# Polymorphism Control and the Formation of Organic Molecular Nanocrystals

by

Xiaochuan Yang

B.S. Chemical Engineering, Tsinghua University, 2008
M.S. Chemical Engineering Practice, Massachusetts Institute of Technology, 2011

Submitted to the Department of Chemical Engineering
In partial fulfillment of the requirements for the degree of

Doctor of Philosophy
At the
MASSACHUSETTS INSTITUTE OF TECHNOLOGY
June 2014

ARCHIVES
MASSACHUSETTS INSTITUTE OF TECHNOLOGY
JUN 30 2014
LIBRARIES

© 2014 Massachusetts Institute of Technology. All rights reserved.

Signature of Author:......... Signature redacted ......................................
Department of Chemical Engineering
June, 2014

Certified by: . Signature redacted ..................................................
Allan S. Myerson
Professor of Chemical Engineering
Thesis Supervisor

Accepted by: ............ Signature redacted ..........................................
Patrick Doyle
Professor of Chemical Engineering
Chairman, Committee for Graduate Students

# Polymorphism Control and the Formation of Organic Molecular Nanocrystals

By

Xiaochuan Yang

Submitted to the Department of Chemical Engineering on May 1st, 2014
In partial fulfillment of the requirements for the degree of
Doctor of Philosophy

## ABSTRACT

The formation of organic molecular nanocrystals is a topic of great interest in the pharmaceutical industry because of the potential increase in dissolution rate and solubility of organic crystals below 1 μm and their potential use in drug products. Previous investigators have developed various methods to produce them; however, breakage, high supersaturation and high intensity mixing are often involved in those methods, producing amorphous solids and if crystalline solid is obtained making control of desired polymorphs difficult. The aim of this thesis is to: (1) Evaluate practical methods to produce organic molecular nano-crystals of the desired form; (2) determine the change in crystal solid properties with size; (3) develop a better fundamental understanding of nucleation kinetics during concomitant nucleation of polymorphs.

The first approach tried used bi-functional Self-Assembled Monolayers (SAMs) substrates. Using mefenamic acid as the model compound, micro-sized and nano-sized crystals were obtained with controlled polymorphs and narrow size distributions. By tuning experimental conditions and surface chemistry, exclusive production of one polymorph was demonstrated as well. On the 1 μm gold islands a single crystal was obtained on each of the islands with a crystal size of ~ 300 nm.

The second approach is crystallization under nano-sized confinement. Using soft confinement (porous polymer membranes), we reported the use of a novel solution impregnation method to form nanocrystals in polymer matrices with various microstructures to systemically study the role of soft confinement and polymer chemistry on the nucleation process of nano-sized crystals. We obtained 100% crystalline materials of four compounds in all experiments and in most cases nanocrystals were the most stable form. The smallest nanocrystals produced were ~ 100 nm. In the rigid confinement (porous silica particles of ~ 40nm pores), we explored the polymorphic outcome of four different compounds using solid state NMR. We found that three out of the four compounds can crystallize in the pores although one showed two polymorphs concomitantly crystallized the same time and another one produces a mixture of two polymorphs and amorphous states. All these nanocrystals under soft and rigid confinement showed significant enhancement of dissolution profiles. These results help advance the fundamental understanding of nucleation under rigid confinement and may lead to potential applications in developing new formulations in the pharmaceutical industry.

The third approach is the use of nano spray drying. We used glycine as the model compound and compare this approach with the first one we developed, and the results suggest that the nanocrystals produced by spraying exhibit wider size distribution and worse surface structures. These defects existing on crystal surface may improve mobility of molecules and cause "crystal-bridging" to form big crystals.

To explore the change in crystal solid properties regarding size, we also measured the solubility vs size curves of two polymorphs of glycine. Both polymorphs showed 20%-30% increase of solubility when crystal size goes down to ~300 nm. Although the curves did not cross in the range that we measured, the extended trends suggested that β-glycine solubility could be lower than α-glycine when the crystal size is smaller than ~100 nm.

Thesis Supervisor: Allan S. Myerson

Title: Professor of Chemical Engineering

# ACKNOWLEDGEMENT

First of all, I would like to express my great appreciation to my thesis advisor Prof. Allan S. Myerson for all the support and encouragement over the duration of my Ph.D. life. His comprehensive knowledge in this field and profound understanding on many key questions really impressed me and intrigued my interest to explore many interesting problems. He also taught me a lot about how to handle complex issues and become a person with better personality. I could not have accomplished so much in my Ph.D. without him.

I want to express my sincere gratitude to Prof. William M. Deen to whom I can always go for when I had questions, Prof. Michael J. Cima for his insightful suggestion in crystallization field and Prof. Michael S. Strano for all the challenging questions and letting me use instruments in his lab.

I would also like to thank Prof. Bernhardt L. Trout, Dr. Markus Krumme, Dr. Norbert Rasenack and Dr. Michael Mazza in Novartis for valuable advice and discussions on my projects in Novartis-MIT research center for continuous manufacturing.

I want to acknowledge my collaborators for their priceless help and support: Dr. David K. Bwambok, Dr. Manza. B. J. Atkinson and Prof. George M. Whitesides in Harvard University, and Dr. Ta-Chung Ong, Dr. Vladimir K. Michaelis and Prof. Robert G. Griffin in Department of Chemistry in MIT.

It has been a pleasure for me to work with many great undergraduate students in the past few years: Jake L. Amereno, Scott Heng, Jennifer Huang, Xi Zhang and Sydney Hodges. Without them I would not have achieved so much.

I would like to thank everyone in the Myerson group, especially Shin Yee Wong, Keith Chadwick, Jie Chen, Ying Diao, Kay Hsi, Min Su, Yuan Jiang, Chris Lai, Li Tan, Jicong Li, Yoyo Peng, Fabienne Courtois, Marcus O'Mahony, Yuqing Cui, Aishuai Xiang, Faika Weche and Andre Puca for his/her company and support, and Novartis and Department of Chemical Engineering for financial support.

Finally, I want to thank my family and my friends for their consistent support.

# Table of Contents

# Table of Figures

## List of Tables

# 1 INTRODUCTION

Organic molecular nanocrystals with controlled polymorphs are of great interest in many industries, especially in pharmaceutical industry where at least 60% of compounds from synthesis exhibit poor aqueous solubility. As crystal size decreases, surface/volume ratio of the crystal increases significantly and thus the dissolution rate can be enhanced. Besides, as Ostwald-Freundlich equation predicts, solubility of the crystal increases as crystal size reduces. Direct production of nano-crystals through crystallization while controlling the crystal form (polymorph) is a difficult problem and a current active area of research. Investigators have explored many novel methods based on the use of confinement (nano-wells), surface templating (polymers and SAM's) and microfluidics. Our group also developed a method to "create confined volume" for crystallization on templated surfaces, which results in both a confined volume and a templating effect. The goal of this thesis is to:

1. Evaluate practical methods to produce organic molecular nano-crystals of the desired form.
2. Determine the change in crystal solid properties with size.
3. Develop a better understanding of nucleation kinetics during concomitant nucleation of polymorphs.

# 2 BACKGROUND

The formation process of crystals is called crystallization, a process that has been used for thousands of years starting with the production of salt from seawater. Crystallization is a critical process in the pharmaceutical industry, aiming to produce crystals with controlled purity, size, morphology and polymorph[1]. Generally, crystallization can be divided into two major steps: nucleation and crystal growth. Within a supersaturated solution, solute molecules start to accumulate into clusters (density fluctuation). The clusters are not stable until they reach a certain size. The generation process of these stable clusters (nuclei) is called nucleation. Crystal growth refers to the aggregation process of more solute molecules in solution onto the existing nuclei. The two processes continue simultaneously as long as supersaturation in the solution still exists. Supersaturation can be generated by cooling, solvent evaporation, change of solvent composition, chemical reaction or pH change. In this chapter, three major topics will be presented as background: (1) nucleation theory (the classical nucleation model and the two-step model), (2) different crystalline structures (polymorphism), (3) templated nucleation on engineered surfaces and (4) the importance of nano-crystals and a literature review of all current methods for manufacture of nano-crystals.

## 2.1 Nucleation

Nucleation can be classified into two categories: primary nucleation and secondary nucleation. Primary nucleation is the initial nucleation process where no crystals are present. Based on whether or not foreign substances are involved in the nucleation process, primary nucleation can be further categorized into heterogeneous nucleation or homogeneous nucleation. Secondary nucleation refers to the nucleation process that is influenced by pre-existing crystals or crystal fragments.

### 2.1.1 Classical nucleation model

In the late 19th century, Gibbs derived basic theoretical results on classical nucleation theory. However, the first paper in this area was published by Volmer and Weber in 1926[2]. Becker and Doring contributed to its further development[3]. Classical nucleation theory was originally proposed to describe the condensation process of a supersaturated vapor phase into spherical liquid droplets, but later it was expanded to crystal formation from supersaturated solution and melts.

Density fluctuation, or concentration fluctuation, is believed to be responsible for the formation of ordered clusters in supersaturated solutions. With the addition of more solute molecules, the cluster becomes stable when it grows to a critical size. The stable clusters are called nuclei, and their formation process is called nucleation.

From the thermodynamic viewpoint, classical nucleation theory[4] states that the nucleation process can be described as a summation of Gibbs free energy changes for phase transformation ($\Delta G_V$) and for surface formation ($\Delta G_S$), as shown in Figure 2-1. Phase transformation refers to the process in which solute molecules aggregate into clusters from solution and form a solid state. Since the solid state is more stable, the first term ($\Delta G_V$) becomes negative and decreases the total free energy of the system. When a cluster forms from solution, an interface between solid and liquid has been introduced into the system. As the cluster grows, the surface tension is overcome and thus surface energy increases. So the second term ($\Delta G_S$) becomes positive and increases the total free energy of the system:

$$\Delta G = \Delta G_V + \Delta G_S = \frac{4\pi r^3}{3}\Delta G_{VV} + 4\pi r^2 \gamma \qquad \text{Equation 2-1,}$$

$$\text{where } \Delta G_{VV} = -\frac{kT \ln S}{V_m} \qquad \text{Equation 2-2,}$$

A spherical cluster is assumed, and r is the radius of the cluster, $\Delta G_{VV}$ is the Gibbs free energy change for phase transformation per unit volume, $V_m$ is molecular volume, $\gamma$ is the surface energy per unit surface area of cluster, and S is supersaturation ratio.

For heterogeneous nucleation, cap-shaped clusters on a flat substrate:

$$\Delta G = \psi(\theta_w)(\frac{4\pi r^3}{3}\Delta G_{VV} + 4\pi r^2 \gamma) \qquad \text{Equation 2-3,}$$

$$\text{where } \psi(\theta_w) = \frac{1}{4}(2 + \cos\theta_w)(1 - \cos\theta_w)^2 \qquad \text{Equation 2-4}$$

and $\theta_w$ is the wetting angle.

Equations below are derived based on homogenous nucleation, but for heterogeneous nucleation of cap-shaped clusters on a flat substrate, $\psi(\theta_w)$ is necessary to be added.

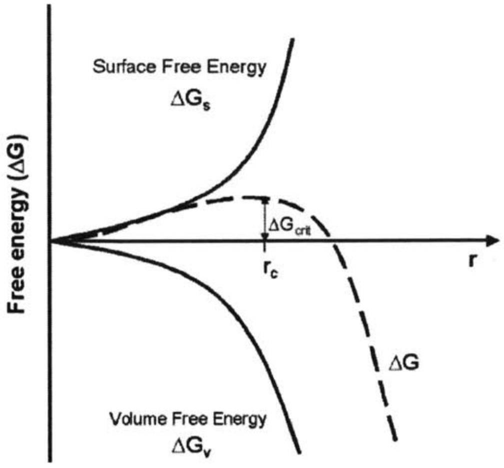

Figure 2-1 Volume, surface and net free energy changes as a function of cluster radius. As the radius increases, surface free energy increase (dominate for small particles) while volume free energy decrease (dominate for big particles), which result in that net free energy increases to the critical value and then decrease.[5]

As a result of the two competing terms, the curve of total free energy change shows two distinct regions as the cluster radius increases. At small radii, the free energy change of the surface formation dominates the total free energy change. The total free energy increases as the cluster radius increases, so cluster growth is not energetically favorable in this region. However, when cluster radius passes the critical size, the free energy change of the phase transformation dominates. The total free energy decreases as the cluster radius increases, so the cluster becomes stable and subsequent growth becomes energetically favorable. This analysis also explains why smaller clusters dissolve preferentially over larger clusters.

The critical radius is reached at the maximum value of the total free energy change ( $\Delta G_{max}$ ):

$$\frac{d\Delta G}{dr} = 4\pi r^2 \Delta G_{VV} + 8\pi r\gamma = 0 \qquad \text{Equation 2-5.}$$

So the critical radius and maximum free energy change can be given as:

$$r_c = \frac{2\gamma V_m}{kT \ln S} \qquad \text{Equation 2-6,}$$

$$\Delta G_{\max} = \frac{16\pi\gamma^3 V_m^{\ 2}}{3(kT \ln S)^2} \qquad \text{Equation 2-7.}$$

Considering $\Delta G_{\max}$ as the free energy barrier to nucleation, the nucleation rate J can be calculated:

$$J = A_n \exp(-\frac{\Delta G_{\max}}{kT}) = A_n \exp(-\frac{16\pi\gamma^3 V_m^{\ 2}}{3k^3T^3 \ln S^2}) \qquad \text{Equation 2-8.}$$

where $A_n$ is the pre-exponential factor,

$$A_n = zf^*C \qquad \text{Equation 2-9}$$

and z is the Zeldovich factor, f* is the frequency of the monomer attachment to a nulceus.

However, several assumptions of the classical nucleation model may not be valid. First, spherical clusters with uniform interior densities and sharp interfaces are not valid. Second, the interfacial tension between clusters and solution cannot be the same as that between infinite planar surfaces and solution. Third, the model assumes the addition of only one monomer at a time and neglects collisions and breakages. Fourth, the process is time-dependent, not steady-state. Fifth, the clusters are assumed to be incompressible.

### 2.1.2 Two-step model

The two-step nucleation theory was originally proposed to describe the crystallization process of proteins. The first step is the aggregation of solute molecules into clusters above a certain size. In contrast to classical nucleation theory, these clusters are not well ordered; they are described as liquid-like clusters since they are believed to be high density domains of solute molecules (See Figure 2-2). The second step is the reorganization of these clusters into ordered clusters called nuclei. This step is believed to be the rate-determining step of nucleation[4].

In addition to many computational simulations[6,-8], significant experimental data also support the two-step nucleation model[9-11]. Appropriate proof is the observation that, as the complexity of molecules increases, their nucleation time also increases. This increase is probably because complex molecules require more time to arrange themselves into ordered structures[5].

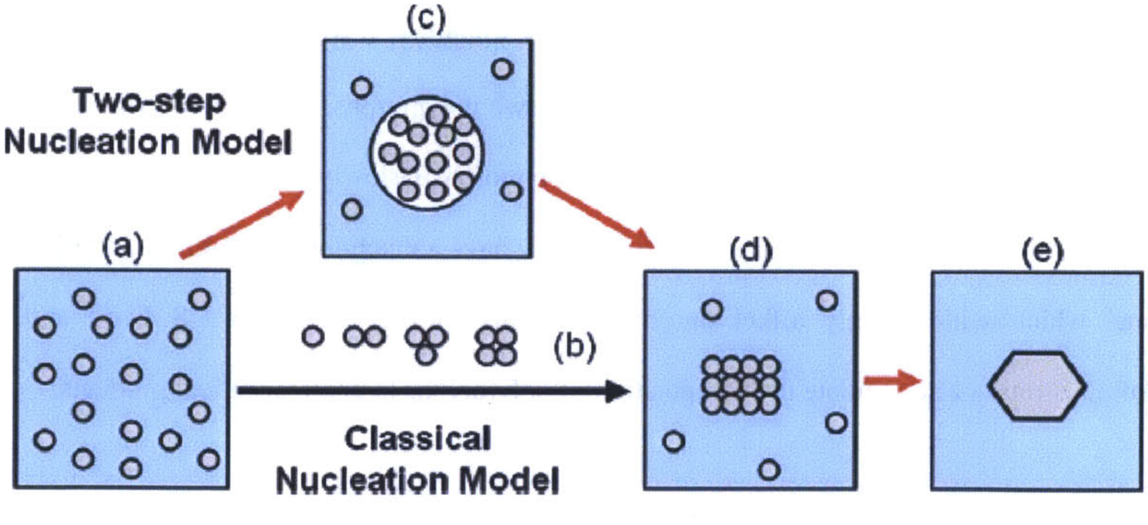

Figure 2-2 Comparison between the classical nucleation theory and the two-step nucleation theory.[5]

## 2.2 Polymorphism

Polymorphism is defined as a phenomenon in which the same molecule has different crystalline forms. Sometimes, amorphous states and solvates are also referred to as polymorphs. The formation of different polymorphs of the same molecule at the same time, known as the concomitant nucleation of polymorphs, is due to the complexity of the molecular arrangement in the nucleation process (See Figure 2-3). Compared to the most stable polymorph, less stable polymorphs (or their combinations) often nucleate faster. Work by our group[12-14] has demonstrated that large numbers of independent crystallization experiments can often produce most if not all polymorphs in a given substance if a large enough sample is taken. Concomitant nucleation is additional evidence in support of the two-step nucleation model, as it might indicate that the random process of the second step determines the polymorphic form obtained.

Polymorphs are very important in the pharmaceutical industry, since different polymorphs may possess totally different solid properties, such as solubility, dissolution rate, density and heat capacity. For example, consider a molecule with two polymorphs, A and B. Polymorph B is the desired and produced form. During storage, polymorph B slowly transforms to polymorph A, which is more stable. However, polymorph A may have a much lower solubility and dissolution rate, which will strongly affect the bioavailability of the drug. The US Food and Drug Administration also regulate the composition of polymorphs in pharmaceutical products.

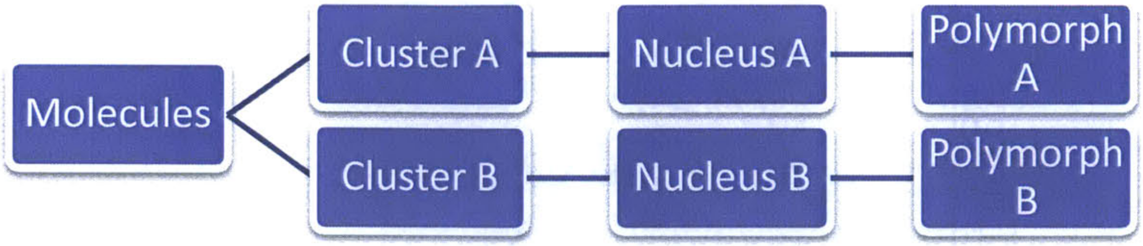

Figure 2-3 Crystallization process of polymorphs. Different nuclei of polymorph A and B form simultaneously at the nucleation process.

A detailed thermodynamic illustration is shown in Figure 2-4. The metastable form B has a lower free energy barrier, while the more stable polymorph A possesses a higher activation energy. If the pre-exponential factors are the same for A and B, polymorph B will have a faster nucleation rate than A. However, the final products depend on the combination of relative nucleation rates, relative crystal growth rates and transformation rates between polymorphs. From an experimental perspective, the control of different solvents, solution pH, temperature and surface properties will strongly affect the polymorphic outcome. For example, different self-assembled-monolayers coated on a substrate will modify the surface property and thus affect the polymorphic outcome, which will be discussed in details in next section.

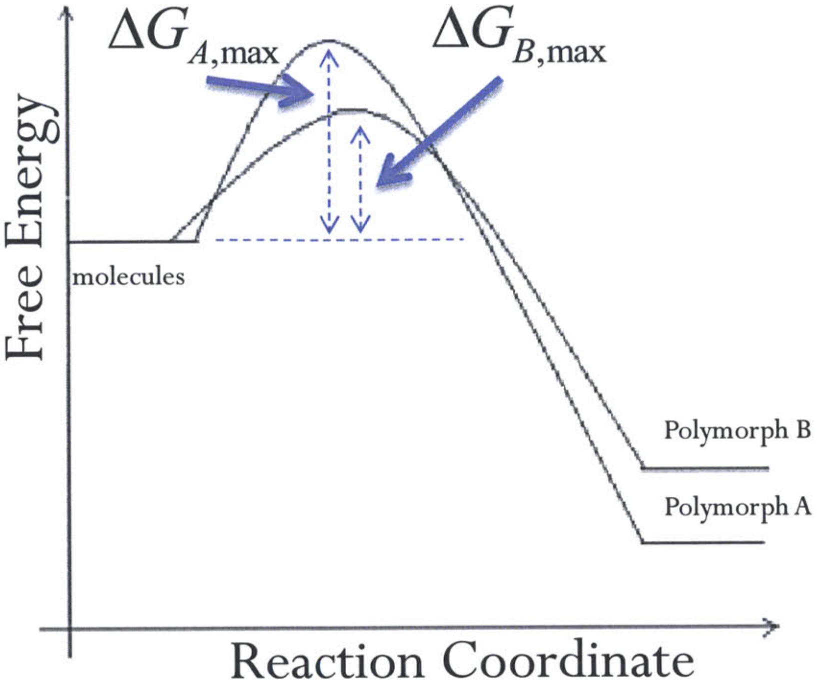

Figure 2-4 Concomitant nucleation of polymorph A & B. While polymorph B is less stable than polymorph A, activation energy for formation of polymorph B is less than that of polymorph A. Therefore, nucleation rate of polymorph B may be higher than that of polymorph A.

## 2.3 Templated nucleation on engineered surfaces

Due to different surface properties, the thermodynamics and kinetics of the crystallization process can be deeply affected by different interactions between surfaces and crystals.

Through varying the nature of the polymer surfaces at the same solvent and temperature, Price et al.[15] selectively produced certain polymorphs in acetaminophen, sulfamethoxazole, carbamazepine and 5-methyl-2-[(2-nitrophenyl)amino]-3-thiophenecarbonitrile (ROY). With the same polymer-induced heteronucleation approach, Grzesiak et al.[16] successfully made several phases of hen egg white lysozyme (HEWL) with controlled nucleation rate.

Monolayers coated on surfaces provide nucleation sites and also affect crystal growth based on the monolayers' chemical properties. Carter et al.[17] discovered that the composition of self-assembled monolayers strongly affects polymorph screening of formed crystals of anthranilic acid (2- aminobenzoic acid) and that hydrogen-bonding functionality may be important to the nucleation process. Hiremath et al.[18] coated thiol self-assembled monolayers (SAMs) of substituted 4'-X-mercaptobiphenyls (X = H, I, and Br) on gold surfaces, on which they selectively crystallized α-, β-, and γ- 1,3-bis(m-nitrophenyl) urea (MNPU) phases, respectively. Banno et al.[19] found that the chirality of the attached enantiomer determines the enantioselective crystal growth on the SAMs.

## 2.4 Importance of organic nano-crystals

### 2.4.1 Definition of Nanocrystals

Currently, nano-crystals are of great interest in the pharmaceutical industry. Over 60% of drugs directly from synthesis have poor solubility[20]. However, as the particle size decreases below 1 micrometer, solubility of these drugs will be enhanced significantly, which will strongly enhance the bioavailability of the drug.

### 2.4.2 Solubility vs size

Inspired by the Kelvin equation (also called the Gibbs-Thomson or Gibbs-Kelvin relation)[21, 22], Ostwald expanded the same argument to solid-liquid systems[23]. The analysis was later refined by Freundlich[24, 25], Jones[26, 27], and Dundon and Mack[28]. It is normally referred to as the Ostwald-Freundlich equation:

$$\rho\nu\frac{RT}{M}\ln\frac{S_r}{S_\infty}=\frac{2\gamma}{r} \qquad \text{Equation 2-10,}$$

where a spherical model is assumed, $\rho$ is density, $\nu$ is the number of moles per mole of electrolyte, R is the gas constant, T is temperature, M is molecular weight, $S_r$ is the solubility at particle radius r, $S_\infty$ is the solubility at a plane surface and $\gamma$ is surface tension.

Assuming other parameters are constant, solubility ($S_r$) increases as particle radius decreases. Since it is an exponential function, Equation 2-10 implies that solubility of nano-crystals increases faster when the particle size becomes smaller. Experimental results also support this trend (See Figure 2-5).

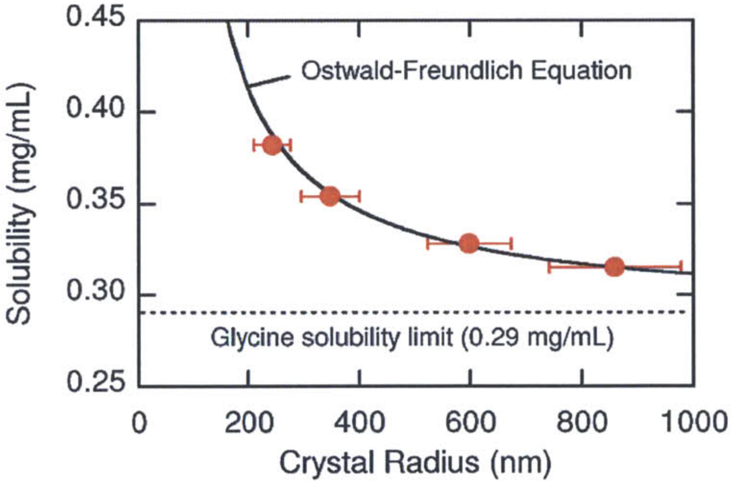

Figure 2-5 Solubility of β-glycine crystals in methanol: experimental data (red dots) vs the Ostwald-Freundlich calculation curve. Solubility of nanocrystals ~ 200nm is enhanced by 31.4%[14].

## 2.5 Methods to produce nanocrystals

Based on the crystal formation process, methods to form nano-crystals can be divided into two categories: "top down" and "bottom up". "Top down" methods refer to those that break large crystals into smaller ones, such as milling and high pressure homogenization. The introduction of impurities, high energy consumption, and possible polymorph transformation are their major problems. "Bottom up" methods refer to those that aggregate single molecules into nano-scale crystals, such as supercritical fluid crystallization, impinging jet crystallization, and confined crystallization. However, the high supersaturation and/or high intensity mixing involved in supercritical fluid crystallization and impinging jet crystallization make control of crystal size and polymorphs difficult. Nano-pores and similar materials confine crystals in a nearly sealed environment, which impedes their characterization and further use. Microfluidic devices are used to produce nano-crystals with uniform size distribution, but these devices experience channel clogging, which affects the continuous mass production of crystals. Nanowells, despite their manufacturing complexity, have become a popular tool for producing nano-crystals in recent years. Detailed introductions to all these "bottom up" methods are provided below.

### 2.5.1 Precipitation or emulsification

These two methods are based on the formation of a stable emulsion solution, followed by anti-solvent or cooling methods. Kwon et al.[29] produced pi-conjugated organic nano-crystals, such as tetracene, $C_{60}$ fullerene, and anthracene, from 30 nm to 110 nm in a stabilizer-free oil-in-water emulsion. However, these methods have the disadvantages of experimental variations, selection limitation of the solvent and low productivity. The nano-crystals produced are also easy to aggregate in the process and have a wide size distribution.

### 2.5.2 Supercritical fluid crystallization

The solubility of drugs in a supercritical fluid deceases significantly as pressure decreases. The rapid expansion of the supercritical solution (RESS) method jets a drug solution through a micro-jet to form high super saturation and thus produces nano-sized particles. Turk used carbon dioxide as the supercritical solvent and made particles of 1.5-3 μm for naphthalene, 0.8-1.2μm for benzoic acid, and less than 350 nm for cholesterol[30]. Turk and Lietzow used the same method to make particles of 130 nm for salicylic acid, 80 nm for Ibuprofen, and 50 nm for phytosterol[31]. Another method called Supercritical Anti Solvent (SAS) uses supercritical fluid as an anti-solvent for crystallization. For example, Reverchon et al.[32] obtained an agglomerate of 0.25-1.2μm, using amoxicillin/N-methyl pyrrolidone (NMP) or amoxicillin/dimethylsulfoxide (DMSO) solution and supercritical $CO_2$ as the anti-solvent.

### 2.5.3 Impinging jet crystallization

High intensity micro-mixing of two fluid streams is employed in impinging jet crystallization. One fluid stream is the desired drug solution, and the other one is a solvent that can lower the solubility of the drug and initialize crystallization. Affected by the solvent, drug molecules begin to crystallize once mixed. Siddiqui et al. demonstrated successful production of 300 nm particles of iron oxide by using a confined impinging reactor[33]. With confined liquid impinging jets, Chioua et al. made suspensions of cyclosporine A (CsA) particles of 180–700 nm and obtained about 1μm agglomerates of CsA particles after spray drying[34]. However, high supersaturation and the high intensity micro-mixing process involved make this method difficult to monitor and control.

### 2.5.4 Microfluidics

Microfluidic devices have been widely used to produce nano-particles of polymeric, inorganic and metallic materials, but their applications for producing organic nano-crystals are rare. Sultana[27] proposed an explanation for why organic nano-crystals are difficult to make: compared to inorganic molecules, the nucleation of organic molecules does not adequately desupersaturate the solution and residual high supersaturation causes growth and coalescence of big particles which result in channel clogging. However, several researchers have found ways to overcome such difficulties. Hansen et al.[36, 37] successfully controlled protein crystallization based on a microfluidic device; Genota et al.[38] synthesized rubrene nano-crystals from 50 nm to 110 nm with varied flow conditions in a 3D hydrodynamic focusing microreactor.

### 2.5.5 Crystal formation in confined environments - nanopores and nanowells

Nano-crystals can also be obtained through crystallization in a nano-sized confined volume. Jackson and McKenna[39] studied the crystallization process of o-terphenyl and benzyl alcohol confined in controlled pore glass (CPG) materials. They observed the glass transition temperature change at various pore sizes (4-73nm), chemical surface treatments and degrees of pore filling; and concluded that the confined crystallization process is strongly affected by pore size and degree of pore filling. However, since the crystallization occurs in the confined volumes and probably adheres to the inner surface of these pores, the crystals formed are hard to remove from the materials. Crystallization in various gels, which is a similar method to that of CPG, has the same removal problem.

By using patterned microwells, Wang et al.[40] produced different polymorphs of proteins, lysozyme, thaumatin, and glucose isomerase as fine as 600 nm. They concluded that the control to produce different polymorphs depends on the control of evaporation kinetics. You et al.[41] developed a strategy to generate drug nano-crystals based on crystallization in attoliter nanowells (diameter 600 nm): by varying the concentration of arsenic trioxide (ATO) solution, nano-crystals from 55 to 175 nm were formed.

## 2.6 Experimental methods and methods of analysis in our group

### 2.6.1 Previous experimental methods

Our group has developed several methods to control crystallization with SAMs. Lee et al.[12] have developed a method to obtain micro-scale gold islands with SAMs as the substrate to control crystal size and structure. α-, β-, and γ- glycine were reported with the controlled solution conditions. Singh et al.[42] developed a high throughput method based on SAMs on gold islands and were able to obtain six of seven stable polymorphs of ROY, including YT04 which had never been reported to crystallize from solution. Kim et al.[14] have demonstrated the formation of glycine nano-crystals (see Figure 2-6) on hydrophilic SAM circular islands surrounded by hydrophobic SAM areas.

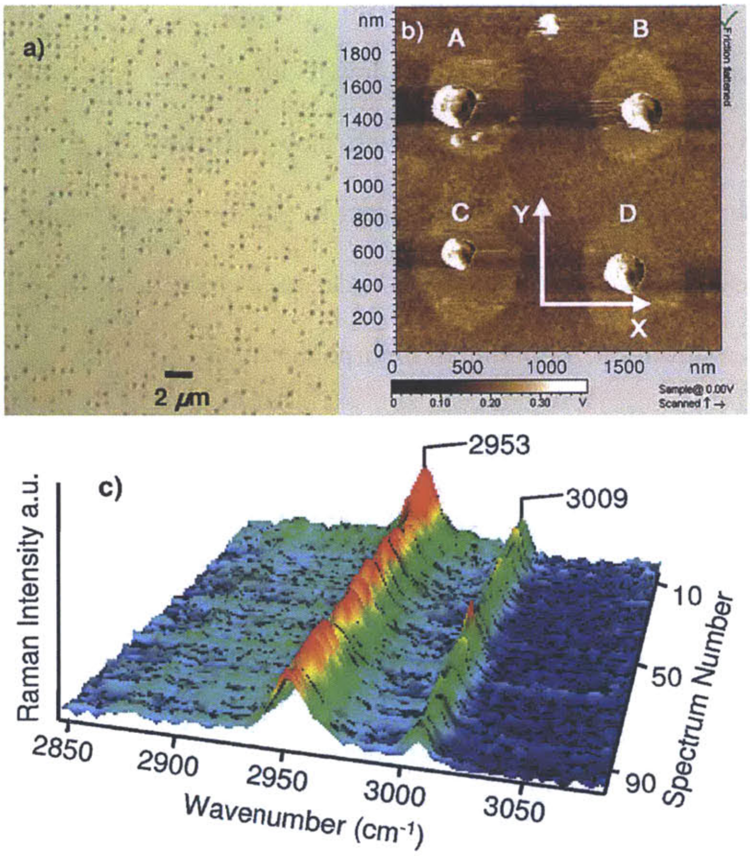

Figure 2-6 (a) Optical microscopic image of nano-crystals. (b) AFM image of nano-crystals. (c) RAMAN spectra of 100 nano-crystals. All of them are β-form[14].

Kim, K., a former Ph.D. student in our group, developed a technique based on photolithography for patterned SAMs on silicon[14]. The simple procedure can be summarized as follows (See Figure 2-7). First, a silicon wafer was coated with negative photoresist (SU8). Under an ultraviolet light of 245 nm wavelength and hard-contact with a patterned mask, the desired pattern was developed in the photoresist layer. Second, 3-aminopropyltriethoxysilane (ATPES), a hydrophilic SAM, was coated onto an exposed area of a silicon wafer. Third, after removing the photoresist, octadecyltrichlorosilane (OTS), a hydrophobic SAM, was applied to the area that the photoresist once occupied. In the fourth step, this bifunctional SAMs substrate was put into unsaturated glycine/water solution and then drawn out slowly. Very small droplets were thus formed on the hydrophilic SAMs. Fifth, with slow diffusion of ethanol into the droplets, solubility decreased and supersaturation occurred to glycine crystallization. The fourth and fifth steps were processed in a vessel of hexane in order to prevent too quick evaporation of droplets in air, which may result in the formation of amorphous states.

Solubility vs size test requires immediate preparation of several supersaturated solutions before the experiment. Substrates with nano-crystals were immersed in these solutions and then taken out to observe whether or not the nano-crystals dissolved. The methods for analysis included AFM and RAMAN microscopy. AFM can provide a clear 3D image, and RAMAN spectra identify the sample's polymorph.

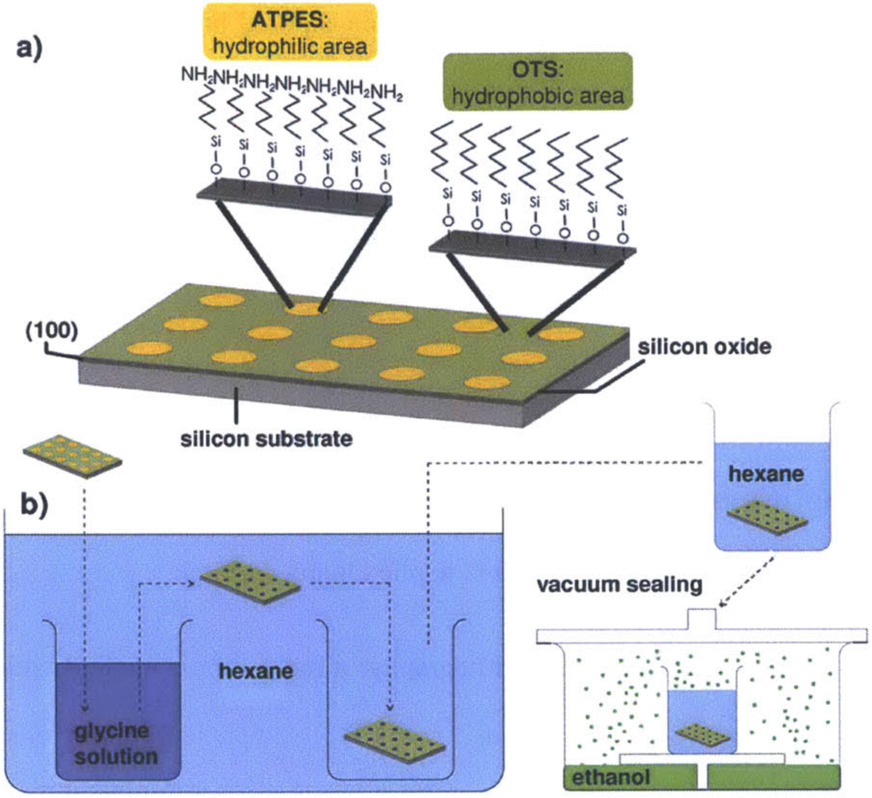

Figure 2-7 (a) Bi-functional SAMs. (b) Crystallization caused by slow diffusion of ethanol (as the anti-solvent) into glycine/water solution[14]

However, this current technique has several drawbacks.

First, 500 nm feature size is almost the limit for photolithography with available facility in MIT. The wavelength of UV light (345 nm) is only half of the smallest feature, which may cause diffraction. Furthermore, the light dose must be strictly controlled: excessive light dose will cause reflection in the photoresist; if the light dose is insufficient, the light reaction cannot penetrate the entire layer.

Second, the photoresist (SU8) is hard to clean. Once exposed baked, it is a highly cross-linked epoxy. It will not be fully removed without special remover solution, piranha etching/cleaning, plasma ashing, laser ablation or pyrolosis. Since the photoresist is in hard contact with the chrome mask, it may contaminate the mask and affect the tightness of hard contact in future processing.

### 2.6.2 New improvements and current experimental methods developed

Three major improvements are proposed and applied in my research:

(1) Photolithography → electron beam lithography: a more robust method which can produce smaller nano-crystals and has no mask cost;

Electron beam lithography, called "E-beam Lithography", is a technique for scanning an electron beam across a surface covered with a thin film resist. It is similar to the photo lithography process, except that an electron beam is used to expose the photoresist. Compared to photo lithography, electron beam lithography has several benefits, as outlined below.

First, there is no mask investment. Because the movement of the beam spot is controlled by a machine command, the desired pattern is required to be drawn only in software and then the software will automatically program it into commands for the machine to implement.

Second, the smallest feature size that can be achieved in this technique is 17 nm. Ebeam lithography is not limited by the diffraction of light. The beam diameter is 7 nm, so theoretically the feature size limit would be about 7 nm. Beam control, dose intensity and the subsequent development process of the photoresist still impose some technical limits that increase the achievable feature size. However, achieving features of 50 nm should not be a problem.

Third, the photoresist (PMMA) is easy to clean and remove. Standard solvents, such as acetone, photoresist thinner solution, or positive photoresist removers can easily remove PMMA photoresist.

The electron beam lithography facility located in the EE&CS department of MIT is a Raith 150, which is modified from a Leo SEM column. Its acceleration voltage varies from 1 kV to 30 kV and the electron beam diameter is about 3 nm (for low current), with a fixed step size of 2 nm. An arbitrary pattern with a minimum feature size of 17 nm is claimed to be achievable on this machine.

(2) Coating a gold layer under SAMs: more options to choose SAMs for surface modification. This enables us to conduct research on the effect of different SAMs on the polymorph control.

(3) Characterizing nano-crystals under 100nm is another challenge in this project, many methods are proposed here which I going to try. One most promising method we applied is surface-enhanced Raman microscopy, with which intensity of desired area can be amplified several hundred times or more.

### 2.6.3 Methods of analysis

Nanocrystals are not easy to characterize since they are only several hundreds of nanometers or less in size. Besides, since some crystallization research was conducted on a templated surface or confined porous matrix, crystals bond firmly to the surface or are not exposed at all, making it difficult to apply some measurement methods.

*AFM* A clear three dimensional map of nano crystals can be obtained.

*IR/ RAMAN* Since the vibration and rotation information of bonds are specific to a certain polymorph, IR/ RMAM spectra are able to discern the crystal structure. Surface-enhanced or tip-enhanced RAMAN spectra (where intensity of desired area is strengthened by near-field radiation[43]) may be able to characterize these nano-crystals under 100 nm.

*STM* Atom arrangement on the surface may be determined in order to identify different polymorphs.

*SEM The* morphology and nano-scale structures of the surface can be detected. Some substances may have different appearances or morphologies for different polymorphs, and will be possible to distinguish under SEM.

*NMR* Since atoms are in different chemical structures in different polymorphs, NMR spectra can be used to determine different polymorphs.

*X-ray Crystallography* From the diffracted X-ray beams, a three dimensional map of electron density can be estimated and thus the structure of the atoms can be obtained. Moreover, if a single crystal of sufficient size (at least 0.1 mm) is not possible, some other X-ray methods may also be applied, such as fiber diffraction, powder diffraction or small-angle X-ray scattering.

*Electron Crystallography (TEM)* TEM can detect very tiny crystals that X-rays may not be able to measure. And unlike X-ray diffraction, phase information can easily be experimentally determined by TEM.

*DSC/DTA/TGA* These techniques can measure the property changes within a certain temperature range for different polymorphs. However, a sufficient number of samples may not be available for application of these methods.[1]

## 2.7 Reference

1. R. Hilfiker, Polymorphism in the Pharmaceutical Industry, WEILEY-VCH, Weinheim, 2006.
2. M. Volmer and A. Weber, *Z. Phys. Chem*, 1926, **119**, 277.
3. R. Becker and W. Doring, *Ann. Phys.*, 1935, **24**, 719.
4. D. Kashchiev, *Nucleation: Basic Theory with Applications*, Butterworth-Heinemann, Oxford, 2000.
5. D. Erdemir, A. Y. Lee and A. S. Myerson, *Accounts of Chemical Research*, 2009, **42**, 621.
6. J. D. Shore, D. Perchak and Y. Shnidman, *J. Chem. Phys.*, 2000, **113**, 6276-6284.
7. E. B. Treivus, *Kristallografiya*, 2001, **46**, 1125.
8. C. Haas and J. Drenth, *J. Phys. Chem. B*, 2000, **104**, 368.
9. Y. Georgalis, P. Umbach, J. Raptis and W. Saenger, *Acta Crystallogr. Sect. D*, 1997, **53**, 691.
10. D. Pontoni, T. Narayanan and A. R. Rennie, *Prog. Colloid Polym. Sci.*, 2004, **123**, 227.
11. K. Igarashi, M. Azuma, J. Kato and H. Ioshima, *J. Crys. Grow.*, 2006, **204**, 181.
12. A. Y. Lee, I. S. Lee, S. S. Dette, J. Boerner and A. S. Myerson, *J. Am. Chem. Soc.*, 2005, **127**, 14982.
13. I. S. Lee, K. T. Kim, A. Y. Lee and A. S. Myerson, *Crys. Grow. Des.*, 2008, **8**, 108.
14. K. Kim, I. S. Lee, A. Centrone, T. A. Hatton and A. S. Myerson, *J. Am. Chem. Soc.*, 2009, **131**, 18212.
15. C. P. Price, A. L. Grzesiak and A. J. Matzger, *J. Am. Chem. Soc.*, 2005, **127**, 5512.
16. A. L. Grzesiak and A. J. Matzger, *Crys. Grow. Des.*, 2008, **8**, 347.
17. P. W. Carter and M. D. Ward, *J. Am. Chem. Soc.*, 1994, **116**, 769.
18. R. Hiremath, J. A. Basile, S. W. Varney and J. A. Swift, *J. Am. Chem. Soc.*, 2005, **127**, 18321.
19. N. Banno, T. Nakanishi, M. Matsunaga, T. Asahi and T. Osaka, *J. Am. Chem. Soc.*, 2004, **126**, 428.
20. A. S. Myerson, *Handbook of Industrial Crystallization*, Butterworth-Heinemann, 2002.
21. W. Thomson, *Proc. Roy. Soc. Edinburgh*, 1870, 7, 63.
22. W. Thomson, *Phil. Mag.*, 1871, **42**, 448.
23. W. Z. Ostwald, *Z. Phys. Chem.*, 1900, **34**, 495.
24. H. Freundlich, *Kapillarchemie*, Engelmann, Leipzig, 1909.
25. H. Freundlich, *Colloid and Capillary Chemistry*, Dutton, New York, 1923.
26. W. J. Jones, *Ann. Phys.*, 1913, **41**, 441.
27. W. J. Jones, *Z. Phys. Chem.*, 1914, **82**, 448.
28. M. L. Dundon and E. Mark, *J. Am. Chem. Soc.*, 1923, **45**, 2479.
29. E. Kwon, H. Oikawa, H. Kasai and H. Nakanishi, *Crystal growth & design*, 2007, 7, 600.
30. M. Turk, *Journal of Supercritical Fluids*, 1999, **15**, 79.
31. M. Turk and R. Lietzow, *Journal of Supercritical Fluids*, 2008, **45**, 346.
32. E. Reverchon, G. D. Porta and M. G. Falivene, *Journal of Supercritical Fluids*, 2000, **17**, 239.

33. S. W. Siddiqui, Y. Zhao, A. Kukukova and S. M. Kresta, *Ind. Eng. Chem. Res.*, 2009, **48**, 7945.
34. H. Chioua, H. K. Chana, D. Henga, R. K. Prudhommeb and J. A. Raperc, *Journal of Aerosol Science*, 2008, **39**, 500.
35. M. Sultana, *Thesis: Microfluidic Systems for Continuous Crystallization of small organic molecules*, Masschusetts Institute of Technology, Cambridge, 2010.
36. C. L. Hansen, S. Classen, J. M. Berger and S. R. Quake, *Journal of the American Chemical Society*, 2006, **128**, 3142.
37. C. L. Hansen, E. Skordalakes, J. M. Berger and S. R. Quake, *Proceedings of the National Academy of Sciences of the United States of America*, 2002, **99**, 16531.
38. V. Genota, S. Desportesb, C. Croushorea, J. Lefevrea, R. B. Pansua, J. A. Delairea and P. R. Rohrb, *Chemical Engineering Journal*, 2010, **161**, 234.
39. C. L. Jackson and G. B. McKenna, *Chem. Mater.*, 1996, **8**, 2128-2137.
40. L. Wang, M. H. Lee, J. Barton, L. Hughes and T. W. Odom, *J. Am. Chem. Soc.*, 2008, **130**, 2142.
41. E. A. You, R. W. Ahn, M. H. Lee, M. R. Raja, T. V. OHalloran and T. W. Odom, *J. Am. Chem. Soc.*, 2009, **131**, 10863.
42. A. Singh, I. S. Lee and A. S. Myerson, *Crys. Grow. Des.*, 2009, **9**, 1182.
43. R. M. Stockle, Y. D. Suh, V. Deckert and R. Zenobi, *Chemical Physics Letters*, 2000, **318**, 131.

# 3 POLYMORPH CONTROL OF MICRO/NANO-SIZED MEFENAMIC ACID CRYSTALS ON PATTERNED SELF-ASSEMBLED MONOLAYER ISLANDS

The nucleation of organic molecular compounds is a stochastic process and is difficult to control. The problem becomes even more complex when the compound has two or more polymorphic forms which can concomitantly nucleate. In this work, patterned self-assembled monolayers (SAMs) are employed, on which a large number of identical experiments can be conducted. SAMs can be an effective way to induce heterogeneous nucleation and were used in this work to generate the desired polymorphic form based on the chemical interactions. Seven different self-assembled monolayers were employed to study the nucleation behavior of the non-steroidal anti-inflammatory drug mefenamic acid [MA, N–(2, 3–xylyl)anthranilic acid]. The results show that SAMs forming a strong interaction with -COOH group of MA molecules preferably produced form II. The effects of temperature, solvent, droplet size and concentration on the nucleation kinetics of MA were also explored. The ability to prepare crystalline MA as small as ~ 300 nm while controlling the polymorphic form was demonstrated.

## 3.1 Introduction

Polymorphs, different crystalline structures of the same molecule, are of great interest to pharmaceutical industry. Different polymorphs may possess different physicochemical properties, such as solubility, melting point, density and stability. These differences are vital in the process development and quality control in industry.[1-3] Polymorph control can be conducted through choosing different solvents, supersaturation level, temperature, cooling rates and pH values.[4-9] Self-assembled monolayers, as a promising approach to modify the surface chemistry, have been used to control crystal size, shape and polymorph.[10-12] Aizenberg et al. studied on the oriented growth of calcite controlled by SAMs with different functional groups and found that SAMs with $CO_2^-$, $SO_3^-$, $PO_3^{2-}$, and $OH^-$ as functional groups facilitate in nucleation, whereas SAMs with $N(CH_3)_3^+$ and $CH_3$ inhibited nucleation.[14] Our group introduced a high throughput method to quantify the effect of solution concentration and island size on the polymorphism of glycine. We discovered that strong interfacial interactions, such as hydrogen bonding, between the functional groups of SAMs and the individual molecules of the crystallizing phase were attributed to the different crystallographic planes of L-alanine and DL-valine grown on SAMs of 4′-hydroxy-(4-mercaptobiphenyl), 4′-methyl-(4-mercaptobiphenyl) and 4-(4-mercaptophenyl)pyridine.[15] Hiremath et al. selectively crystallized *α*-, *β*-, and *γ*-1,3-bis(m-nitrophenyl) urea phases by using the substituted 4′-X-mercaptobiphenyls (X= H, I, and Br) and proposed the hypothesis of geometric lattice matching and chemical interactions at the SAMs/crystal interfaces.[16] Thalladi and coworkers showed that the perfluoroalkyl-terminated siloxane SAMs can promote the exclusive growth of the stable γ form of indomethacin by suppressing the nucleation of the metastable α form.[17] Pokroy et al. used $HS(CH_2)_{10}COOH$ and $HS(CH_2)_{11}COOH$ supported on gold films to induce a very controlled, specific orientation of malonic and succinic acid crystals.[18] Swift and coworkers studied crystallization process of 1,3-bis (m-nitrophenyl) urea with 11 different siloxanes and 3 unique solvents. The results suggested that siloxane SAMs tended to favor the growth of the metastable forms (β, δ, γ) and completely suppress the growth of the most stable form α.[19] Zhang et al. showed that at low supersaturation form II of tolbutamide were crystallized on the methyl-terminated SAMs and trifluoromethyl-terminated SAMs, while form IV were obtained on phenyl-terminated SAMs.[20] Even though there has been a large effort by many researchers, the mechanism of the interactions between SAMs and the induced crystals are not fully understood.

Mefenamic acid (Figure 3-1) is a poorly water soluble, non-steroidal anti-inflammatory drug available in capsule and tablet formulation. The drug has been reported to exhibit polymorphism and two polymorphs have been reported (stable form I and metastable form II).[13] In this work we explored the nucleation of MA on seven different self-assembled monolayers and also the effect of island size, solvent and temperature on the polymorphs of MA obtained.

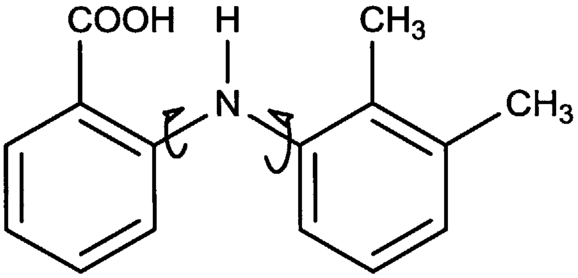

Figure 3-1 Molecular flexibility along C–N bond drives the polymorphism of MA.

## 3.2 Experimental section

### 3.2.1 Materials

Mefenamic acid ($C_{15}H_{15}NO_2$), 4-Mercaptopyridine (4MPY), 3-mercaptopropionic acid (3MPA), 3-mercaptobenzoic acid (3MBA), 16-Mercaptohexadecanoic acid (MHA), DL-Mercaptosuccinic acid (MSA), 3-Mercapto-1,2-propanediol (3MP) and 1-Mercapto-2-propanol (1MP), n-Octadecyltrichlorosilane (OTS) were purchased from Sigma Aldrich. Methanol ($CH_3OH$), ethanol ($C_2H_5OH$) and toluene ($C_6H_5CH_3$) were purchased from VWR. The commercial mefenamic acid purchased from Aldrich was analyzed by powder X-ray diffraction and Raman spectroscopy and found to be form I. Silicon wafers were purchased from Silicon Valley Microelectronics Inc., CA.

### 3.2.2 Bifunctional SAM preparation

Patterned gold substrates with island size 250 μm/100 μm/1 μm were prepared in MIT microsystems technology laboratories (Figure 3-2). Silicon substrate was patterned by photolithography first, coated with 5 nm titanium layer and 50 nm gold layer. The rest photoresist were stripped off by immersing the substrates in acetone for 2 hours. After being cleaned and dried with a nitrogen gun, the substrates with gold islands were ready to prepare bi-functional self-assembled monolayers (SAMs). Fabricated substrates with patterned gold islands as mentioned above were cleaned with piranha solution (A typical mixture of 3:1 concentrated sulfuric acid to 30% hydrogen peroxide solution) for 20 minutes for the cleaning of all organic impurities from the surface. Substrates were then washed with copious amount of pure water and isopropanol then dried with nitrogen gun. Cleaned patterned substrates were slowly put into a 10 mM thiol/ethanol solution in pure nitrogen atmosphere for 18 hours for the formation of hydrophilic SAMs on gold islands, i.e. –COOH group of 3MPA exposing outwards. Substrates were rinsed three times with pure ethanol and dried with nitrogen gas and immersed into a 2 mM OTS (n-Octadecyltrichlorosilane)/toluene solution for 40 minutes for the formation of hydrophobic SAMs on the remaining silicon surface. After being rinsed 3 times with pure toluene and dried with nitrogen gas, the bi-functional SAMs substrates were ready with hydrophilic thiol on gold islands and hydrophobic OTS on the remaining silicon area for the crystallization of MA. Other functional SAMs mentioned above were prepared with the same procedure. Surfaces with different SAMs were scanned under Atomic Force Microscope (AFM). The roughness of these gold island surfaces were at most ±2 nm.

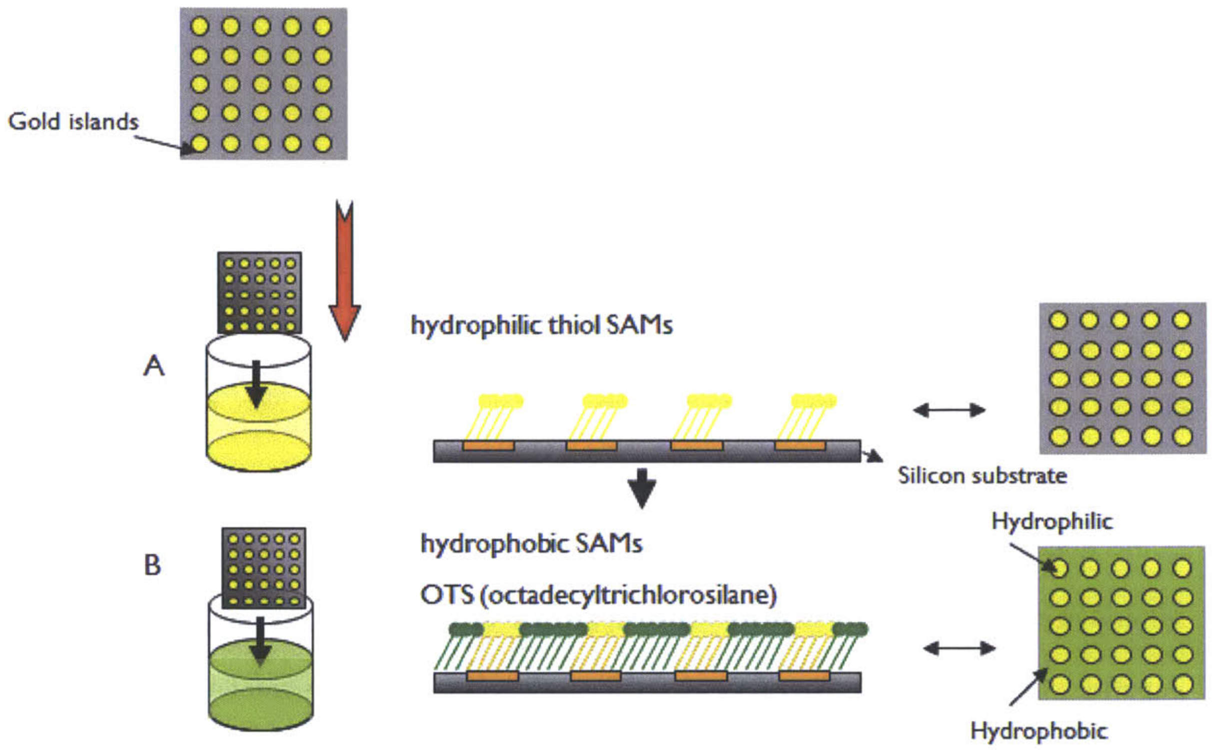

Figure 3-2 SAM patterning process: A. patterned gold islands were coated with hydrophilic SAMs first; B. the remaining area was coated with hydrophobic SAMs.

### 3.2.3 Crystallization procedure

The 3.0 mg/g MA in methanol solution was prepared. We poured 20 ml of 3.5 mg/g MA solution into a 500 ml glass jar and covered the jar with parafilm to control the evaporation from the droplets of API solution on the patterned substrates. The bi-functional SAMs substrates were placed inside the jar with plastic support which ensures the substrates do not touch the liquid. After 3 hours, the atmosphere inside the glass jar was saturated with methanol vapor. A 10 ml syringe with a 21G2 needle was used to punch a hole in the parafilm and drop the 3.0 mg/g solution on the substrates and the jar was slightly tilted to get rid of additional MA solution on the surface. Droplets on islands started to evaporate slowly became supersaturated (Figure 3-3). This slow evaporation of solvent resulted in the formation of crystals rather than amorphous solids as confirmed by polarized light and Raman microscopy.

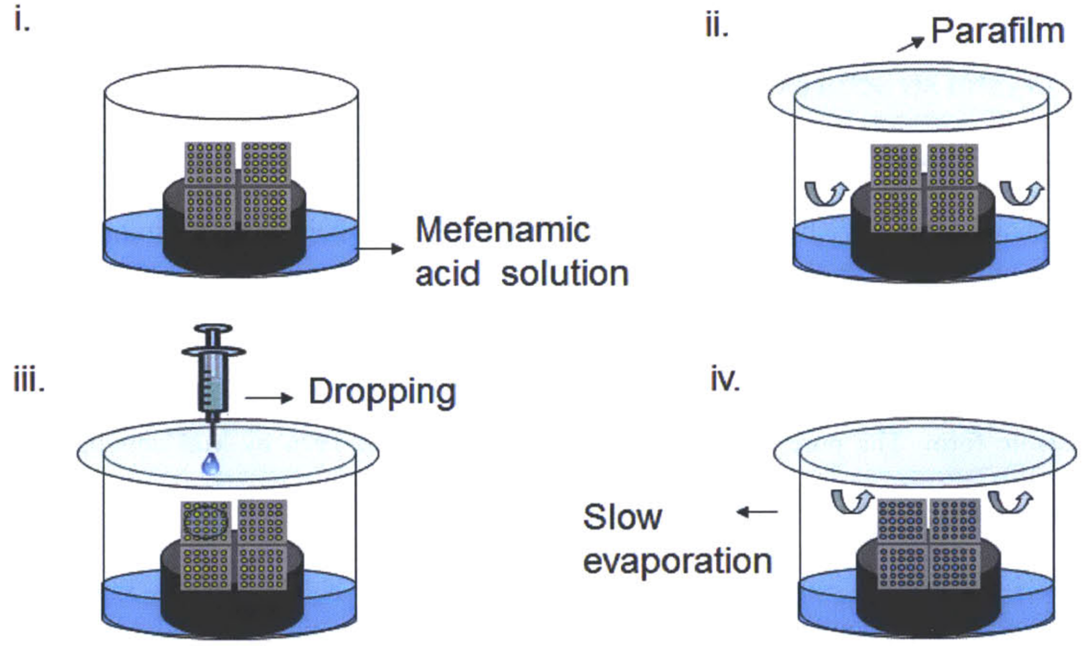

Figure 3-3 Crystallization set-up: (i) The substrates were supported away from the solution at the bottom; (ii) The jar was covered with a parafilm. After 3 hours, the inside was saturated with solvent vapor; (iii) MA solution was dropped on the substrates by a syringe; (iv) After tilting the jar to form droplets on islands, the jar was left still for crystallization.

Raman spectra: The Raman microscope (Kaiser Optical Systems, Inc.) is equipped with a 785 nm exciting line using a 600 grooves/mm grating and a 100x microscope objective. The spectra were collected from 100 $cm^{-1}$ to 1800 $cm^{-1}$ spectral range and we are specifically interested in the range from 100 $cm^{-1}$ to 1200 $cm^{-1}$. For crystals smaller than 1 μm, we used Horiba Jobin-Yvon

Labram HR800 spectrometer equipped with a 514 nm line using 1800 grooves/mm and a 100x microscope objective. One benefit of gold islands is that the Raman signal is enhanced due to the surface-enhanced effect by gold. The characteristic peaks 624,703 $cm^{-1}$ for form I and 631,694 $cm^{-1}$ for form II were used for polymorph characterization. One crystal was analyzed on each island, and at least 100 individual MA crystals were recorded.

## 3.3 Crystal structures of mefenamic acid

Two enantiotropically related polymorphs of this widely-prescribed non-steroidal anti-inflammatory drug have been reported in the past along with their single crystal structures. DSC analysis showed that below 170°C, form I is the stable form while form II is the metastable form; when the temperature reaches 170 °C and above, form II is the stable form and form I is the metastable form. The pure structure of MA was reported in 1976 by McConnell;[21] however a disordered structure for form II was reported by Lee et al. in 2006.[13] We have grown form II crystals by annealing form I at 180 °C overnight and collected its single crystal structure, in order to draw precise differences in molecular packing and hydrogen bond nature between these two forms. But this structure comprised of whole-molecule disorder. Crystallographic data are displayed in Table 3-1 and compared with reported structures. The molecular flexibility of C–N–C bond (Figure 3-1) and the presence of both intra and inter molecular hydrogen bonding could be two of the main causes to show polymorphism by this molecule (Figure 3-4 and Figure 3-5). Both forms show the presence of the intra molecular hydrogen bonding between the carbonyl oxygen and the hydrogen of –NH. Similarly, in the intermolecular hydrogen bonding, the carbonyl oxygen of one molecule also interacts with the hydrogen of the carbonyl −OH of the other molecule.

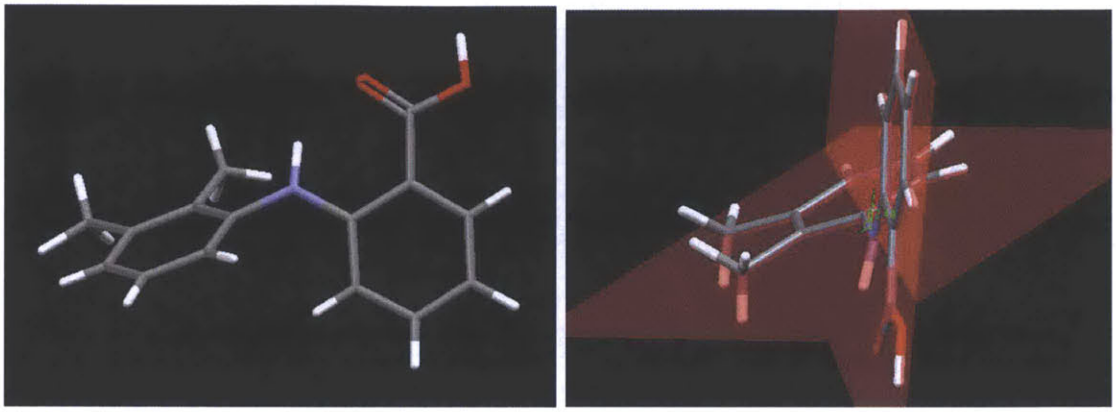

Figure 3-4 Form I of MA. The angle between two ring's planes is 62.44°.

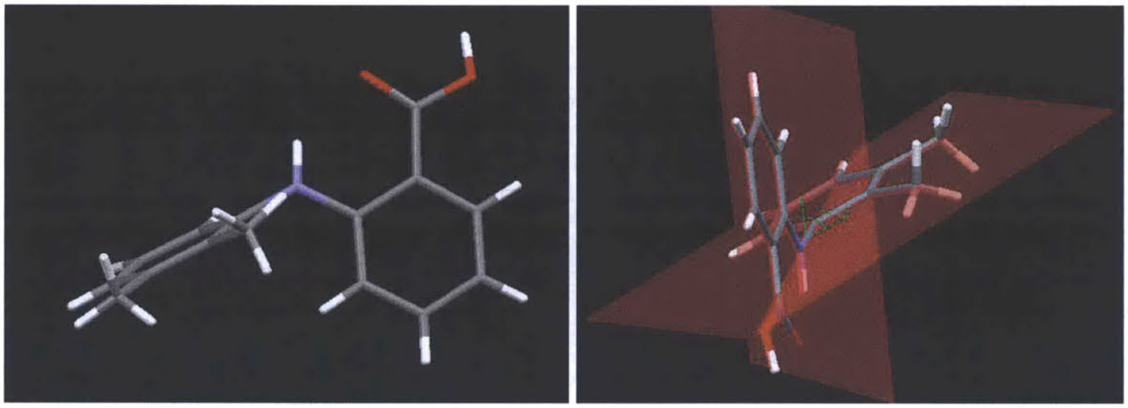

Figure 3-5 Form II of MA. The angle between two ring's planes is -104.72°.

Table 3-1 Crystal data of MA polymorphs

| Parameter | MA form I | MA form II[13] | MA form II (new data) |
|---|---|---|---|
| Crystal system | Triclinic | Triclinic | Triclinic |
| Space group | P-1 | P-1 | P-1 |
| a (Å) | 14.556 | 7.6969 (10) | 7.70630 (10) |
| b (Å) | 6.811 | 9.1234 (10) | 9.10160 (10) |
| c (Å) | 7.657 | 9.4535 (11) | 9.39700 (10) |
| α (°) | 119.57 | 107.113 (7) | 107.2850 (10) |
| β (°) | 103.93 | 91.791 (6) | 91.4080 (10) |
| γ (°) | 91.30 | 101.481 (7) | 101.8040 (12) |
| V ($Å^3$) | 631.766 | 618.89 (13) | 613.454 (12) |
| Z′ | 1 | 1 | 1 |
| R ($F_0$) | 0.045 | 0.052 | 0.0344 |

The two polymorphs structures are very similar in their molecular packing. Inversion related molecules are hydrogen bonded by the carboxylic acid dimer formation [O–H···O, 2.655 Å, 174.12 ° (form I); 2.565 Å, 167.97 ° (form II)] in both structures. In form I, phenyl rings are offset stacking (inter centroid distance 5.007 Å), and C–H···O and C–H···π interactions cover the third dimension molecular packing.

A close examination reveals the carbonyl oxygen–π interaction (C=O···π 3.675 Å), which is similar to anion-π interaction, in form I as shown pictorially in Figure 3-6. The anion-π interactions are non-covalent forces between electron deficient aromatic systems and anions. These interactions are energetically favorable (~20-50 kJ/mol), and are gaining significant recognition over recent years.[22, 23, 24, 25] Similar interactions between the partially negatively-charged carbonyl oxygen atom and the positively-charged phenyl ring center have also been reported before.[26, 27, 28, 29, 30] For example, Vittal and coworkers showed that the C=O···π interaction seems to be responsible for the weakening of hydrogen bonds, thermal dehydration behavior, preventing the formation of new Cu-O bonds in their study of $[Cu_2(sgly)_2(H_2O)]\cdot H_2O$ [$H_2$sgly = N-(2-hydroxybenzyl)glycine].[30] This may also explain why Dimethylformamide (DMF, $HC(=O)N(CH_3)_2$) is the only solvent molecule found by far to produce form II crystals in bulk crystallization experiments.[31] The C=O bond in DMF molecules may interfere the formation of C=O···π interaction in form I crystals and thus push the system to produce form II. In form II, carboxylic acid dimer units are expanded along (-111) plane via C−H···O (2.647 Å; 165.81 °) hydrogen bonds from $CH_3$ to the oxygen of OH group and π···π interaction of phenyl rings (inter centroid distance 3.765 Å). The C−H···O (2.692 Å, 154.88 °) from phenyl ring hydrogen and C−H···π extend the molecular packing into third dimensions (Figure 3-7).

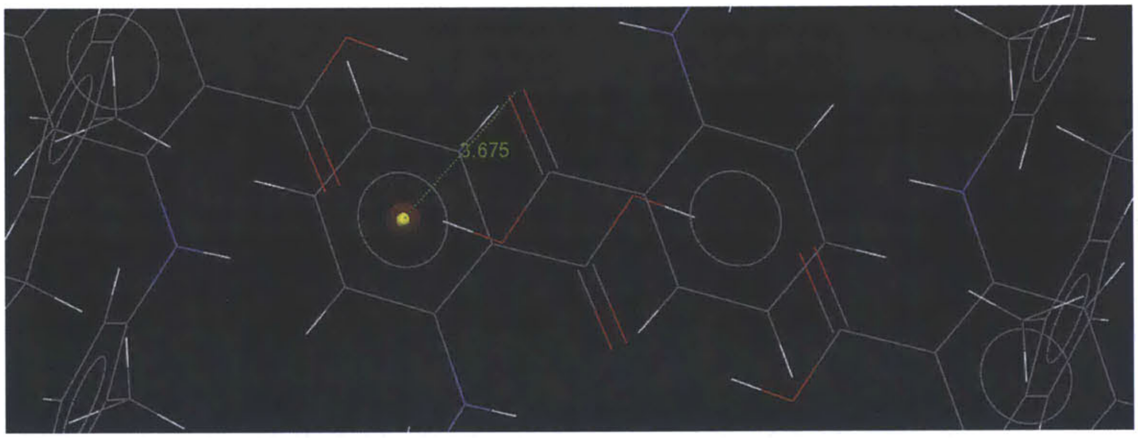

Figure 3-6 Form I C=O···π interaction distance: 3.675 Å.

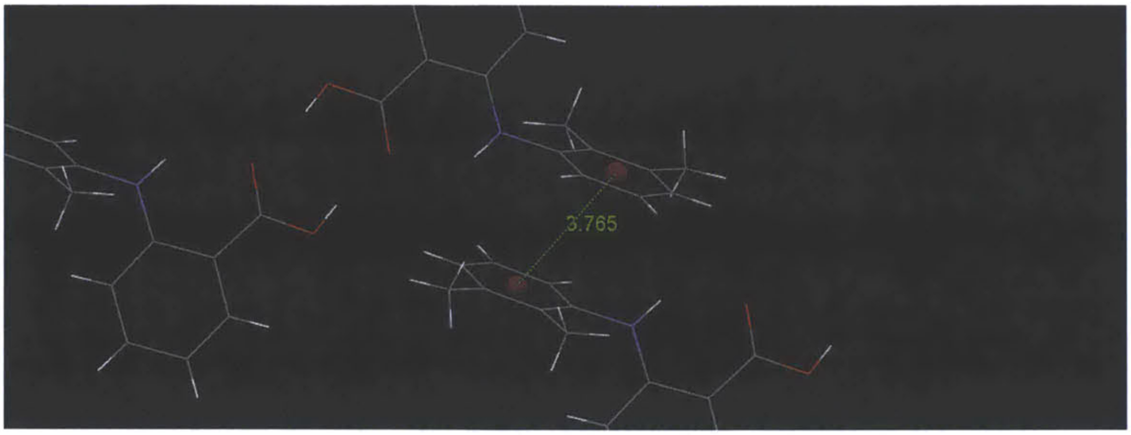

Figure 3-7 Form II π···π interaction inter centroid distance: 3.765 Å.

## 3.4 Selection of SAM Surfaces

A SAM molecule consists of a headgroup, a backbone and an endgroup. The wide choice of backbones and endgroups with various functionalities (e.g. hydrophilicity/hydrophobicity, hydrogen bond donor/acceptor ability) offers great flexibility in the formation of SAMs and has led to a broad range of applications. As previously discussed a number of investigators have demonstrated the use of SAM surfaces to promote the growth of a specified crystal shape, crystal face or polymorph of a crystalline material. These SAMs were selected based on chemical interactions between the SAM surfaces and certain crystal faces of the crystalline material. Given the discussion above, we hypothesized that, by selecting SAMs that may have different chemical interactions with MA molecules, a significant difference on the polymorphic outcome of MA would be observed.

Form I and form II of MA both have carboxylic dimers in their crystal structures. However, the carbonyl group in form I also forms the C=O···π interaction as shown in Figure 6. If we choose a SAM with an endgroup that bond weakly with the carboxylic acid group of the molecule, the residual polarity would favor the formation of the C=O···π interaction observed in form I. Otherwise, a SAM with an endgroup strongly interacting with the carboxylic acid group of the molecule prefers the system to be stabilized by other weak interactions, such as π···π, C–H···π interactions, far away from the carboxylic dimer, observed in form II. Therefore, based on the ability of forming hydrogen bonds with the carboxylic acid group of the MA molecule, we selected the endgroups from strong to weak: pyridine, carboxylic acid group and hydroxyl group (It is found that Pyridine···COOH interaction was preferred over carboxylic acid dimer.[32, 33, 34, 35]). We also chose four more SAMs in order to verify the effect of the backbone length, the number of endgroups and the endgroup orientation on the polymorphic outcome (Figure 3-8).

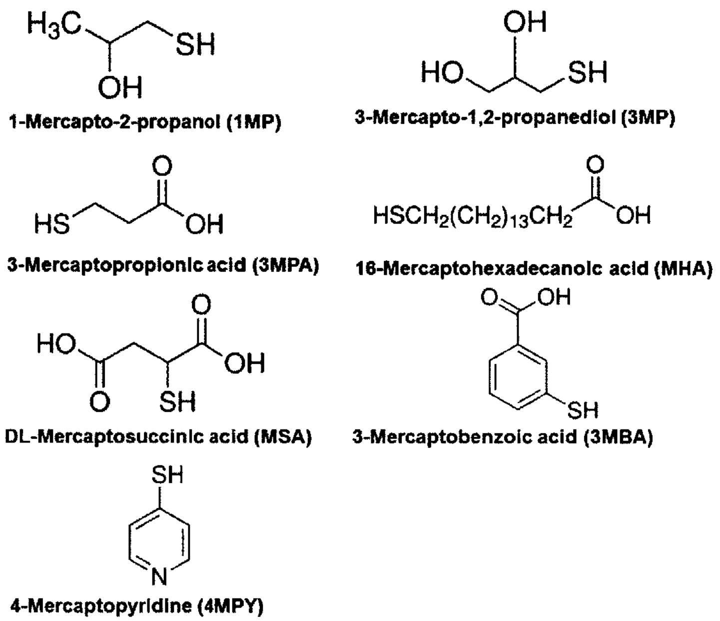

Figure 3-8 Organic thiols SAM molecules with different backbones and different endgroups (–COOH, –OH and pyridine) were chosen for the self-assembled monolayer preparation.

## 3.5 Results and discussion

Concomitant polymorph formation involves the appearance of more than one polymorph of a substance under seemingly identical conditions. Due to the stochastic nature of nucleation, the polymorphs nucleate less frequently are often suppressed by those nucleating more frequently in one crystallization experiment, but the chance of obtaining the rare polymorph can be increased by repeating the experiments. We observed concomitant polymorphism (that is different polymorphs formed on different islands where the islands are at identical conditions) in most cases and the crystals obtained on one substrate are illustrated in Figure 3-9.

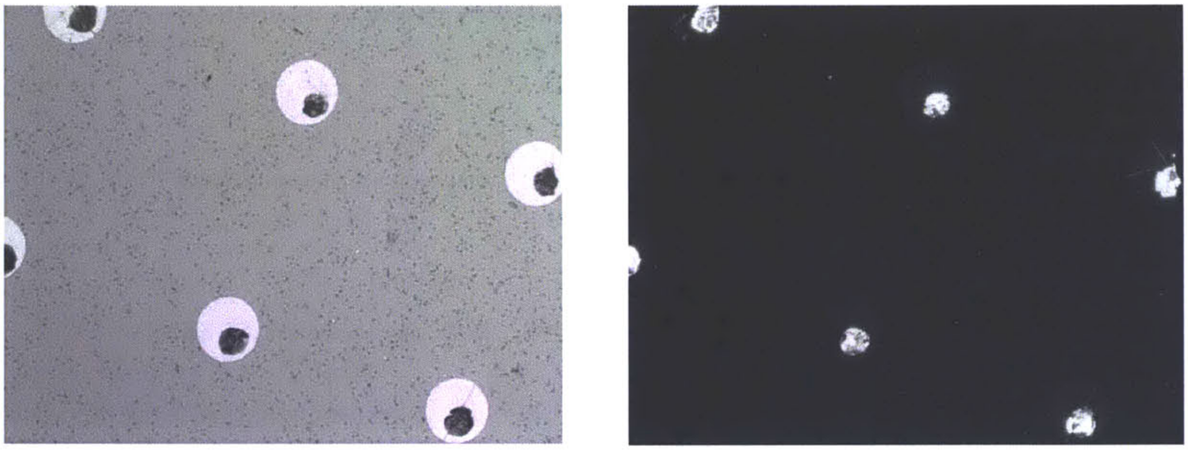
(a) (b)

Figure 3-9 (a) Microscope image under 20X magnification with normal while light, and (b) Image obtained with polarized films in the optical path. Bright spots on islands indicate crystals. Island size is 250 µm.

### 3.5.1 SAMs effect on polymorphism

The effectiveness of the seven chosen SAMs at controlling the polymorphic outcome of MA was measured by determining their effect on the percentages of form I obtained. Nucleation is a stochastic process, and the percentage of form I is an effective way to quantify a SAM's ability to affect the nucleation kinetics. If the SAM lowers the free energy barrier for form II to nucleate, there will be more form II crystals and the percentage of form I will be substantially reduced. At least 100 islands and one crystal on each island were characterized for one experimental condition to ensure statistical accuracy.

The X-ray powder diffraction patterns of crystals obtained on the surfaces of seven SAMs were used to determine the preferred orientation of the (100) face for form I crystals and the (1-10) face for form II. Both crystal faces showed carboxylic acid dimer interactions as we predicted (Figure 3-10 and Figure 3-11).

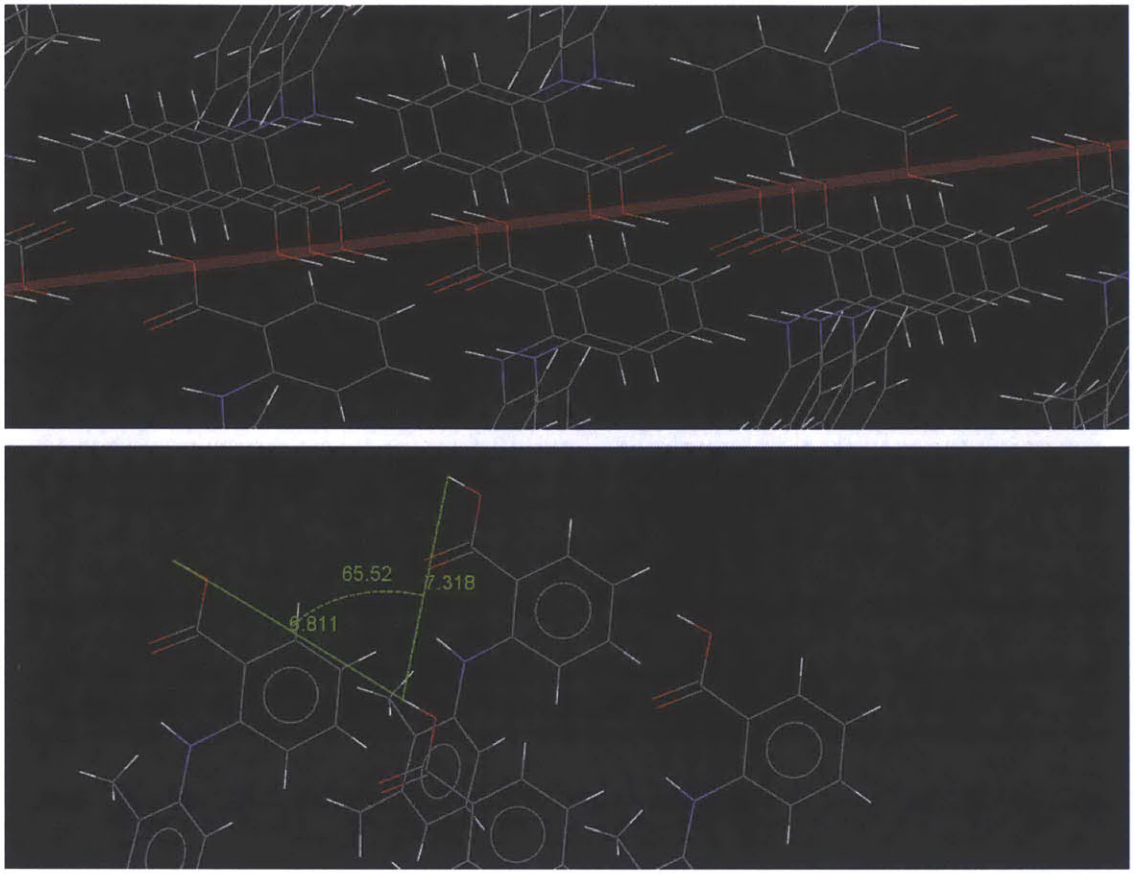

Figure 3-10 Form I (100) plane lattice parameters: 6.811 Å × 7.318 Å.

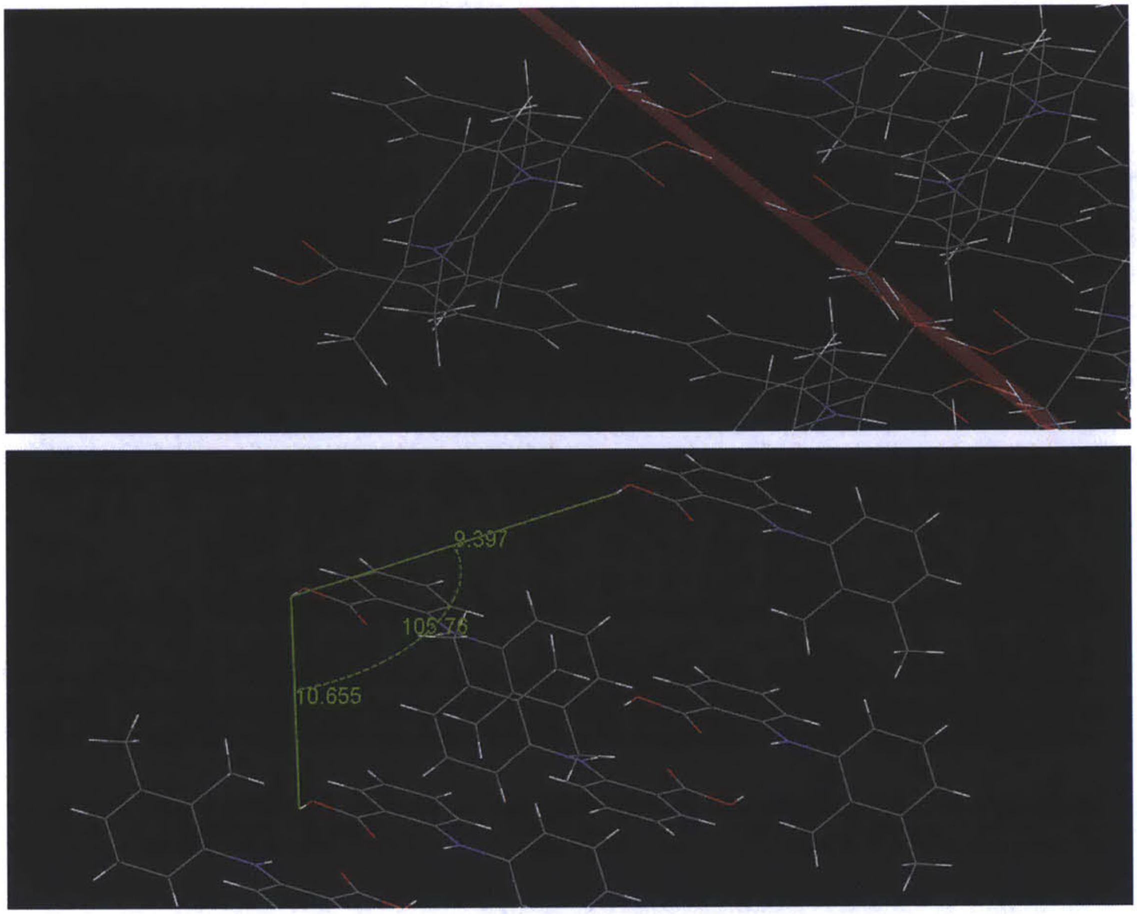

Figure 3-11 Form II (1-10) plane lattice parameters: 9.397 Å × 10.655 Å.

The percentages of form I crystallized on the seven SAM surfaces were plotted in Figure 3-12. At 25 °C, approximately 10% of crystals obtained on the 4MPY, 3MBA, MHA and 3MPA surfaces were form I. On the other hand, crystals obtained on the 1MP and 3MP surfaces contained 22.7% and 28.6% form I, respectively. This demonstrates that, as predicted, SAMs with the pyridine or carboxylic acid endgroup produced more form II and less form I than SAMs with the hydroxyl endgroup. Almost the same percentages of form I on MHA and 3MPA surfaces indicated that the backbone length did not significantly affect the nucleation kinetics and the polymorphic outcome. A 5.9% difference between 1MP and 3MP implied that an increase in hydroxyl endgroup density promoted more form I nucleation. We also explored the orientation effect of SAMs on the polymorphic outcome of MA. It is found that 3MBA with a slightly tilted carboxylic acid endgroup showed almost the same results as 3MPA and MHA. However, MSA generated significant different results from these three SAMs. The findings are also consistent with the results at 5°C. We also detected two unusual Raman spectra which may imply two unknown polymorphs of MA (Spectra in the appendix). More than four thousand spectra were measured. Unknown form I was found 3 times and unknown form II 5 times. Since nucleation is a stochastic process, it is possible that some rare polymorphs are detected when a large number of identical experiments are conducted. This was previously demonstrated in our work on ROY.[36] It is difficult to determine if these polymorphs are a result of the SAM substrate or simply the result of the large number of experiments and the slow rate of conversion of a metastable form to a stable form when attached to a surface.

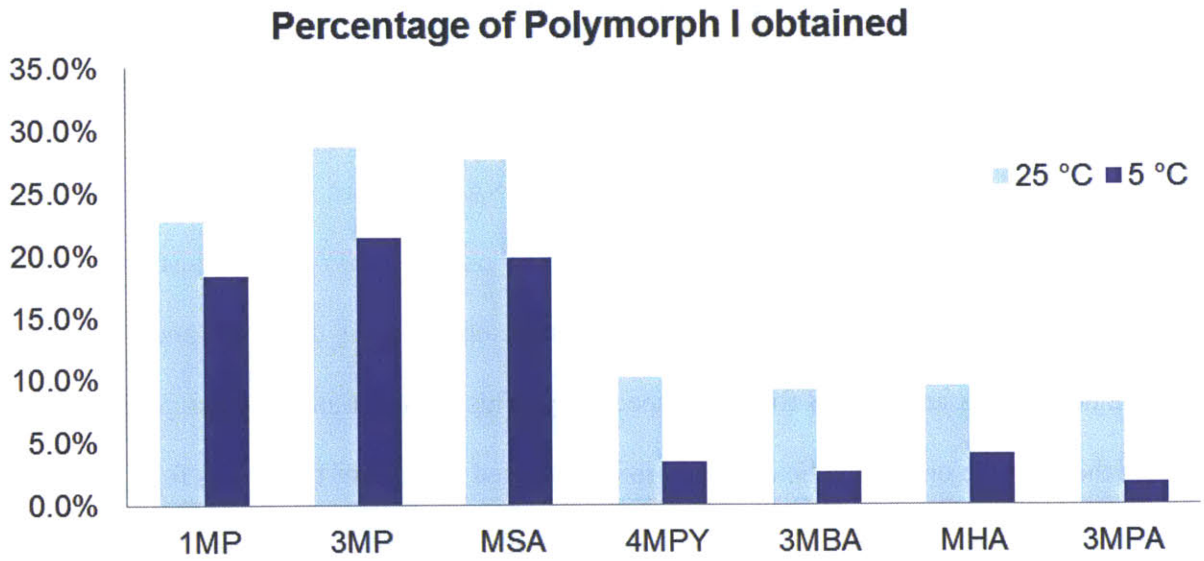

Figure 3-12 Polymorphic outcomes of MA crystals on different SAMs islands at 5°C (deep blue) and 25°C (light blue). Island size: 250 µm. 3.0 mg/g MA ethanol solution was used.

Compared to the 3MPA surface, the MSA surface produced ~ 20% more polymorph I at 5°C and 25°C, as shown in Figure 3-12. This was likely due to the orientation effect. A schematic diagram (Figure 3-13) of MSA and 3MPA depicted that the carboxylic acid group in 3MPA was fully exposed to the outer space while the carboxylic acid group of MSA was either pointing towards or sitting parallel to the surface. Therefore, the carboxylic acid groups of MSA might not have formed carboxylic acid dimers as 3MPA, but acted as the hydroxyl groups of 1MP and 3MP which favored the formation of form I.

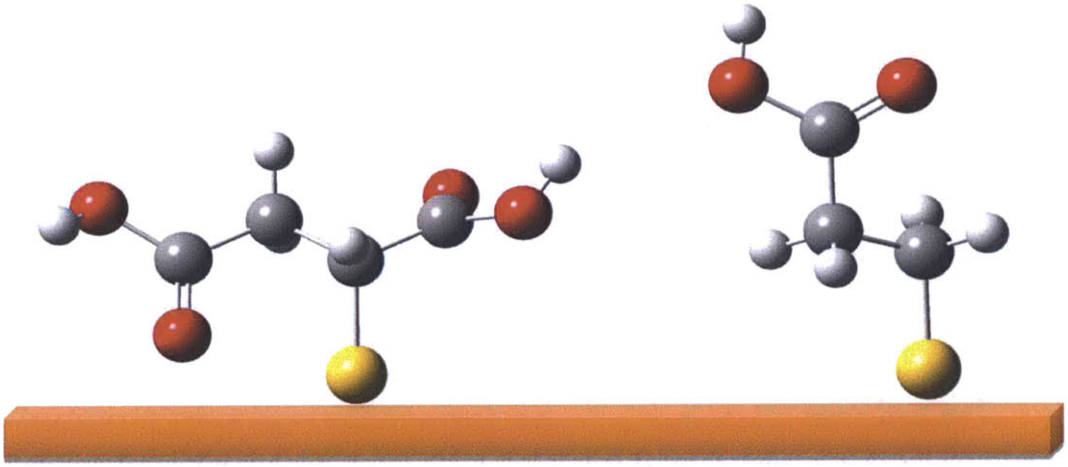

Figure 3-13 Example graphs of DL-mercaptosuccinic acid (MSA) and 3-Mercaptopropionic acid (3MPA) adsorbed on the gold surface. Inward orientation of carboxylic acid groups of MSA blocks the formation of carboxylic acid dimers between MA and the SAM surface.

The degree of lattice matching between the SAMs and crystal faces was evaluated using EpiCalc Version 5.0.[37, 38, 39] The software uses a dimensionless potential ($V/V_0$) to represent the degree of the lattice matching. $V/V_0$ = 1, 0.5, 0 and -0.5 mean incommensurism, coincidence, commensurism on a nonhexagonal substrate lattice and commensurism on a hexagonal substrate, respectively.

Past studies demonstrated that n-alkanethiol (n>9) SAMs on Au(111) surfaces consisted of $(4\times 2)$ superlattices of a basic $(\sqrt{3}\times\sqrt{3})$R30° dense-packed monolayers.[40, 41] For short-backbone alkanethiol SAMs, the lateral van der Waals forces among the backbones were not strong enough to align the tails in parallel and thus they were less organized. Rhee and coworkers tested the SAM of 1-mercapto-2-propanol (1MP) and observed the striped structure of $(2\sqrt{3}\times\sqrt{3})$R30°.[41] Giz et al. found that the 3-mercaptopropionic acid (3MPA) molecules packed into several phases on the surface. The most dominant phase was an incommensurate $p\times\sqrt{3}$ structure, where p is an irrational number for a truly incommensurate phase or a very large integer for a higher order commensurate phase.[42] A simplified calculation is shown below when p is chosen to be 100. The results are presented as the optimal orientation of crystal lattice (θ) on the SAMs surface and the corresponding $V/V_0$ minimum. For form I(100)/3MPA: $\theta = 36.25°$, $V/V_0 = 0.71$, form II(1-10)/3MPA: $\theta = 138.25°$, $V/V_0 = 0.96$, form I(100)/1MP: $\theta = 167.75°$, $V/V_0 = 0.93$, and form II(1-10)/1MP: $\theta = 23.25°$, $V/V_0 = 0.75$. These results indicate that 3MPA favors form I rather than form II while 1MP prefers form II than form I. However, our experimental results showed the opposite trend. Therefore, it is reasonable to conclude that the effect of chemical interactions of the SAM surfaces on promoting nucleation is more predominant than the lattice matching factor for the heterogonous nucleation of MA. This conclusion is consistent with some others' recent work. Chadwick et al. focused on nucleation of acetaminophen on various crystalline surfaces and found that surface functionality matched substrates significantly decreased the induction time of acetaminophen even when other substrates showed better lattice matching.[43] Ward and coworkers studied trans-cinnamic acid, glycine, 5-methyl-2-[(2-nitrophenyl)amino]-3-thiophenecarbonitrile (ROY) and sulfanilamide on 5 different crystalline substrates and concluded that in select cases chemical interactions dominate the nucleation over lattice matching.[44]

### 3.5.2 Solvent effect on polymorphism

Similar trends were also observed with methanol as the solvent (Figure 14), but the percentages of form I are slightly lower. The solubility of MA in methanol (4.67±0.08 mg/g) is lower than that in ethanol (5.13±0.05 mg/g). When applying the same initial concentrations, the supersaturation in methanol is actually higher than that in ethanol. As shown in Figure 3-14, the higher supersaturation favors less form I and produces more metastable form II.

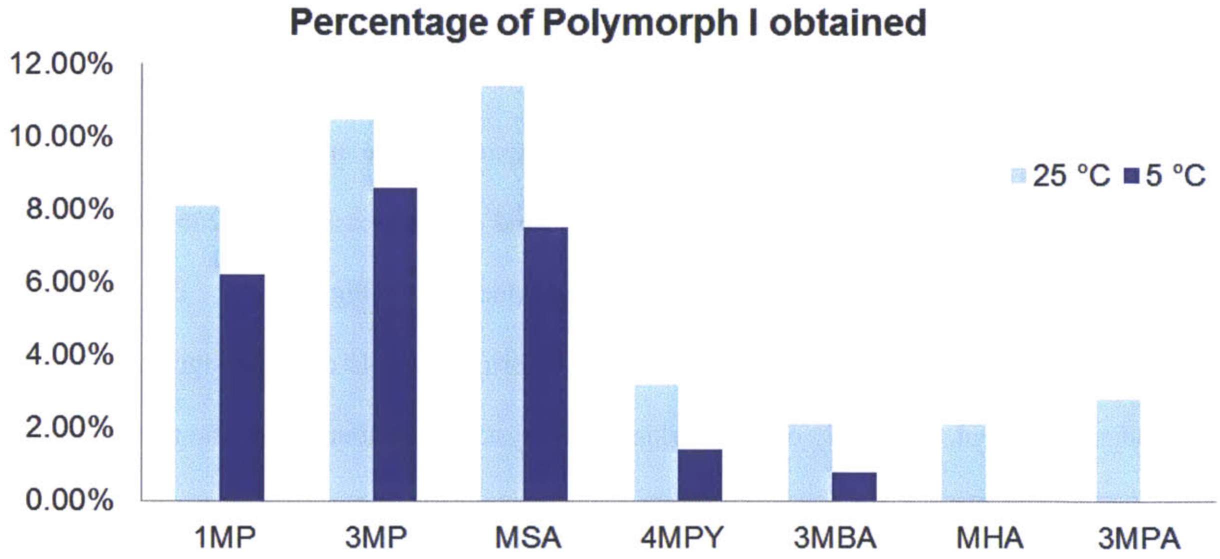

Figure 3-14 Polymorphic outcomes of MA crystals on different SAMs islands at 5°C (deep blue) and 25°C (light blue). Island size: 250 µm. 3.0 mg/g MA methanol solution was used. Bars not shown represent 0% form I crystals were obtained under that experimental condition.

### 3.5.3 Temperature effect on polymorphism

The temperature effect is complex. When the temperature drops, the solubility of MA in ethanol/methanol will also reduce. Since the initial concentration is the same as used at 25°C, the supersaturation is therefore increased. As discussed above, higher supersaturation favors the metastable form II. However, evaporation rate also decreases as the temperature goes down. This allows droplets to reach higher supersaturation in a slow pace, and thus more form I crystals tend to form. Our experimental results showed that lower temperature 5 °C consistently produced more form II than 25 °C. This implied that the temperature effect on solubility was more important than the temperature effect on evaporation rate in this scenario.

### 3.5.4 Island size effect on polymorphism

According to the Young-Laplace equation, vapor pressure near droplet surface increases as droplet size decreases. Therefore, the driving force to evaporate increases and evaporation is accelerated to achieve high supersaturation more quickly. The metastable form II is more favorable due to the kinetic factor. In our work, island size decreased from 250 μm to 100 μm and further to 1 μm. Experiments were conducted under 25°C (Figure 3-15). The results were consistent with the prediction. The percentages of form I crystals dropped significantly as the island size reduced. Especially on 1 μm islands, all crystals were found to be the metastable form II.

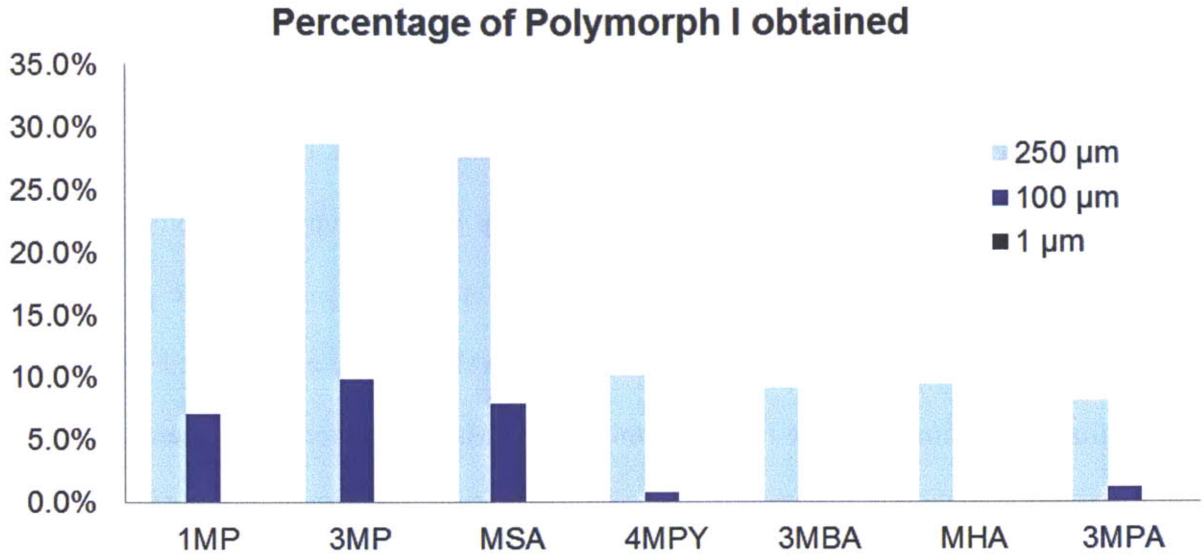

Figure 3-15 Polymorphic outcomes of MA crystals on different SAMs islands at 25°C. Island size: 250 µm (light blue), 100 µm (deep blue) and 1 µm (black). 3.0 mg/g MA ethanol solution was used. Bars not shown represent 0% form I crystals were obtained under that experimental condition.

### 3.5.5 Concentration effect on polymorphism on 1µm islands

According to Figure 3-15, 100% form II crystals were obtained on 1 µm islands regardless of which SAM was used. This implied that on 1 um islands, the initial concentration (3.0 mg/g) was too high and predominantly produced the metastable form II. In order to see the effect of SAMs, MA solutions of decreased concentrations (1.0 mg/g and 0.3 mg/g) were used. The differences on polymorphic outcomes among various SAM surfaces were observed for these decreased concentrations as shown in Figure 3-16 and Figure 3-17. Compared to the results starting with 1.0 mg/g, those starting with 0.3 mg/g produced significantly higher percentages of form I. These results can also be explained by the Ostwald's rule of stages. Droplets with higher initial concentrations had less time to reach a high supersaturation and thus preferably produced the metastable form II. On the contrary, droplets with a lower initial concentration had more time and reorganized molecules into the stable form I. These results also implied that the effect of SAMs on polymorphs was only significant for a certain range of the supersaturation. Above the range, the supersaturation directed the system to the metastable form II regardless of which SAM was on the surface. Similar results on the relationship between supersaturation and SAMs on polymorphic outcomes were also reported by Zhang et al.[20] They studied the polymorphs of tolbutamide (TB) crystallized on three different SAM surfaces and showed that TB only crystallized into form II on the methyl-terminated SAMs and trifluoromethyl-terminated SAMs at low supersaturations.

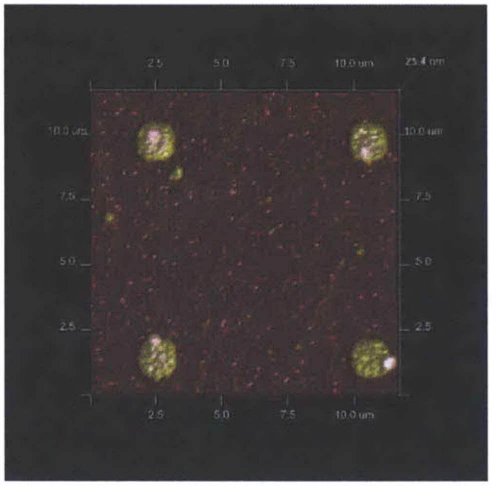

Figure 3-16 AFM image: MA crystals were obtained on 1 μm islands. Crystal size is ~ 300 nm.

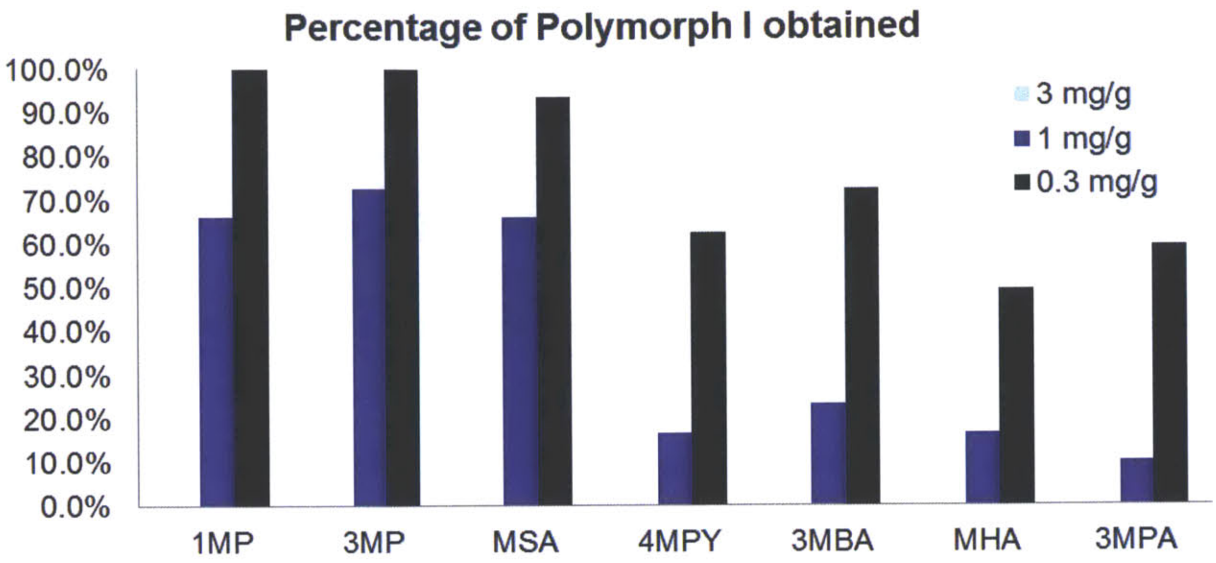

Figure 3-17 Polymorphic outcomes of MA crystals on different SAMs islands at 25°C. Island size: 1 μm. MA ethanol solution concentration: 3.0 mg/g (light blue), 1.0 mg/g (deep blue) and 0.3 mg/g (black). Crystal size is ~ 300 nm. Bars not shown represent 0% form I crystals were obtained under that experimental condition.

## 3.6 Conclusion

The control of polymorphism in crystallization is a crucial topic in the pharmaceutical industry as is the ability to produce crystals of small sizes (below 1 micron) of a desired crystalline form. Our work examined the role of the seven different SAMs on the polymorphic outcome of MA crystallization on patterned surfaces.

The results suggested that the SAMs forming strong interactions with the carboxylic acid group of MA molecules depleted its polarity and pushed the system to form π···π and C–H···π interactions, which lowered the free energy barrier of nucleation and promoted growth of form II. The formation of the chemical interactions was strongly affected by the orientation. For example, the carboxylic acid groups of MSA could not form strong chemical interactions with the MA molecules. By increasing the number of the SAM endgroups, the sites for chemical interactions would be increased to promote nucleation, such as 3MP. Based on lattice matching calculations employing Epicalc software, it is reasonable to conclude that the chemical interactions were more important than the lattice matching effect.

We also explored the effects of temperature, solvent, droplet size and concentration on the polymorph control of MA. Regardless of which factor among these four was changing, it was always related to the supsaturation change in the droplets. Our results also pointed out that the effect of SAMs on polymorphs was not dominant for MA, and worked in a certain range of supersaturation. Finally, we demonstrated the ability to make crystals as small as ~ 300 nm and exclusively produce either form of MA by applying our knowledge developed above.

## 3.7 Reference

1. J. Bernstein, *Polymorphism in Molecular Crystals*, Oxford University, 2002.
2. J. T. Carstensen, *Pharmaceutics of Solids and Solid Dosage Forms*, John Wiley & Sons, 1977.
3. F. Wohler, J. Liebig, *Ann. Pharm.*, 1832, **3**, 249.
4. J. Haleblian, W. McCrone, *J. Pharm. Sci.*, 1969, **58**, 911.
5. J. Bernstein, *J. Phys. D: Appl. Phys.*, 1993, **26**, B66.
6. A. J. Aguiar, J. Krc Jr, A. W. Kinkel, J. C. Samyn, *J. Pharm. Sci.*, 1967, **56**, 847.
7. J. Guo , J. Ulrich, *Cryst. Res. Technol.*, 2010, **45**, 267.
8. M. Lahav, L. Leiserowitz, *J. Phys. D: Appl. Phys.*, 1993, **26**, B22.
9. R. J. Davey, N. Blagden, G. D. Potts, R. J. Docherty, *J. Am. Chem. Soc.*, 1997, **119**, 1767.
10. A. Singh, I. S. Lee, K. Kim, A. S. Myerson, *Cryst. Eng. Comm.*, 2011, **13**, 24.
11. A. Y. Lee, A. S. Myerson, *MRS Bull.*, 2006, **31**, 881.
12. R. Hilfiker, *Polymorphism in the Pharmaceutical Industry*, John Wiley & Sons Inc., 2006.
13. E. H. Lee, S. R. Byrn, T. M. Carvajal, *Pharm. Res.*, 2006, **23**, 2375.
14. J. Aizenberg, J. A.Black, G. M. Whitesides, *Nature*, 1999, **398**, 495.
15. A.Y. Lee, A. Ulman, A. S. Myerson, *Langmuir*, 2002, **18**, 5886.
16. R. Hiremath, J. A. Basile, S. W. Varney, J. A. Swift, *J. Am. Chem. Soc.*, 2005, **127**, 18321.
17. J. R. Cox, L. A. Ferris, V. R. Thalladi, *Angew. Chem. Int. Ed.*, 2007, **46**, 4333.
18. B. Pokroy, F. V. Chernow, J. Aizenberg, *Langmuir*, 2009, **25**, 14002.
19. C. Capacci-Daniel, K. J. Gaskell, J. A. Swift, *Cryst. Growth Des.*, 2010, **10**, 952.
20. J. Zhang, A. Liu, Y. Han, Y. Ren, J. Gong, W. Li, J. Wang, *Cryst. Growth Des.*, 2011, **11**, 5498.
21. J. F. McConnell, F. Z. Company, *Cryst. Struct. Commun.*, 1976, **5**, 861.
22. P. Gamez, T. J. Mooibroek, S. J. Teat, J. Reedijk, *Acc. Chem. Res.*, 2007, **40**, 435.
23. I. Alkorta, I. Rozas, J. Elguero, *J. Am. Chem. Soc.*, 2002, **124**, 8593.
24. D. Quinonero, C. Garau, C. Rotger, A. Frontera, P. Ballester, A. Costa, P. M. Deya, *Angew. Chem., Int. Ed.*, 2002, **41**, 3389.
25. M. Mascal, A. Armstrong, M. D. Bartberger, *J. Am. Chem. Soc.*, 2002, **124**, 6274
26. L. Addadi, M. Lahav, *Pure Appl. Chem.*, 1979, **51**, 1269.
27. J. Bernstein, M. D.Cohen, L. Leiserowitz, *In the Chemistry of Quinonoid Compounds*, J. Wiley & Sons, 1974.
28. K. Ueno, H.Nakanishi, M. Hasegawa, Y. Sasada, *Acta Crystallogr.*, 1978, **B34**, 2034.
29. J. N. Moorthy, S. D. Samant, K. Venkatesan, *J. Chem. Soc. Perkin Trans.* 1994, **2**,1223.
30. X. Yang, D. Wu, J. D. Ranford, J. J. Vittal, *Cryst. Growth Des.*, 2005, **5**, 41.
31. C. E. Nicholson, S. J. Cooper, *Crystals*, 2011, **1**, 195.
32. J. Y. Lee, P. C. Painter, M. M. Coleman, *Macromolecules*, 1988, **21**, 954.
33. T. R. Shattock, K. K. Arora, P. Vishweshwar, M. J. Zaworotko, *Cryst. Growth Des.*, 2008, **8**, 4533.
34. N. Shan, A. D. Bond, W. Jones, *Cryst. Eng.*, 2002, **5**, 9.

35. R. D. B. Walsh, M. W. Bradner, S. Fleischman, L. A. Morales, B. Moulton, N. Rodríguez-Hornedo, M. J. Zaworotko, *Chem. Commun.*, 2003, 186.
36. A. Singh, I.S. Lee and A.S. Myerson, *Crystal Growth and Design,* 2009, **9**, 1182.
37. A. C. Hillier, M. D. Ward, *Phys. Rev. B,* 1996, **54**, 14037.
38. J. A. Last, D. E.Hooks, A. C. Hillier, M. D. Ward, *J. Phys. Chem. B,* 1999, **103**, 6723.
39. http://www.nyu.edu/fas/dept/chemistry/wardgroup/software.php
40. M. J. Giz, B. Duong, N. J. Tao, *J. Electroanal. Chem.,* 1999, **465**, 72.
41. G. E. Poirier, M. J. Tarlov, *Langmuir*, 1994, **10,** 2853.
42. C. K. Rhee, Y. N. Kim, *Appl. Surf. Sci.*, 2004, **228**, 313.
43. K. Chadwick, J. Chen, A. S. Myerson, B. L. Trout, *Cryst. Growth Des.,* 2012, **12**, 1159.
44. B. K.Olmsted, M. D. Ward, *Cryst. Eng. Comm.,* 2011, **13**, 1070.

## 3.8 Appendix

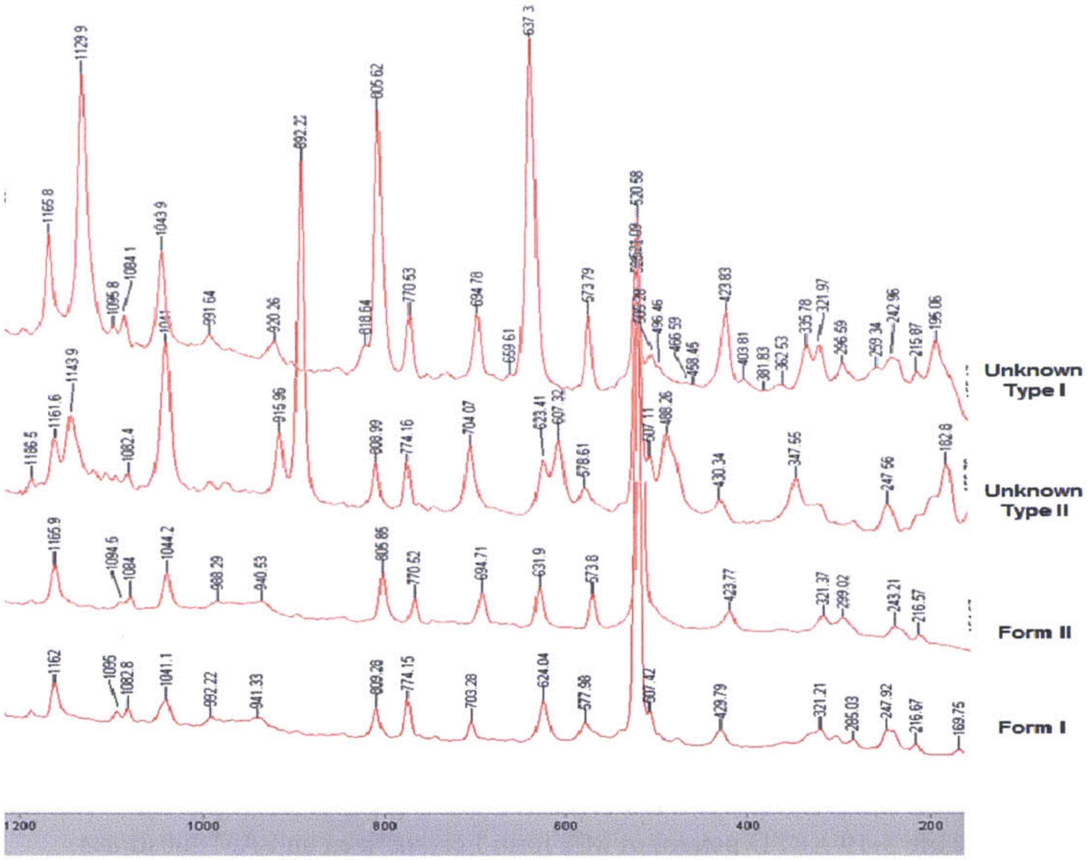

Figure 3-18 Raman spectra of mefenamic acid form I and II. Two unknown polymorphs (type I and type II) were detected during the experiments.

Substrates with form I was prepared by immersing SAM substrate in solution for evaporation crystallization. And therefore, the crystals are big and the signal is much strong. Compared with the calculated pattern, the preferred orientation is (100).

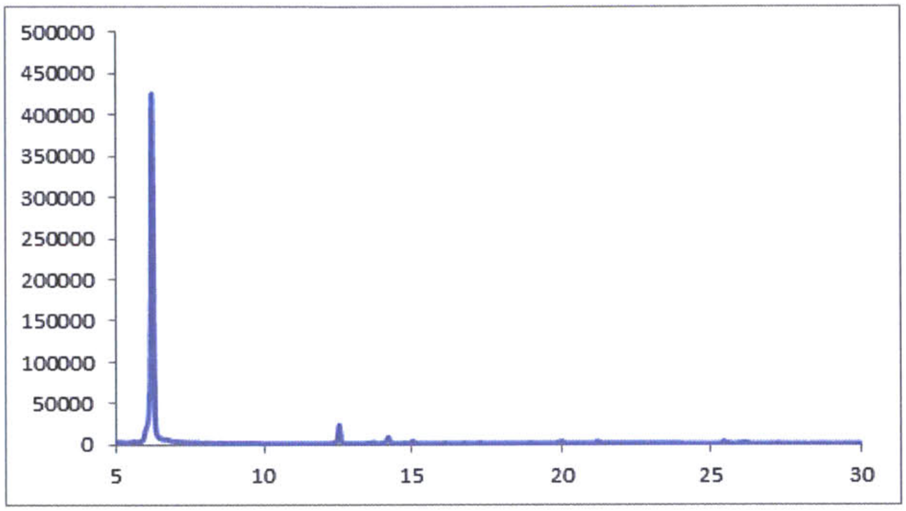

Figure 3-19 XRPD pattern of MA form I crystallized on SAM substrates.

Substrates with all form II was scanned as below. Compared with the calculated pattern, the preferred orientation is (1-10).

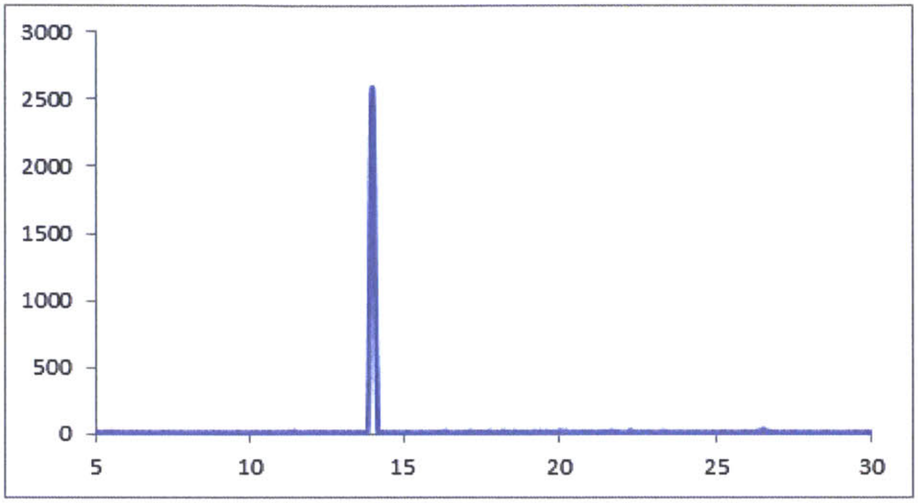

Figure 3-20 XRPD pattern of MA form II crystallized on SAM substrates.

# 4 FORMATION OF ORGANIC MOLECULAR NANOCRYSTALS UNDER SOFT CONFINEMENT

Methods to produce nano-sized organic molecular crystals are of great interest in the pharmaceutical industry due to the potential of increasing the solubility of poorly soluble drugs. One method of direct formation of organic nanocrystals is by crystallization in confined environments where the overall crystallization volume is constrained. In this work, we report the use of a novel solution impregnation method to form nanocrystals in polymer matrices with various microstructures in order to systemically study the role of soft confinement and polymer chemistry on the nucleation process of nano-sized crystals. We demonstrate that the direct nano-crystallization in the polymer matrices can produce nanocrystals as small as 100 nm. The particle diameter correlates significantly with the microstructure of the polymer matrices and the nucleation kinetics. In addition, by carefully choosing the right experimental conditions and the polymer matrix, polymorph control of nanocrystals could be achieved. Solid state NMR was used to examine the local structure of nanocrystals inside the polymer matrices as well as crystal polymer interactions.

## 4.1 Introduction

In recent years, interest in nanocrystals of organic molecular crystals has increased dramatically particularly in the pharmaceutical industry. It is estimated that 40% or more of compounds identified through combinatorial screening exhibits poor aqueous solubility.[1, 2] Formulating these compounds as nanocrystals may potentially increase their bioavailability.[3, 4] As crystal size decreases, surface-to-volume (s/v) ratios greatly increase and thus the dissolution rate will be strongly enhanced.[5] In addition, as the Ostwald-Freundlich equation predicts, the solubility of nano-sized crystals smaller than 1 μm is much higher than that of larger bulk crystals.[6] Kim *et al.* demonstrated 31.7% solubility enhancement of β-glycine nanocrystals of which the equivalent radius is 244 nm.[7] Wang *et al.* showed that cabmazepine form III nanocrystals of ~ 320 nm in diameter exhibited a 26.4% increase in their solubility.[7, 8] Methods to produce organic molecular nano-sized crystals have been widely studied. Based on the crystal formation process, methods to form nano-crystals can be divided into two categories: "top down" and "bottom up"[1]. "Top down" methods refer to those that break large crystals into smaller ones, such as milling and high pressure homogenization. However, the introduction of impurities, high energy consumption, and possible polymorph transformation are major drawbacks of these approaches. "Bottom up" methods refer to those that aggregate single molecules into nano-scale crystals, such as emulsification[9, 10], supercritical fluid crystallization[11, 12], impinging jet crystallization[13, 14], and confined crystallization. However, the high supersaturation and/or high intensity mixing involved make control of crystal size and polymorphs difficult. Microfluidic devices are also used to produce nanocrystals with uniform size distribution, but these devices experience channel clogging, which affects the continuous mass production of crystals.[15-17]

Nano-crystallization in many types of confinements has been reported in the literature. Previous studies have employed rigid inorganic porous materials such as controlled pore glasses[18-20], mesoporous silica[21] and zeolites[22]. Another option is the use of soft confinement using materials such as porous polymers. Ward and coworkers reported using porous polystyrene-poly(dimethyl acrylamide) (p-PS-PDMA) monoliths to obtain nano-sized crystals of β-glycine, 2,2,3,3,4,4-

hexafluoro-1,5-pentanediol and (R)-(+)-3-methyladiapic acid.[18, 19] Diao *et al.* used polymer gels with tunable microstructures and polymer nano-pores of different shapes and angles to control nucleation kinetics and polymorphic outcomes.[23-25] In this work, we present a novel bottom-up means of producing nanocrystals in polymer matrices, for understanding the nucleation and crystal growth mechanism of organic molecular nanocrystals formed inside soft confined environments. The polymer matrices are composed of cross-linked cellulose/cellulose acetate polymer fibers with various pore sizes. We propose that by varying the microstructures of these polymer matrices nano-sized crystals with controlled polymorphic outcome can be obtained and stabilized.

## 4.2 Experimental section

### 4.2.1 Materials

Glycine (ReagentPlus®, ≥99%), acetaminophen (BioXtra®, ≥99.0%), ibuprofen (≥98%) and water (CHROMASOLV®, for HPLC) were purchased from Sigma Aldrich. Deferasirox was a gift from Novartis. Porous cellulose membranes (Whatman®, pore size 0.2/0.45/1 μm, thickness 75 μm) and cellulose acetate membranes (Whatman®, pore size 0.2/0.45/0.8/1.2 μm, thickness 140 μm) were purchased from GE Healthcare Life Sciences. Ethanol (200 proof) was purchased from VWR.

### 4.2.2 X-Ray Powder Diffraction (XRPD) Analysis

The instrument (X'Pert PRO, PANalytical Inc.) is equipped with a PW3050/60 standard resolution goniometer and a PW3373/10 Cu LFF DK241245 X-ray tube. The high tension generator high voltage and anode current were set at 45 kv and 40 mA. A spinner sample stage PW3064 (Reflection mode) was used for all the samples. Settings on incident bean path include: soller slit 0.04 rad., mask fixed 10 mm, programmable divergence slit and fixed 1° anti-scatter slit. Settings on diffracted beam path include: soller slit 0.04 rad and programmable anti-scatter slit. The scan was programmed as a continuous scan: $2\theta$ angle 2-40°, step size 0.0083556°, time per step 19.685 s; three repeated scans were collected to average.

### 4.2.3 Differential Scanning Calorimetry (DSC) Analysis

The instrument (Q2000, TA instruments) is connected with nitrogen gas to maintain a flow rate of 50 ml/min in order to create an inert gas environment in the sample chamber. An extra refrigerated cooling system (RCS 40, TA instruments) is used to extend the available temperature range between -40 and 400 °C. Tzero® pan and lid were used. A heating/cooling rate of 5°C/min was applied and different initial/final temperatures were set for different compounds. For example, we used 20 -80 °C for ibuprofen since its melting point is ~75 °C.

### 4.2.4 Solid-state Nuclear Magnetic Resonance (ssNMR) Methods

Solid-state magic-angle spinning (MAS) NMR experiments were conducted on a home-built 500 MHz spectrometer (courtesy of Dr. Dave Ruben, FBML) using either a 3.2 mm or a 4 mm

Varian triple resonance ($^{1}$H/$^{13}$C/$^{15}$N) probe. For the cross-polarization (CP) experiments,[26] the contact time was 2.0 ms at $\nu_{rf}$ of 83 kHz and the MAS frequency was between 10 and 13.5 kHz. The $^{1}$H $T_1$ was measured either by the inversion-recovery[27] or the saturation recovery[28] sequence. All experiments utilized the two pulse phase modulation (TPPM)[29] proton decoupling sequence. The recycling time for ibuprofen samples was 5 s, and for the acetaminophen samples was 120 s. The number of scans was up to 4096 depending on the signal to noise. The $^{13}$C MAS NMR data was referenced to 40.49 ppm using solid adamantane with respect to DSS (0 ppm). Quantification of API polymorphs from CPMAS spectra was performed following the procedure published by Offerdahl et al.[30]

### 4.2.5 Scanning Electronic Microscope (SEM) imaging

The matrix cross-section imaging by SEM is challenging since the polymer matrix is not conductive. We were also concerned that a large portion of nanocrystals near the cross-sectioned part may be lost due to cutting, unintentional shaking or sudden exposer to environmental humidity. Therefore we applied cyro-cutting techniques to freeze the sample before cutting to best maintain the micro-structures of nanocrystals within the matrix: (1) we put the sample into a 1 L Thermo-Flask™ benchtop liquid nitrogen containers which was half filled with liquid nitrogen for ~ 30 minutes. (2) The sample was quickly transferred onto two wooden supports with a 5-mm gap in between, and the sample was easily cracked into two pieces when a tweezer tip was pressed onto the very brittle sample; (3) One piece was then coated with a ~20 nm gold thin film for creating a conductive surface of the sample under the SEM; (4) The sample was attached onto a vertical support on a special Aluminum SEM sample holder (Electron

Microscopy Sciences, catalog 75344) with the cracked cross-sectioned part facing upwards. (5) A JEOL® 6700F SEM (A cold field-emission gun scanning electron microscope) was operated for obtaining the images.

### 4.2.6 Experimental set-up

Nano Plotter (Model NP2.1, GeSim Germany) was used for uniformly dispersing solution droplets onto a porous matrix. The instrument is able to disperse a desired number of droplets onto any desired spot by micromachined piezoelectric micropipettes. Based on the porosity of the matrix and the affinity of the solution for the matrix, we experimented and designed programs in order to disperse solution droplets uniformly onto the matrix without residual solution on the surface. Key parameters that vary for different solutions include solution concentration, the number of droplets per spot and step size between spots. Nano Plotter also includes an enclosure in which an open beaker containing a solution of a certain concentration can be placed to control the relative vapor pressure. For example, raising the vapor pressure of ethanol may slow down the evaporation and crystallization of acetaminophen/ethanol solution, and thereby promoting the production of a more stable polymorphic crystalline form.

## 4.3 Results and discussion

We selected glycine (GLY), ibuprofen (IBP), acetaminophen (APAP) and deferasirox (DFX) as model compounds to represent active pharmaceutical ingredients (APIs) from simple to complex, as shown in Figure 4-1. GLY has a total of six different polymorphs while three of them were obtained under room temperature and pressure conditions (i.e, α, β and γ). IBP was reported as having two polymorphs (I and II), but the second polymorph was only successfully produced in a very small amount (milligrams) with a complicated heating/quenching loop[31]. APAP possesses three different polymorphs (I, II and III): form I is the most stable and commercially formulated form. DFX was reported to have five polymorphs (I-V), and the most stable form (polymorph I) is chosen in the marketed formulation.

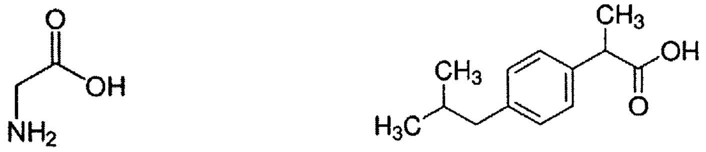

Glycine (GLY, 6 polymorphs) Ibuprofen (IBP, 2 polymorphs)

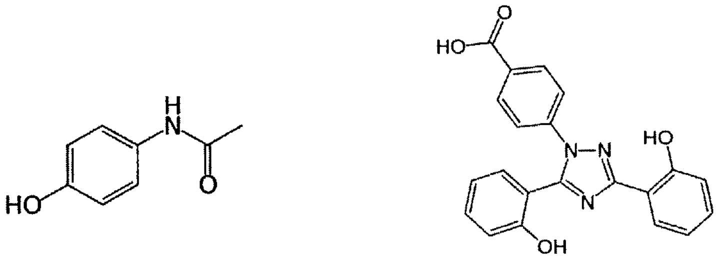

Acetaminophen (ATP, 3 polymorphs) Deferasirox (DFX, 5 polymorphs)

Figure 4-1 Compounds of interest: Glycine, ibuprofen, acetaminophen, deferasirox.

### 4.3.1 Drug loading and method feasibility

Our design aims to minimize the existence of surface crystals and ensure the uniformity of nanocrystals distributed inside the porous matrix. In order to achieve these two goals, several experimental parameters are carefully controlled. First, the dispersed droplets should be as small as possible, so it would be easy for droplets to infiltrate into the matrix with no significant liquid volume left on the surface.

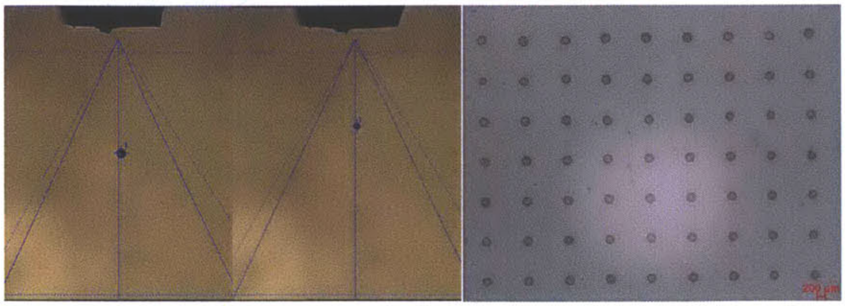

Figure 4-2a and Figure 4-2b show droplets dispersed from Nano Plotter using three different solvents. The volume of droplets are ~ 77-181 pl (corresponding diameter ~ 43-56 μm, which is the same order of magnitude as the membrane thickness, cellulose 75 μm and cellulose acetate 140 μm). Second, the step size of dispersion should be far enough to ensure least interference of two adjacent droplets and yet close enough to achieve a relatively high drug loading if required by formulation needs. Figure 4-2c shows droplets of ethanol dispersed onto a glass slide surface, showing good uniformity of dispersion. By adjusting the equipment parameters, droplet volume and step size could be controlled for different solutions. For example, we made a solution of 4 g ibuprofen and 10 ml ethanol. A single droplet size was tuned to ~ 56 μm by diameter and the step size was set to 50 μm. A cellulose membrane (pore size 200 nm) was cut into a square shape with each side being 30 mm in length and secured onto the Nano Plotter sample plate. After the dispersion was finished, we waited at least 12 hours for crystallization. The sample was also put into a vacuum oven overnight to evaporate all residual solvents, but no significant loss of mass was observed.

(a)

(c)

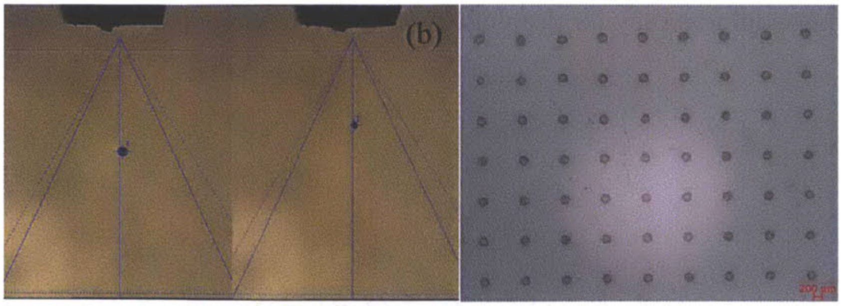

Figure 4-2 Inspection of droplets generated from Nano Plotter. (a) Pure DMSO droplets generated by Nano Plotter. (b) Ibuprofen/ethanol droplets generated by Nano Plotter. The solvent was ibuprofen/ethanol solution and the droplet size is 181 pl. The diameter of the droplet is 57 µm. (c) Array of glycine crystals (result of dispersing glycine/water solution droplets onto a glass slide). The inspection demonstrated that the droplets are very uniform in size and the dispersion process is also quite stable.

After crystallization, we first checked the membrane for surface crystals and recorded the mass increase due to API loading. Using a microscope (objective lens 100X & eyepiece lens 10X), no surface crystals were observed. This is likely a result of the membranes exhibiting good affinity towards water and ethanol; therefore the solution diffused into the matrices very quickly and left little residue on the surface. Table 4-1 summarizes the loading results. They match well with the designed loading amounts, demonstrating that almost all droplets were successfully loaded and embedded into the polymer matrix.

Table 4-1 Loading weighs of different compounds inside the membranes (unit: mg/cm$^2$).

| ***API*** | GLY | IBP | APAP | DFX |
|---|---|---|---|---|
| ***Actual loading mass*** | 9.8 ± 0.4 | 23.1 ± 0.6 | 8.4 ± 0.3 | 5.8 ± 0.4 |

### 4.3.2 Size analysis of nano-crystals inside pores

Preparing nanocrystals as small as possible is one goal of this work. A high concentration of ibuprofen/ethanol solution (0.3 g/ml) and the cellulose membrane with the smallest pore size (200 nm) were used for this study. Characterizing nanocrystals inside the polymer matrix is challenging. Generally speaking, organic compounds have a low melting point and can "charge up" (accumulating electrons) under SEM. As previously mentioned, we used cryo-cutting to prepare cross-sectioned parts of samples. Figure 4-3 shows SEM images of a cross-sectioned part of a membrane loaded with ibuprofen nanocrystals. The membrane was heavily loaded (23.0 wt. %). Figure 3a clearly shows the cross-linked structure of cellulose fibers. Figure 3c is an enlarged image of a small part of Figure 3b. However, due to the high energy nature of SEM focus spot, these organic nanocrystals melted too quickly when we went for even higher magnifications. As shown in the figures, the nanocrystals are attached to the fibers. The smallest ones that can be distinguished are measured ~ 100 nm. We also examined the distribution uniformity of nanocrystals in the membrane, and did not find observable difference between regions in the middle and regions near the surface. X-ray diffraction (peak width) could be utilized as a method to estimate the size of the formed nanocrystals. However, it can only be used to provide a rough estimate[18-20] because many other factors such as crystal defects and structure deformation (micro strain) may also contribute to the peak broadening, and preferred orientation effect will also change the peak height and alter the peak shape.

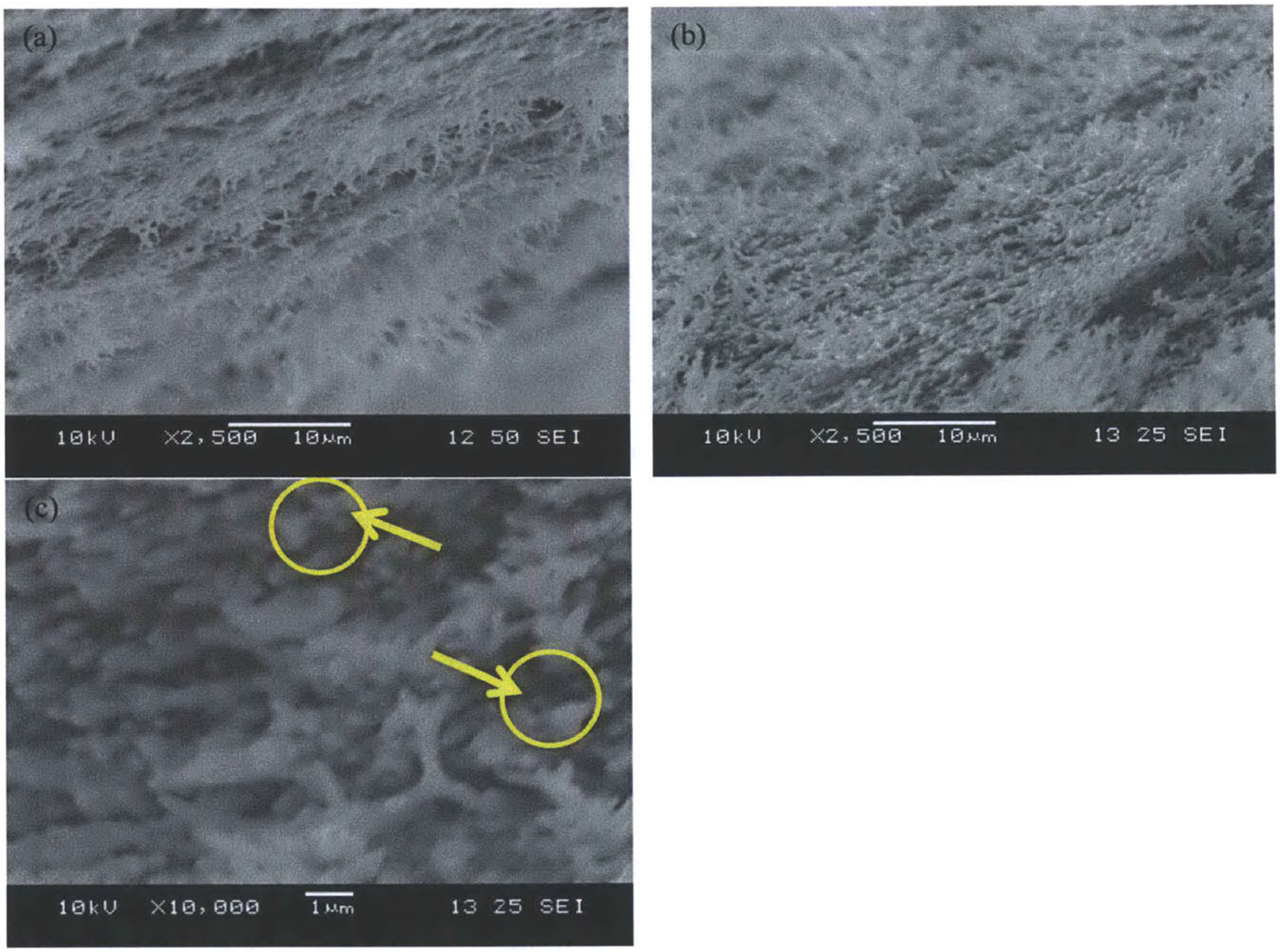

Figure 4-3 SEM images of a cross-sectioned part of a cellulose membrane (200 nm pores, a), a cross-sectioned ibuprofen nanocrystals loaded in a cellulose membrane (200 nm pores, b) (b) A different section with scale bar of 10 µm; and a zoomed image of (b) with a scale bar of 1 µm (c). The loading fraction is 23.0 wt. %. The membrane consists of cross-linked cellulose polymer fibers, and in between the very small white dots are ibuprofen nanocrystals scattered as small as ~ 100 nm (as pointed out in yellow circles).

### 4.3.3 Effect of pore size

The size of confinement plays a significant role in nucleation kinetics and influences the polymorphic outcomes. Previous literature mostly focuses on small confinements from < 1 nm to

~ 50 nm, and result in amorphous materials if supersaturation generation is not controlled well.[18-20, 24, 32-34] In this work we tried several polymer matrices with pore sizes 10-40 nm however, using ibuprofen, these pore sizes produced amorphous material even using very slow evaporation over a period of one week. Table 4-2 and

Table 4-3 summarize the polymorphic outcomes of various crystals in membranes that have pore sizes ≥ 200 nm. The GLY experiments were performed with a relative humidity control (75%RH). Other experiments did not have controlled evaporation rates. As pore size decreased, GLY crystallized as the β-form and APAP partially produced the metastable form II. Using MAS NMR it was confirmed that no detectable amorphous materials existed.

Table 4-2 Polymorphic outcome of compounds crystallized in cellulose membranes of different pore sizes.

| | **GLY** | **IBP** | **ATP** | **DFX** |
|---|---|---|---|---|
| **200 nm pore** | β | I | I,II | I |
| **450 nm pore** | α,β | I | I | I |
| **1 μm pore** | α,β | I | I | I |

Table 4-3 Polymorphic outcome of compounds crystallized in cellulose acetate membranes of different pore sizes.

| | **GLY** | **IBP** | **ATP** | **DFX** |
|---|---|---|---|---|
| **200 nm pore** | β | I | I,II | I |
| **450 nm pore** | α,β | I | I | I |
| **800 nm pore** | α,β | I | I | I |
| **1.2 μm pore** | α | I | I | I |

We considered using XRPD to quantify the fraction of different polymorphs in the samples, but the preferred orientation and interference of cellulose/cellulose acetate background made this impossible. The preferred orientation effect from the (100) plane is prominent in the GLY XRPD, as shown in Figure 4-4. This is probably due to the carboxyl group (–COOH) of glycine molecules forming hydrogen bonds with the hydroxyl groups (–OH) of cellulose and therefore glycine mainly crystallized along the (100) plane, as shown in Figure 4-5.

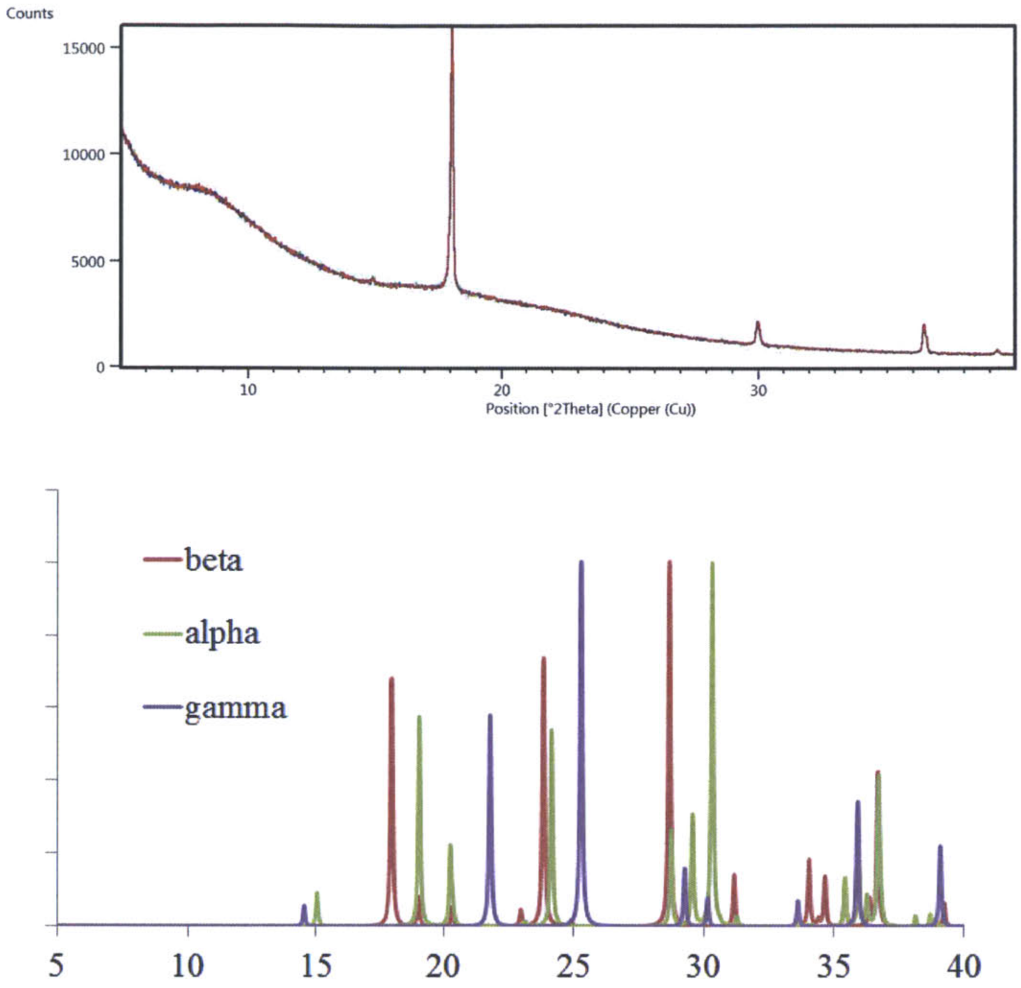

Figure 4-4 XRPD pattern of β-glycine in a cellulose membrane of 200 nm pore size (a) and calculated patterns of different polymorphs of glycine (b). The very intense peak ($2\theta \approx 18^{\circ}$) in (a) corresponding to the (100) plane of β-glycine.

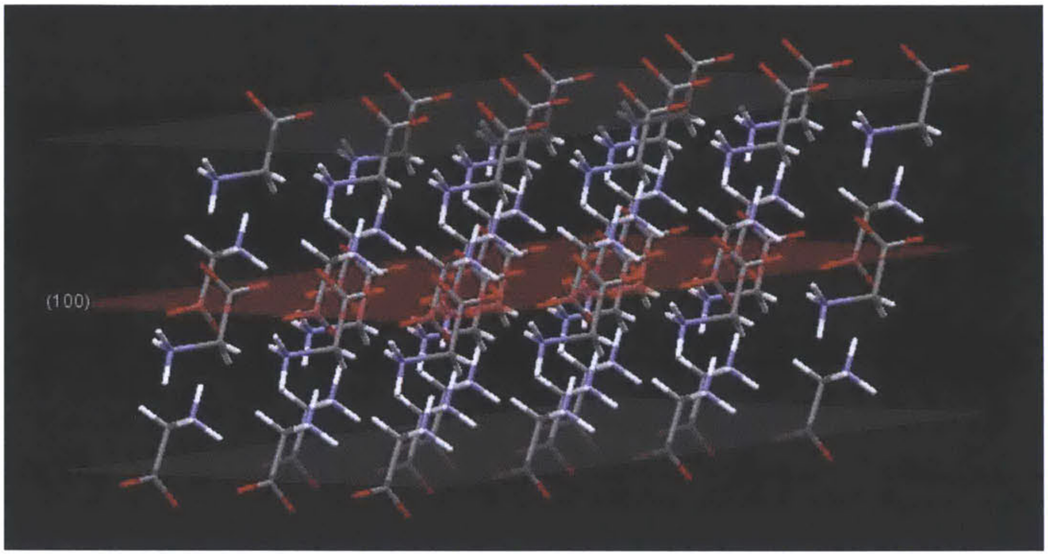

Figure 4-5 Crystal structure of β-glycine on the surface of cellulose fibers, The carboxyl group of the glycine molecules may form hydrogen bonds or interact strongly with the hydroxyl groups of the cellulose membrane and cause the preferred orientation to be the (100) plane.

### 4.3.4 Melting point depression

The Gibbs-Thomas equation (Equation 4-1) is widely used to explain the melting point reduction as a function of particle size. As the particle size reduces, the melting point of the particle also decreases. $T(d)$ is the melting temperature of size d, $T_{bulk}$ is the melting point of bulk crystal, $\sigma_{sl}$ is the crystal-melt interfacial energy, $H_f$ is the crystal molar heat of fusion, $\rho_s$ is crystal density:

$$T(d) = T_{bulk}\left(1 - \frac{4\sigma_{sl}}{H_f \rho_s d}\right) \qquad \text{Equation 4-1}$$

Table 4-4 shows the DSC results of ibuprofen nanocrystallized in various membranes. Each data point was averaged from at least three different samples. By assuming the size of the nanocrystals to be the same as the pore sizes, we found there is a linear relationship between the melting point and the crystal size, although the errors bars are significant compared to the effect.

Table 4-4 Melting points of ibuprofen in different membranes (bulk ibuprofen 75.1 ± 0.1 °C)

| **Cellulose** | **Melting point (°C)** | **Cellulose acetate** | **Melting point (°C)** |
|---|---|---|---|
| **200 nm pore** | 74.0 ± 0.3 | **200 nm pore** | 73.2 ± 0.1 |
| **450 nm pore** | 74.5 ± 0.2 | **450 nm pore** | 74.3 ± 0.2 |
| **1 μm pore** | 74.8 ± 0.2 | **800 nm pore** | 74.6 ± 0.2 |
| | | **1.2 μm pore** | 75.0 ± 0.1 |

We also noticed that different polymer matrices also contributed to different melting point depressions. For the same pore size, the melting point of IBP crystallized in cellulose acetate was depressed by 0.8 °C relative to those in cellulose, as shown in Figure 4-6. This is probably explained by the interactions of IBP molecule with the surface chemistry. Cellulose has –OH group which may interact with –COOH group of ibuprofen. This preferred interaction may promote nucleation kinetics, and therefore crystals will grow quickly and bigger than the crystals in cellulose acetate membranes.

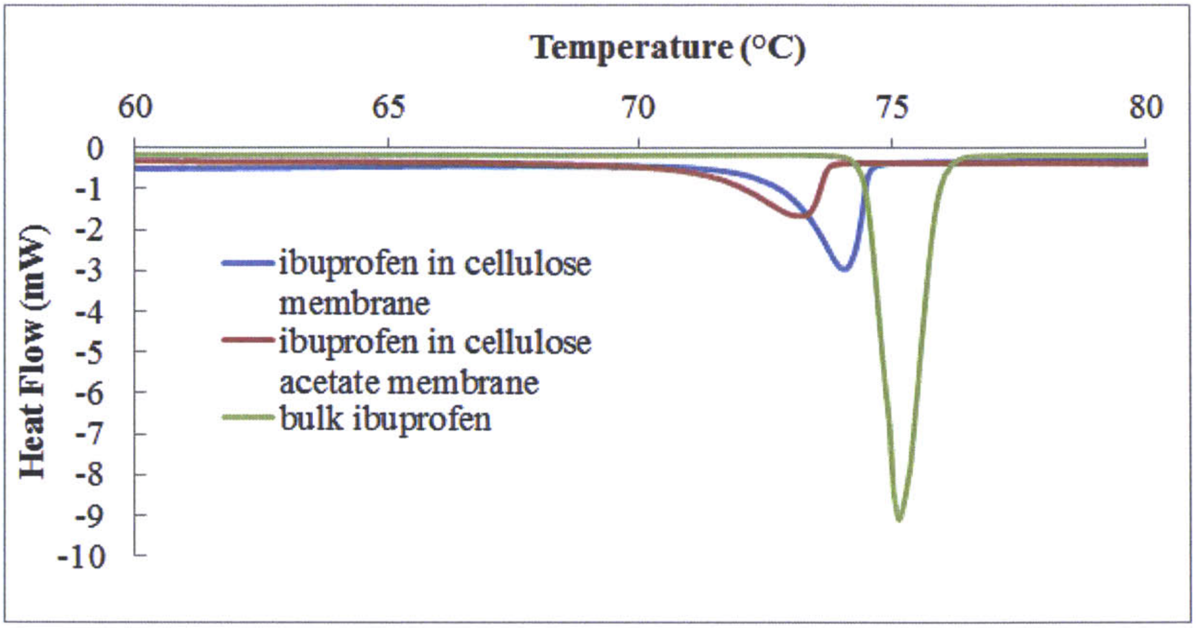

Figure 4-6 Illustration of DSC analysis of three samples: ibuprofen nanocrystals loaded in cellulose membrane of 200 nm pores (blue, 73.2 ± 0.1 ºC), ibuprofen nanocrystals loaded in cellulose acetate membrane of 200 nm pores (red, 74.0 ± 0.3 ºC) and bulk ibuprofen crystals directly from a commercial source (green, 75.1 ± 0.1 ºC).

### 4.3.5 Structure information analyzed by ssNMR

Firstly, we compared the assigned CPMAS NMR spectra of form I crystalline IBP, the stable polymorph as obtained from Sigma Aldrich, and of cellulose-ibuprofen as shown in Figure 4-7. The form I IBP exhibits sharp resonances with linewidth (full-width at half maximum) of approximately 54 Hz, or 0.4 ppm, which is consistent with literature.[35, 36] Upon incorporation of IBP into the cellulose membrane (pore size of 200 nm), we found that the resonances of cellulose-ibuprofen share the same chemical shifts and the same linewidths as the form I IBP. This finding therefore suggests that IBP exists entirely as form I within the pores of the cellulose membrane, and no additional polymorph was formed. A comparison of $^1$H spin-lattice relaxation time constants ($T_1$) of form I and cellulose-ibuprofen only revealed slight differences (Table 4-5), which is further evidence that the cellulose excipient seemingly does not perturb the structure and the dynamics of IBP.

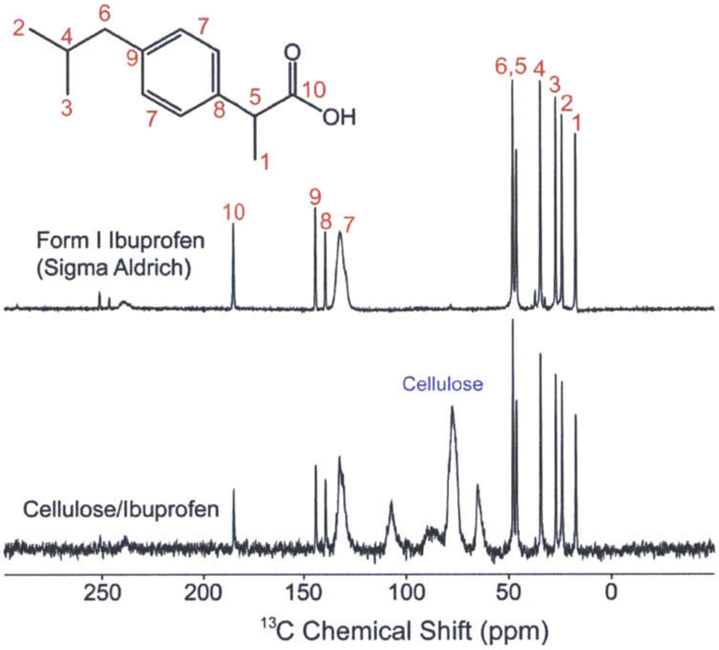

Figure 4-7 $^{13}$C CP MAS NMR spectra of form I ibuprofen (top) and cellulose-ibuprofen (bottom) taken at 11.7 T (500 MHz, $^{1}$H). The cellulose resonance is located between the ibuprofen aliphatic and aromatic carbon resonances, and no spectral overlap occurs.

Table 4-5 $T_1$ ($^1H$) of form I ibuprofen and cellulose-ibuprofen.

| **Chemical Shift (δ, ppm)** | **$T_1$ ($^1H$) (s)**<br>**Form I ibuprofen** | **$T_1$ ($^1H$) (s)**<br>**Cellulose-Ibuprofen** |
|---|---|---|
| **185.0** | 1.18 ± 0.08 | 1.14 ± 0.11 |
| **144.1** | 1.21 ± 0.05 | 1.15 ± 0.09 |
| **139.3** | 1.19 ± 0.06 | 1.08 ± 0.10 |
| **47.9** | 1.22 ± 0.02 | 1.25 ± 0.05 |
| **46.1** | 1.21 ± 0.03 | 1.27 ± 0.04 |
| **34.4** | 1.17 ± 0.03 | 1.19 ± 0.06 |
| **27.0** | 1.13 ± 0.05 | 0.87 ± 0.06 |
| **24.0** | 1.10 ± 0.06 | 0.81 ± 0.05 |
| **17.3** | 1.11 ± 0.06 | 0.83 ± 0.06 |

In contrast with IBP, APAP polymorphism was readily observed within the cellulose membrane. Compared to the $^{13}C$ CP MAS NMR spectrum of the stable monoclinic form I APAP, the spectrum for the cellulose-acetaminophen shows resonance peak splitting that indicates a mixture of polymorphs was formed inside the membrane pores, as shown in Figure 4-8. The difference in isotropic chemical shifts between the polymorphs is not large, but distinct peaks are clearly resolvable for some resonances as shown in Figure 4-9. The isotropic chemical shifts of these additional peaks are consistent with the data published by Moynihan and O'Hare[37] for the orthorhombic form II acetaminophen. The ratio of form I and the form II acetaminophen within the cellulose membrane is 65:35.

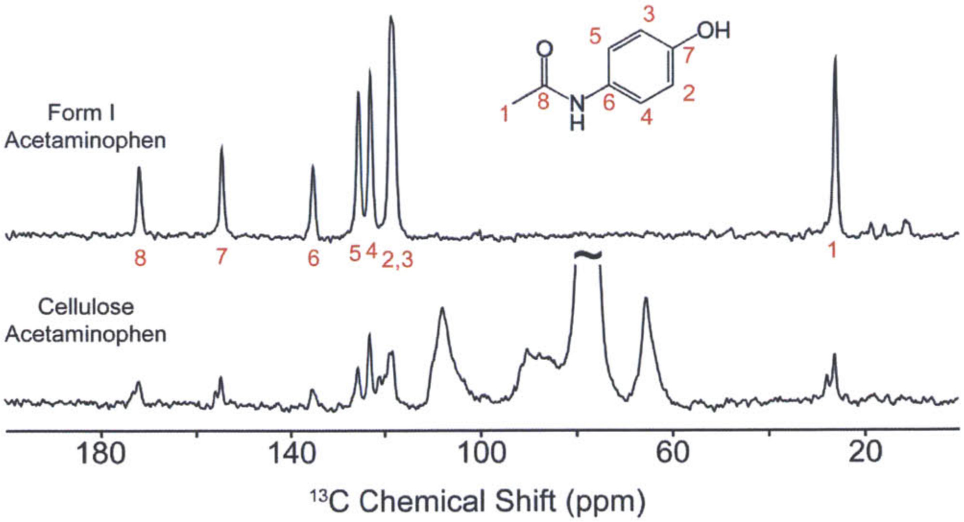

Figure 4-8 $^{13}$C CP MAS NMR spectra of form I acetaminophen (top) and cellulose-acetaminophen (bottom).

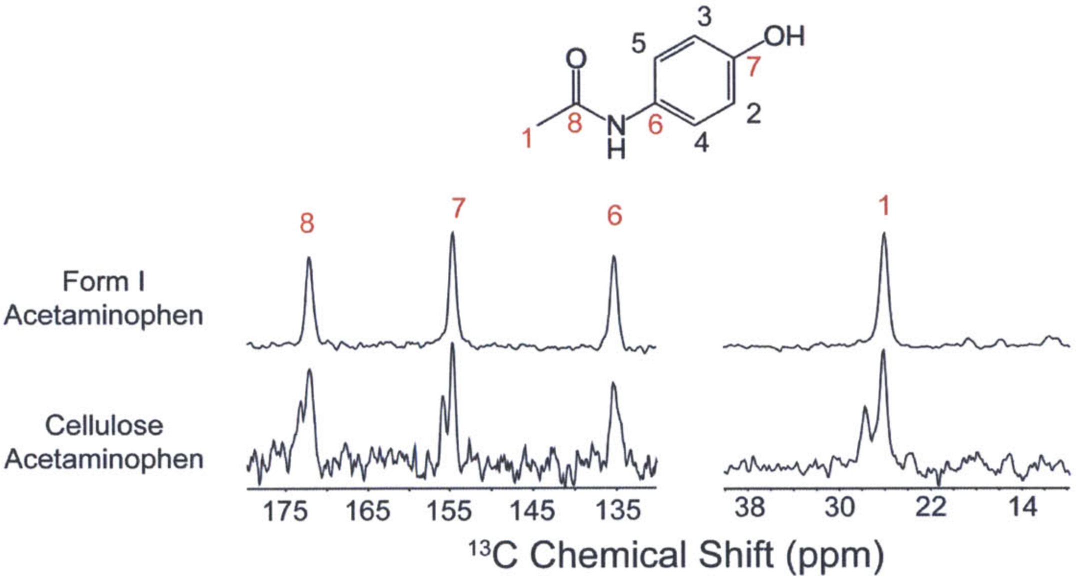

Figure 4-9 Expanded $^{13}$C CP MAS NMR spectra of acetaminophen focusing on resonances sensitive to polymorphism to clearly illustrate the onset of form II observed in the cellulose-acetaminophen formulation.

In addition to the onset of polymorphs, a notable difference between form I acetaminophen and the cellulose-acetaminophen is the measured $^1$H T$_1$. The crystalline form I acetaminophen has $^1$H T$_1$ that is longer than 100 s, but once inside the membrane acetaminophen T$_1$ reduces to less than 20 s, as summarized in Table 4-6. This finding is evidence that no bulk microcrystalline acetaminophen was formed on the membrane surface. Possible factors such as material disorder and crystal defects can also serve as relaxation sinks that reduce acetaminophen T$_1$ within the membrane.

Table 4-6. T$_1$ ($^1$H) of form I acetaminophen and cellulose-acetaminophen.

| **Chemical Shift (δ, ppm)** | **T$_1$ ($^1$H) (s) Form I acetaminophen** | **T$_1$ ($^1$H) (s) Cellulose-Acetaminophen** |
|---|---|---|
| **171.8** | 127.1 ± 15.1 | 18.5 ± 1.3 |
| **154.3** | 122.4 ± 13.2 | 19.0 ± 1.0 |
| **135.0** | 128.8 ± 14.9 | 17.3 ± 1.7 |
| **125.3** | 116.0 ± 12.6 | 16.6 ± 1.2 |
| **122.6** | 109.4 ± 10.6 | 18.7 ± 1.9 |
| **118.3** | 110.5 ± 13.6 | 17.3 ± 1.0 |
| **117.7** | 104.5 ± 9.4 | 19.9 ± 1.0 |
| **25.7** | 126.2 ± 15.9 | 17.8 ± 0.7 |

### 4.3.6 Dissolution enhancement

In order to compare dissolution profiles of nanocrystals in membranes of different pore sizes, we chose IBP as the model compound since it shows consistently the form I polymorph without detectable structure deformation in all the analysis shown above. The same amounts of IBP (20.8±0.6 mg) were successfully loaded into the cellulose membranes of 200 nm, 450 nm, 1 μm pores. For comparison, we also chose a control group which is a mixture of ibuprofen crystals from a commercial source (Sigma Aldrich) and membranes of 200 nm pores. The dissolution tests were conducted under the instruction of U.S. Pharmacopeia standards. Figure 4-10 illustrates the enhanced dissolution profiles of nanocrystals inside membranes. As shown in the figure, membranes of 200 nm pores showed the fastest release, and released twice as much IBP as the control group in one minute. The control group reached 80% release within 15 minutes. But it only took ~ 5, 7 and 12 minutes for membranes of 200 nm, 450 nm, 1 μm pores to achieve 80% release respectively. The improvement of dissolution profiles is probably a combination effect of increasing the surface/volume ratio and improving solubility due to the reduction of crystal size as discussed in the introduction. However, there is a possibility that diffusion of the compound out of the polymer matrix into the bulk dissolution medium may play a role in limiting the whole release process, although we already chose a relatively thin membrane (75 μm). From the perspective of polymer compositions, several alternatives may be possible: (a) rather than cellulose, we may use or design some polymers as the base of the matrix; these polymers can dissolve quickly in water, but are insoluble to some organic solvents which can dissolve the desired loading compounds; (b) some disintegrants may be blended into the matrix during the manufacturing process, so it will be disintegrated into small pieces when in contact with water.

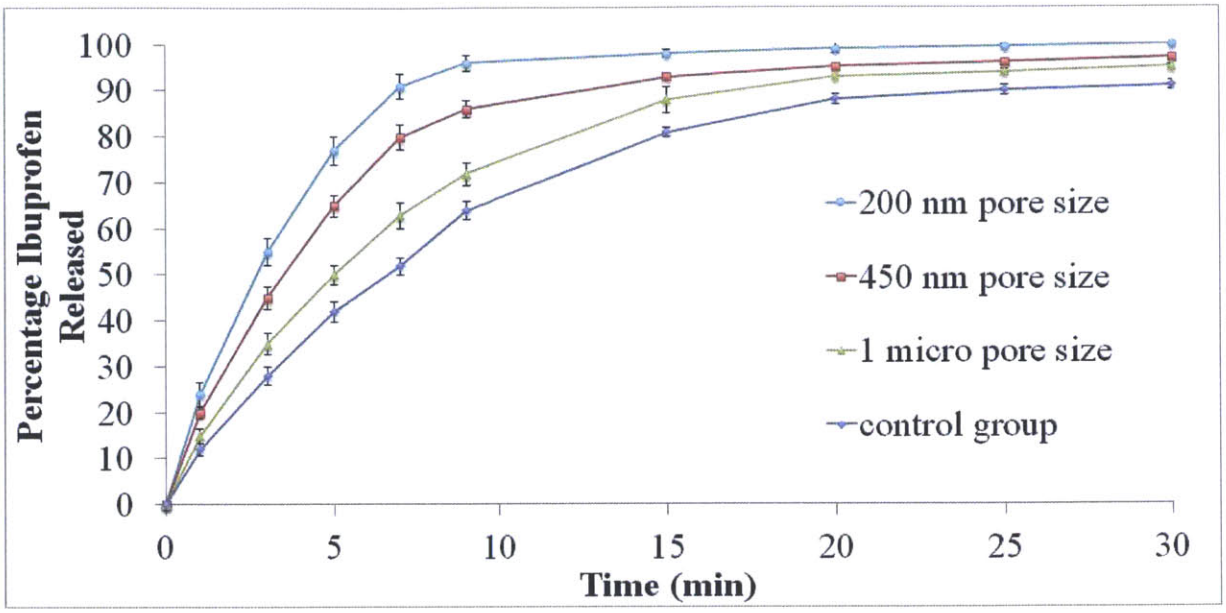

Figure 4-10 Dissolution test of cellulose membranes of different pore sizes loaded with the same weight of ibuprofen nanocrystals. The control group is ibuprofen crystals from commercial bottles (with a mean size of 48 μm) mixed with cellulose membranes of 200 nm pores. Each curve is averaged from at least three dissolution tests. Lines are placed as guides for the reader.

## 4.4 Conclusion

In conclusion, we demonstrated that the impregnation method using polymer matrices is a promising mean to produce nano-sized organic molecular crystals with controlled polymorphs. This method provides several benefits. (1) The nanocrystals are directly embedded in the excipients, thereby avoiding transport problems of fine particles and non-uniformity of active pharmaceutical ingredients in excipients. (2) Crystal size and polymorphic outcome can be controlled by the pore size and surface chemistry of the polymer matrix. (3) Polymer matrices may help block environmental humidity, separate nanocrystals in distances and confine them in certain dimensions to stabilize nanocrystals. (4) Furthermore, the soft confinement (polymer matrices) may be a certain type of polymer or by addition of disintergrants that allow the matrices to immediately dissolve when coming into contact with water or from pH changes. In this scenario, API nanocrystals would be released even faster. Our results help advance the fundamental understanding towards nucleation mechanism and kinetics of organic molecules in confined environments. This work has immense potential for industrial applications, and is still on-going in our group for process development. However, more detailed cost analysis and equipment/process design would be necessary for industrial scale production.

## 4.5 Reference

1. E. M. Merisko-Liversidge and G. G. Liversidge, *Toxicologic pathology*, 2008, **36**, 43.
2. L. A. Wegiel, L. J. Mauer, K. J. Edgar and L. S. Taylor, *Journal of pharmaceutical sciences*, 2013, **102**, 171.
3. K. Kim, A. Centrone, T. A. Hatton and A. S. Myerson, *Crystengcomm*, 2011, **13**, 1127.
4. P. G. Vekilov and M. A. Vorontsova, *Acta Crystallographica Section F*, 2014, **70**, 271.
5. P. G. Vekilov, *Cryst Growth Des*, 2010, **10**, 5007.
6. W. Oswald, *Z. Phys. Chem*, 1900, **34**, 495.
7. K. Kim, I. S. Lee, A. Centrone, T. A. Hatton and A. S. Myerson, *Journal of the American Chemical Society*, 2009, **131**, 18212.
8. M. Wang, G. C. Rutledge, A. S. Myerson and B. L. Trout, *Journal of pharmaceutical sciences*, 2012, **101**, 1178.
9. E. Kwon, H. Oikawa, H. Kasai and H. Nakanishi, *Crystal Growth & Design*, 2007, **7**, 600.
10. S. Petersen and J. Ulrich, *Chem Eng Technol*, 2013, **36**, 398.
11. M. Turk and R. Lietzow, *Journal of Supercritical Fluids*, 2008, **45**, 346.
12. E. Reverchon, G. D. Porta and M. G. Falivene, *Journal of Supercritical Fluids*, 2000, **17**, 239.
13. S. W. Siddiqui, Y. Zhao, A. Kukukova and S. M. Kresta, *Ind. Eng. Chem. Res.*, 2009, **48**, 7945.
14. H. Chioua, H. K. Chana, D. Henga, R. K. Prudhommeb and J. A. Raperc, *Journal of Aerosol Science*, 2008, **39**, 500.
15. M. Sultana, *Thesis: Microfluidic Systems for Continuous Crystallization of small organic molecules*, Masschusetts Institute of Technology, Cambridge, 2010.
16. V. Genota, S. Desportesb, C. Croushorea, J. Lefevrea, R. B. Pansua, J. A. Delairea and P. R. Rohrb, *Chemical Engineering Journal*, 2010, **161**, 234.
17. M. Ildefonso, N. Candoni and S. Veesler, *Crystal Growth & Design*, 2013, **13**, 2107.
18. B. D. Hamilton, M. A. Hillmyer and M. D. Ward, *Crystal Growth & Design*, 2008, **8**, 3368.
19. J.-M. Ha, M. A. Hillmyer and M. D. Ward, *The Journal of Physical Chemistry B*, 2005, **109**, 1392.
20. J.-M. Ha, B. D. Hamilton, M. A. Hillmyer and M. D. Ward, *Crystal Growth & Design*, 2012, **12**, 4494.
21. K. K. Qian and R. H. Bogner, *Journal of pharmaceutical sciences*, 2012, **101**, 444.
22. P. Maheshwari, D. Dutta, S. K. Sharma, K. Sudarshan, P. K. Pujari, M. Majumder, B. Pahari, B. Bandyopadhyay, K. Ghoshray and A. Ghoshray, *The Journal of Physical Chemistry C*, 2010, **114**, 4966.
23. Y. Diao, M. E. Helgeson, A. S. Myerson, T. A. Hatton, P. S. Doyle and B. L. Trout, *Journal of the American Chemical Society*, 2011, **133**, 3756.
24. Y. Diao, M. E. Helgeson, Z. A. Siam, P. S. Doyle, A. S. Myerson, T. A. Hatton and B. L. Trout, *Crystal Growth & Design*, 2011, **12**, 508.
25. V. López-Mejías, A. S. Myerson and B. L. Trout, *Crystal Growth & Design*, 2013, **13**, 3835.

26. A. Pines, J. S. Waugh and M. G. Gibby, *J Chem Phys*, 1972, **56**, 1776.
27. R. L. Vold, J. S. Waugh, M. P. Klein and D. E. Phelps, *J Chem Phys*, 1968, **48**, 3831.
28. R. Freeman and H. D. W. Hill, *J Chem Phys*, 1971, **54**, 3367.
29. A. E. Bennett, C. M. Rienstra, M. Auger, K. V. Lakshmi and R. G. Griffin, *J Chem Phys*, 1995, **103**, 6951.
30. T. J. Offerdahl, J. S. Salsbury, Z. D. Dong, D. J. W. Grant, S. A. Schroeder, I. Prakash, E. M. Gorman, D. H. Barich and E. J. Munson, *J Pharm Sci-Us*, 2005, **94**, 2591.
31. P. Derollez, E. Dudognon, F. Affouard, F. Danede, N. T. Correia and M. Descamps, *Acta Crystallographica Section B*, 2010, **66**, 76.
32. J. M. Ha, J. H. Wolf, M. A. Hillmyer and M. D. Ward, *J. Am. Chem. Soc.*, 2004, **126**, 3382.
33. Y. Diao, M. E. Helgeson, A. S. Myerson, T. A. Hatton, P. S. Doyle and B. L. Trout, *J. Am. Chem. Soc.*, 2011, **133**, 3756.
34. Y. Diao, T. Harada, A. S. Myerson, T. A. Hatton and B. L. Trout, *Nat. Mater.*, 2011, **10**, 867.
35. M. Geppi, S. Guccione, G. Mollica, R. Pignatello and C. A. Veracini, *Pharm Res*, 2005, **22**, 1544.
36. J. P. Bradley, The University of Warwick, 2011.
37. H. A. Moynihan and I. P. O'Hare, *International Journal of Pharmaceutics*, 2002, **247**, 179.

## 4.6 Appendix

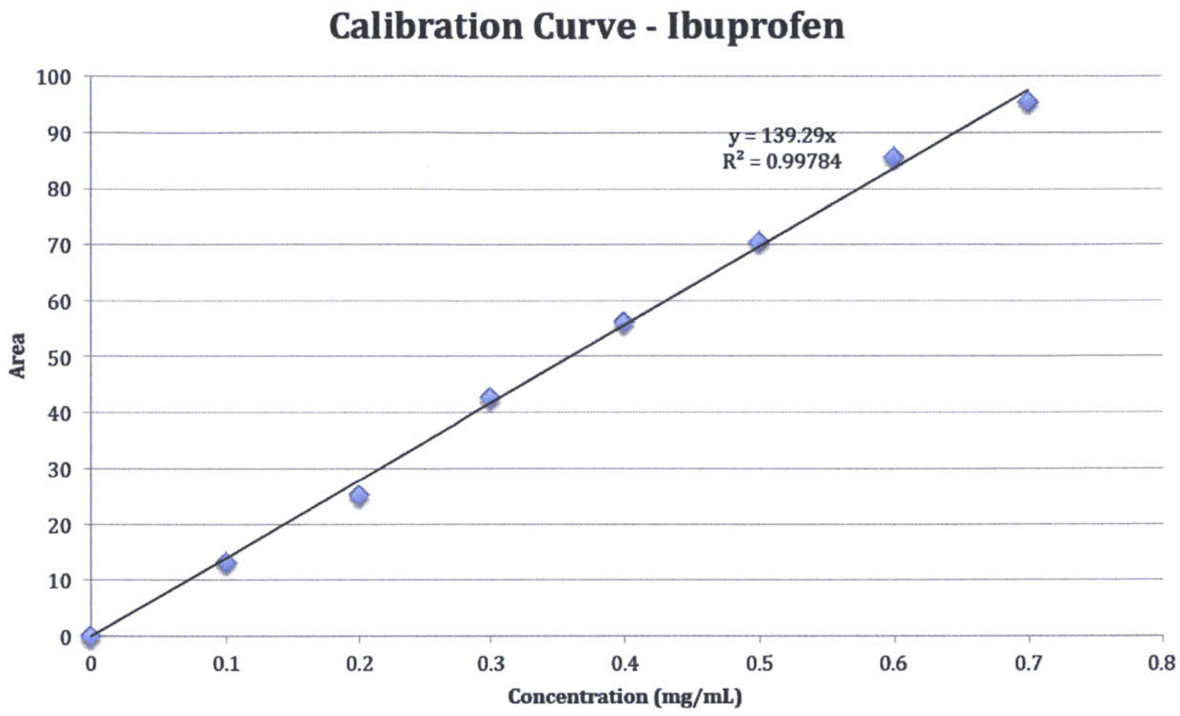

Figure 4-11 Ibuprofen calibration curve using HPLC

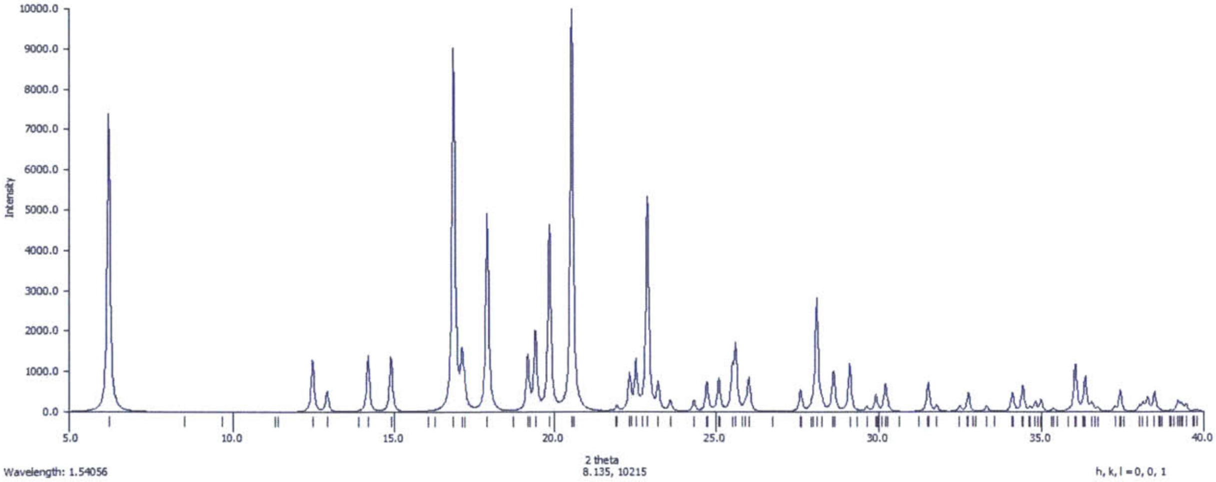

Figure 4-12 Polymorph I of ibuprofen

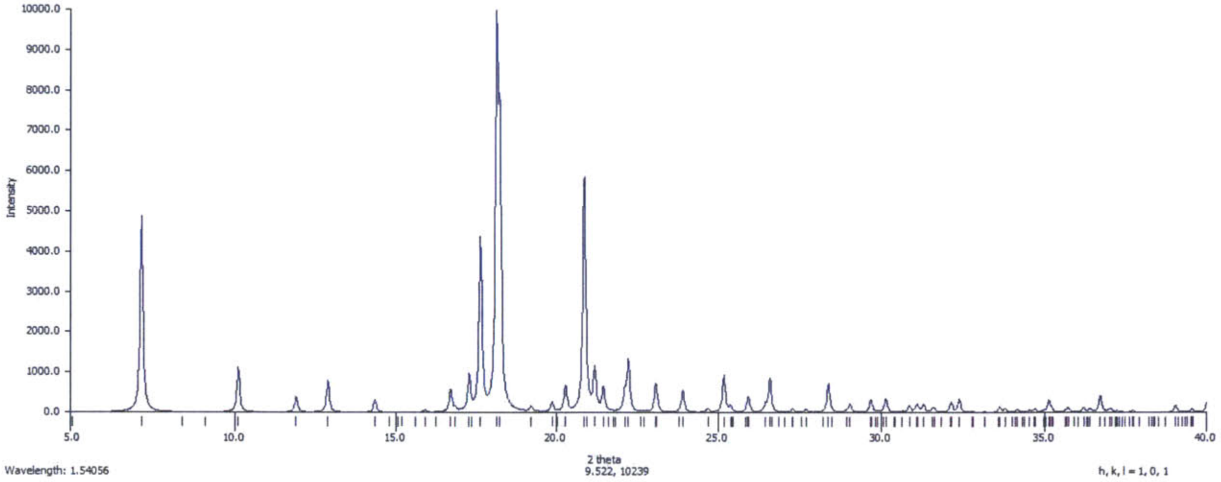

Figure 4-13 Polymorph II of ibuprofen

# 5 FORMATION OF ORGANIC MOLECULAR NANOCRYSTALS UNDER RIGID CONFINEMENT

Nanocrystallization in rigid confinement has been previously reported, however, the role of pore size, supersaturation generation and their influence on crystal formation and polymorphism are not well understood. Here we present a systematic study of the nucleation of organic molecular nanocrystals in rigid pores. Four different compounds were studied, ibuprofen, fenofibrate, griseofulvin and indomethacin, which range from simple to complex. Solid-state Nuclear Magnetic Resonance (NMR) was employed to analyze the structure of those compounds inside pores which are difficult to characterize by other analytical methods. We successfully demonstrated the production of nano-crystalline ibuprofen, fenofibrate and griseofulvin in porous silica particles with 40 nm pores. These nanocrystals showed significant enhancement in dissolution rates. These results help advance the fundamental understanding of nucleation under rigid confinement and may lead to potential applications in developing new formulations in the pharmaceutical industry.

## 5.1 Introduction

The formation of organic molecular nanocrystals is a topic of great interest in the pharmaceutical industry because of the potential increase in solubility and dissolution rate of organic molecular crystals below 1 μm[1-4]. Direct production of nanocrystals through crystallization while controlling the crystal form (polymorph) is a difficult problem and an active area of research[4]. Previously, researchers have explored many novel methods based on the use of spray drying[3], supercritical fluid[5, 6], impinging jetting[7, 8], microfluids[9-11] and nano-porous confinement[12-16]. In particular, nano-crystallization in porous materials is considered a promising and robust mean. These porous materials can be generally divided into two categories, soft confinement (mostly polymer) and rigid confinement (mostly inorganic materials, such as porous silica, alumina and zeolite). Here, we mainly focus on the rigid confinement. Ha et al. examined the polymorphic outcomes of anthranilic acid in 7.5/24/55 nm controlled pore glasses and found out that the metastable polymorph (form II) preferably crystallized in smaller pores and remained stabilized for at least one month.[17] Similar phenomena were also reported on pimelic acid, subric acid and coumarin.[18]

Compounds nanocrystallized inside porous matrices, can be challenging to characterize. Traditional crystallographic techniques such as x-ray powder diffraction (XRPD) rely on diffraction of incident x-ray off the sample surface, which becomes difficult if the nanocrystals are embedded within the pores and are low in concentration. Solid-state NMR (ssNMR), which is not constrained in this way, is therefore a viable method to study nano-crystallization in compatible porous systems.[19] Combined with magic angle spinning (MAS) and cross polarization (CP) at high magnetic field (> 10 T), solid-state NMR offers high resolution for studies of various polymorphs, hydrates, and solvates.[20, 21] NMR parameters such as chemical shift, linewidths, and relaxation are sensitive to polymorphism and crystallinity,[22-26] and in recent years more advanced NMR techniques have been applied for structural and dynamics studies of pharmaceuticals.[27, 28] In one study, Lubach et al. examined by $^{13}$C CPMAS NMR bupivacaine, a local anesthetic, encapsulated in lipospheres in tristearin/protein matrix.[29] In another study, Azaïs et al. investigated ibuprofen embedded in the mesoporous silica particle MCM-41,[30] whereas they characterized the system by a combination of $^{1}H$, $^{13}C$, and $^{29}Si$ MAS NMR and evaluated the impact of temperature (218 – 286 K) and pore diameters (35 and 116 Å). They found that ibuprofen exhibits liquid-like molecular dynamics inside the pores at room temperature, with higher mobility associated with the larger pore size. Recently, dynamic nuclear polarization, which can improve NMR signal-to-noise by factors of $10^{2}$ -$10^{3}$, has been applied to porous materials[31-34] and pharmaceutical samples,[35, 36] so the technique may prove useful for NMR studies of organic molecular nanocrystals embedded in porous matrices.

This work aims to develop a novel method to produce nano-sized organic molecular nanocrystals while controlling the polymorphic outcome under rigid confinement. To this end, four different organic compounds (ibuprofen, fenofibrate, griseofulvin and indomethacin) were selected as model compounds. Experimental conditions such as evaporation rates and loading percentages were tuned to better control the polymorphic outcome and nucleation rate. Information on the crystallinity and crystalline forms obtained are analysed by solid-state NMR. We anticipate that our results will help improve the fundamental understanding of nucleation and polymorphism of nanocrystals under rigid confinement and lead to novel formulation methods in industry.

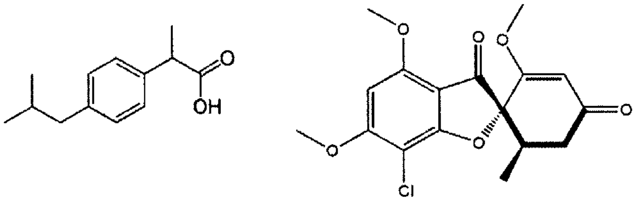

Ibuprofen (IBP) Griseofulvin (GSF)

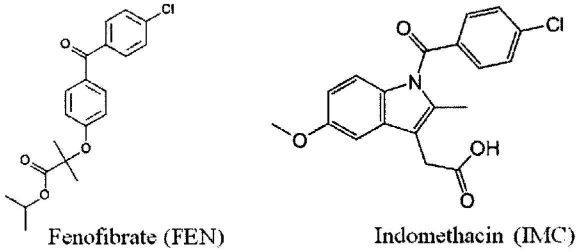

Fenofibrate (FEN) Indomethacin (IMC)

Figure 5-1 Compounds of interest: Ibuprofen, Fenofibrate, Griseofulvin and Indomethacin.

## 5.2 Experimental Section

### 5.2.1 Materials

Ibuprofen, fenofibrate, griseofulvin and indomethacin were obtained from Sigma Aldrich. Silicon dioxide (silica) particles of 40 nm pores (AEROPERL® 300 Pharma) were obtained from Evonik USA. Silicon dioxide particles of 10 nm pores were obtained from EPRUI Nanoparticles & Microspheres Co. Ltd.

### 5.2.2 X-Ray Powder Diffraction (XRPD) Analysis

The instrument (X'Pert PRO, PANalytical Inc.) is equipped with a PW3050/60 standard resolution goniometer and a PW3373/10 Cu LFF DK241245 X-ray tube. The high tension generator high voltage and anode current were set as 45 kV and 40 mA. A spinner sample stage

PW3064 (Reflection mode) was used for all samples. Settings on incident beam path include: soller slit 0.04 rad., mask fixed 10 mm, programmable divergence slit and fixed 1° anti-scatter slit. Settings on diffracted beam path include: soller slit 0.04 rad and programmable anti-scatter slit. The scan was programmed as a continuous scan: 2θ angle 2-40°, step size 0.0083556°, time per step 19.685 s; three repeated scans were collected to average.

### 5.2.3 Differential Scanning Calorimetry (DSC) Analysis

The instrument (Q2000, TA instruments) is connected with a nitrogen gas cylinder to maintain a flow rate of 50 ml/min in order to create an inert gas environment in the sample chamber. An extra refrigerated cooling system (RCS 40, TA instruments) is used to extend the available temperature range to -40 ~ 400 °C. Tzero® pan and lid were used. A heating/cooling rate of 5 °C/min was applied and different initial/final temperatures were set for different compounds.

### 5.2.4 Solid-state Nuclear Magnetic Resonance (ssNMR) Methods

Solid-state NMR experiments were conducted on a home-built 500 MHz spectrometer (courtesy of Dr. Dave Ruben, FBML) using either a 3.2 mm or a 4 mm Varian triple resonance ($^1H/^{13}C/^{15}N$) probe. For the CPMAS experiments,[37] the CP contact time was 2.0 ms at $\nu_{rf}$ of 83 kHz and the MAS frequency was between 10 to 13.5 kHz. The $^1H$ $T_1$ was measured either by the inversion-recovery[38] or the saturation recovery[39] sequence. All experiments utilized the two pulse phase modulation (TPPM)[40] proton decoupling sequence. The recycling time for all samples was 5 s. The number of scans was up to 80,000 depending on the signal to noise. The spectrometer was referenced to adamantane (40.49 ppm) with respect to DSS (0 ppm). Quantification of active pharmaceutical ingredient (API) polymorphs from CPMAS spectra was performed following the procedure published by Offerdahl et al.[22]

### 5.2.5 Dissolution test

Procedures of dissolution tests are from USP standards. Analysis of concentration used either High-Performance Liquid Chromatography (HPLC) or ultraviolet–visible spectroscopy (UV-Vis). Here, we take ibuprofen as an example. The dissolution medium used for ibuprofen was a pH 7.2 phosphate buffer. The phosphate buffer was made using monobasic potassium phosphate, sodium hydroxide, and water. 27.22 grams of potassium phosphate was weighed out and dissolved in 1000 mL of water. 50 mL of the solution was mixed with 34.7 mL of 0.2 M sodium hydroxide solution, and water was added to form 200 mL of the phosphate buffer. The dissolution profile of the sample was determined using the USP Dissolution Apparatus 2 at 37 °C. The apparatus operated under 50 revolutions per minute. 900 mL of the dissolution medium was allowed to reach temperature equilibrium before the sample was placed in the medium. Approximately one milliliter of the mixture was taken out and filtered each time for a concentration test. The percentage of ibuprofen dissolved in the medium was determined using high-performance liquid chromatography (HPLC). The mobile phase for the HPLC was made using chloroacetic acid, acetonitrile, and water. 4.0 g of chloroacetic acid was weighed out and dissolved in 400 g of water. The solution was then mixed with 600 mL of acetonitrile and degassed.

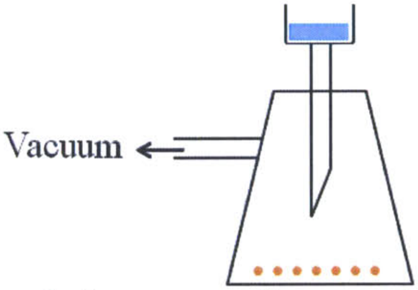

Figure 5-2 A loading procedure under low pressure. Porous particles were placed at the bottom of a Buchner flask connected to a vacuum line, and then API solution was injected from the top.

### 5.2.6 Experimental set-up

Figure 5-2 shows the loading process of solution into porous particles. Undersaturated API solutions were prepared (i.e. 5 g ibuprofen in 10 ml ethanol). A given amount of porous silicon dioxide particles were weighed (i.e., 1 g of silicon dioxide, AEROPERL®, pore size ~40 nm) and put into a 50 ml Buchner flask. A rubber cap was used to seal the Buchner flask. The Buchner flask was then connected to a vacuum line (~ 0.5 atm) in order to prevent possible trapping of air inside pores during the loading process, as shown in figure 2. After 10 minutes, API solution was injected into the Buchner flask through the rubber cap using a syringe and needle. To enhance the mass transfer, the flask was lightly shaken for the silicon dioxide particles to be suspended and then kept still for 60 minutes. Afterwards, a filtration and washing step was applied to remove adhering solution from the surface. The particles were then taken out for crystallization. The experimental parameters tuned include different APIs, porous particles, solution concentrations, pore sizes, vacuum and filtration conditions. In addition, various crystallization methods, such as slow evaporation, slow cooling and anti-solvent methods were applied.[41] Normally the crystallization time was a minimum of 12 hours. Samples were also put into a vacuum oven overnight to evaporate all residual solvents, but no significant loss of mass was observed.

## 5.3 Results and discussion

Ibuprofen (IBP), griseofulvin (GSF), fenofibrate (FEN) and indomethacin (IMC) were selected as model compounds to represent APIs from simple to complex, as shown in Figure 5-1. IBP was reported as two polymorphs (I and II), but the second polymorph was only successfully produced in a very small account (milligrams) with a complicated heating/quenching loop.[42] GSF has three different polymorphs (I/II/III) while form I is the most stable form.[43] FEN possesses two different polymorphs (I/II, stability: form I > form II).[44] IMC was reported to have 8 different polymorphs: the most stable form is $\gamma$-form and the metastable form often produced is $\alpha$-form.[45]

### 5.3.1 XRPD analysis

In preliminary tests we found that we were unable to crystallize IBP in porous silica particles with 10 nm pores and that the release rate from the pores was slow and likely limited by the rate of diffusion . Based on this result we focused our work on porous silica particles with 40 nm pores.

Table 5-1 IBP loaded in porous silica particles of 40 nm pores

| Washing levels | IBP mass loaded | Melting points by DSC | Polymorphic outcome by XRPD | Polymorphic outcome by ssNMR |
|---|---|---|---|---|
| No wash | 28.2 ± 3.1%wt | 65.8 ± 0.2°C /75.1 ± 0.1°C | Form I | - |
| Light wash | 21.7 ± 4.7%wt | 65.6 ± 0.3°C /75.0 ± 0.3°C | Form I | - |
| Medium wash | 12.3 ± 2.1%wt | 65.5 ± 0.3°C | No crystalline peaks | Two forms (79:21) |
| Strong wash | 6.8 ± 3.0%wt | 66.0 ± 0.2°C | No crystalline peaks | - |

Table 5-2 FEN loaded in porous silica particles of 40 nm pores

| Washing levels | FEN mass loaded | Melting points by DSC | Polymorphic outcome by XRPD | Polymorphic outcome by ssNMR |
|---|---|---|---|---|
| Light wash | 15.8 ± 4.4%wt | 71.3 ± 0.3°C /81.0 ± 0.1°C | Form I | - |
| Strong wash | 8.1 ± 3.5%wt | 71.2 ± 0.4°C | No crystalline peaks | - |

Table 5-1 shows results of IBP loaded inside porous silica particles of 40 nm pores with different washing levels. The loading of compounds into the porous particles is significantly impacted by the washing employed. Solution residue is left on the surface of the particles if washing is not sufficient, and bulk surface crystals may form during crystallization. Cold pure solvent (~ 4 °C) was used as the washing solvent after the filtration step. The washing levels were quantified by the volume of cold solvent used. However, it is difficult to ensure that every particle was washed and every sample was washed exactly the same way. Therefore, at least 10 experiments for each data point were conducted. Samples with no wash exhibit an average loading of 28.2 wt%. For these samples, some big surface crystals could be observed under the polarized optical microscope (100X). These surface crystals contribute a major part of signal in the XRPD. The number of X-ray photons into the sample decays exponentially as the depth increases, and therefore the major part of the XRPD pattern represents crystals on the surface and within a few micrometers below the surface.

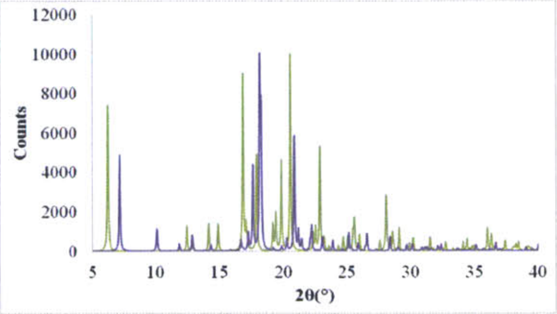

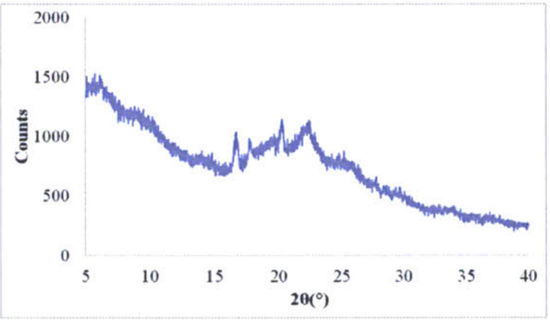

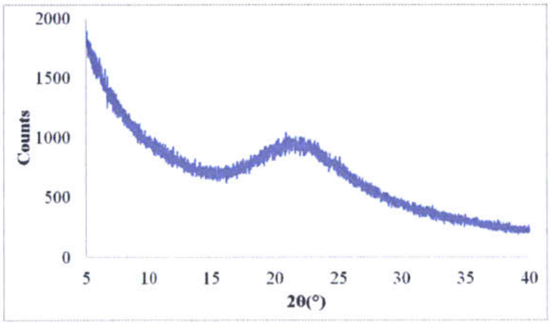

Figure 5-3 shows the XRPD patterns of samples of light wash and medium wash. The pattern of samples of light wash exhibits the characteristic peaks of form I while no peaks are present in the pattern of samples of medium wash. The reason of peak broadening is not due to size reduction of nanocrystals but from non-uniform height differences of silica particles. The results suggest the existence of form I crystals and no crystals on the surface or within a few micrometers below the surface of samples of light- and medium-wash, respectively.

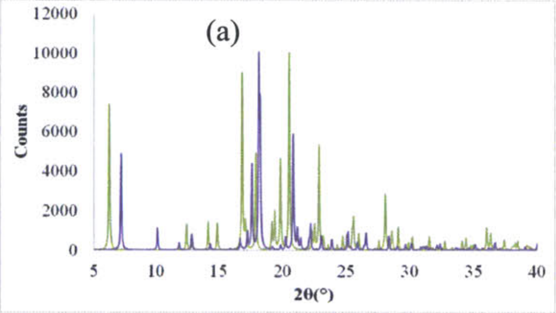

Table 5-3 GSF loaded in porous silica particles of 40 nm pores

| Washing levels | GSF mass loaded | Melting points by DSC | Polymorphic outcome by XRPD | Polymorphic outcome by ssNMR |
|---|---|---|---|---|
| **Light wash** | 17.2 ± 2.5%wt | 215.1 ± 0.3°C /221.3 ± 0.1°C | Form I | Form I/II & amorphous |
| **Strong wash** | 8.3 ± 2.8%wt | 205.3 ± 0.4°C /215.2 ± 0.2°C | No crystalline peaks | Form I/II & amorphous |

Table 5-4 IMC loaded in porous silica particles of 40 nm pores

| Washing levels | IMC mass loaded | Melting points by DSC | Polymorphic outcome by XRPD | Polymorphic outcome by ssNMR |
|---|---|---|---|---|
| **Strong wash** | 9.1 ± 2.7%wt | No peaks | No crystalline peaks | amorphous |

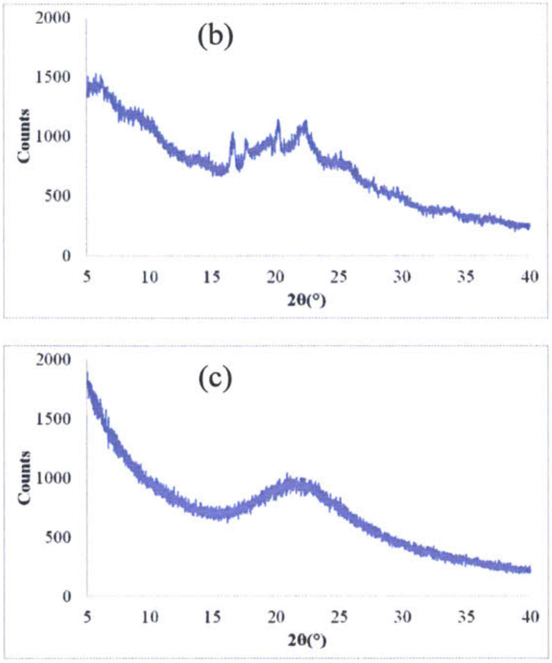

Figure 5-3 XRPD patterns of IBP loaded in porous silica particles of 40 nm pores of light- (b) and medium-wash (c). (a) The reference pattern of IBP form I (green) and II (purple). Characteristic peaks of (b) match well with form I, showing crystals on the surface and within a few micrometers below the surface are form I.

### 5.3.2 DSC analysis

Existence of bulk surface crystals can also be verified by DSC analysis. Melting point depression of compounds nanocrystallized under similar confinement has been previously described in the literature.[13, 18] In our experiments, IBP and FEN in the porous silica particles shows ~ 10 °C decrease compared to the melting points of their bulk crystals (Table 5-2). Surface crystals, without confinement, are bulk crystals with normal melting points. As shown in Figure 5-4, FEN samples of light wash shows the major peak of 71.4 °C as well as a small peak at 81.2 °C, indicating the existence of surface bulk crystals. The results are consistent with the XRPD analysis.

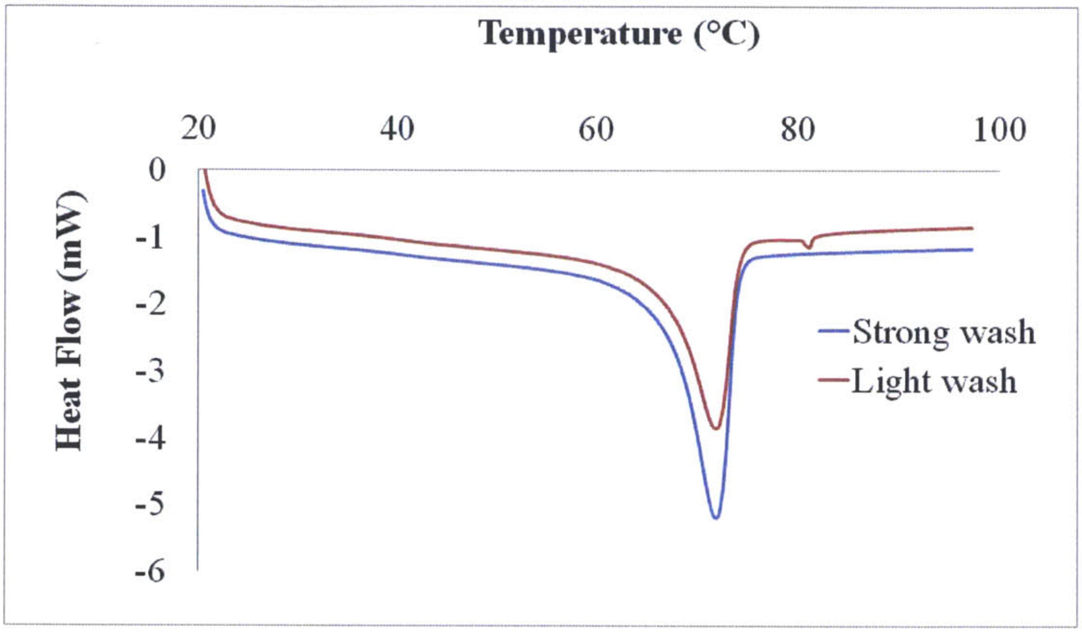

Figure 5-4 DSC results of FEN loaded in porous silica particles of 40 nm pores of light- (red) and strong-wash (blue). Samples of light wash show two peaks (71.4 and 81.2 °C) while samples of strong wash has only one peak of 71.7 °C.

### 5.3.3 Solid state NMR analysis

Another method, solid-state NMR, was applied to further analyze the nanocrystals under the confinement. Here, one IBP sample of medium wash was used for the NMR study. We observed the onset of additional peaks in the aliphatic region of silica-IBP, as shown in Figure 5-5, which suggests IBP polymorphism. The ratio of the two forms is 79:21. The finding of polymorphism is intriguing. Form II of IBP was reported in 2009, but only a small amount was obtained with a very complex heating/quenching method.[42] However, we do not believe the second polymorph observed is form II, as the observed chemical shifts are inconsistent with the NMR spectrum of form II reported in literature.[46] However, no other polymorph of IBP has been reported yet. If it is not form II, it could be a new polymorph of IBP; although our DSC results do not indicate signs of a second polymorph. It may be due to the melting points being close to form I and therefore indistinguishable. An alternative explanation is the silica base interacting with the IBP drug may induce a distinctive $^{13}$C shift; further investigations are currently underway.

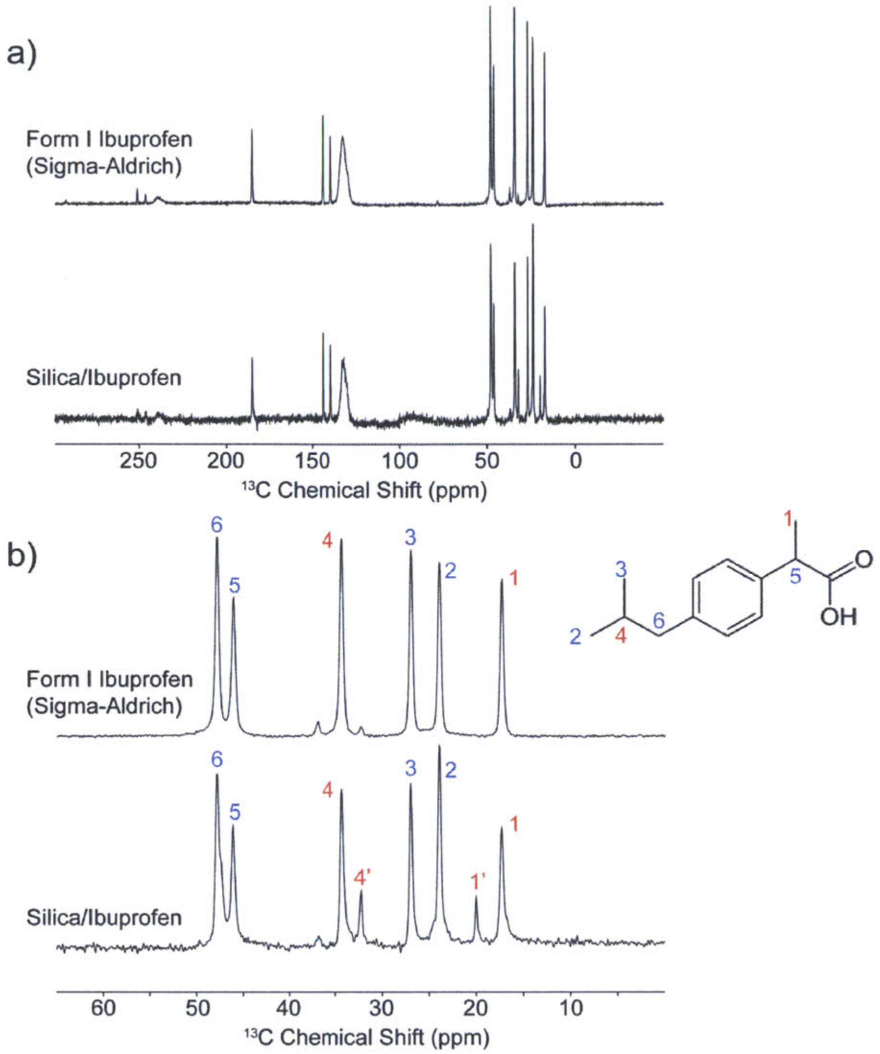

Figure 5-5 $^{13}$C CPMAS spectra of form I IBP and silica-IBP, a) the full spectra and b) the spectra expanded on the aliphatic region, which clearly shows the onset of additional peaks for silica-IBP (peak 1' and 4'). Peak integration utilizing peak 1 and 1', and also 4 and 4', indicates that the ratio of two forms to be 79:21.

A similar combination of polymorphs was also observed in the study of GSF (Table 5-3). In the DSC results of light wash GSF samples, we observed glass transitions and recrystallization processes during heating. These characteristics normally indicate the existence of amorphous content in the sample. We conducted ssNMR on one sample to confirm. The CPMAS $^{13}$C spectrum of silica-GSF (Figure 5-6) shows that the sample is a combination of amorphous content and two distinct crystalline polymorphs. DSC results confirmed the existence of a small amount of surface bulk crystals, and XRPD shows characteristic peaks of the most stable form (form I). Therefore, one of the two polymorphs can be confirmed as form I. We took one strong washed GSF sample to further explore the control of its polymorphic outcome. As shown in the bottom part of Figure 5-6, only one set of polymorph peaks remains along with the amorphous material. (Complete assignment of peaks is presented in appendix using previously published solution NMR spectra[47, 48]) This finding indicates that the polymorph I formed on the silica surface diminished from the stronger wash while the second polymorph formed inside the silica pores along with the amorphous content were relatively unaffected. XRPD of the strong washed samples show no crystalline peaks, proving no surface crystals remained. The DSC curves exhibit a major broadening endothermic peak at 205.3 °C and a small broadening peak at 215.2 °C. Apparently, the second polymorph is a metastable form but we are not sure it is form II or III. Nevertheless, these results prove that complex compounds tend to form metastable polymorphs, or even amorphous content under the rigid confinement.

The last compound we tried is IMC. IMC was hard to crystallize. We used the slow evaporation method and allowed 14 days for crystallization. DSC analysis showed no peaks while the solid-state NMR confirmed it was 100% amorphous content. However, one advantage of amorphous IMC in porous silica is that it is stabilized by the porous matrix. We ran DSC analysis of the samples after one-month storage and no peak was detected indicating no crystallization had occurred.

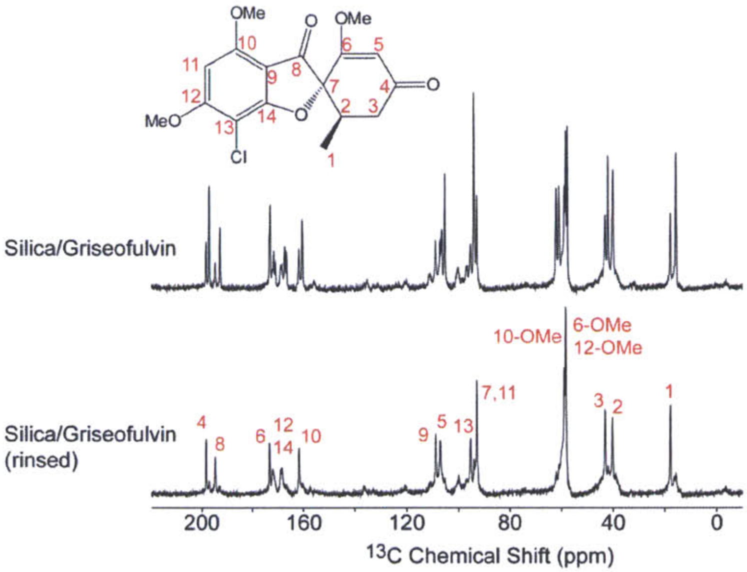

Figure 5-6 $^{13}$C CPMAS spectra of silica-GSF before and after rinsing with dichloromethane. The sharp peaks indicate the presence of crystalline polymorphs and the line broadening at the base suggests amorphous content. The rinsing removed the surface polymorph, so only the pore polymorph and the amorphous content remains.

### 5.3.4 Dissolution test

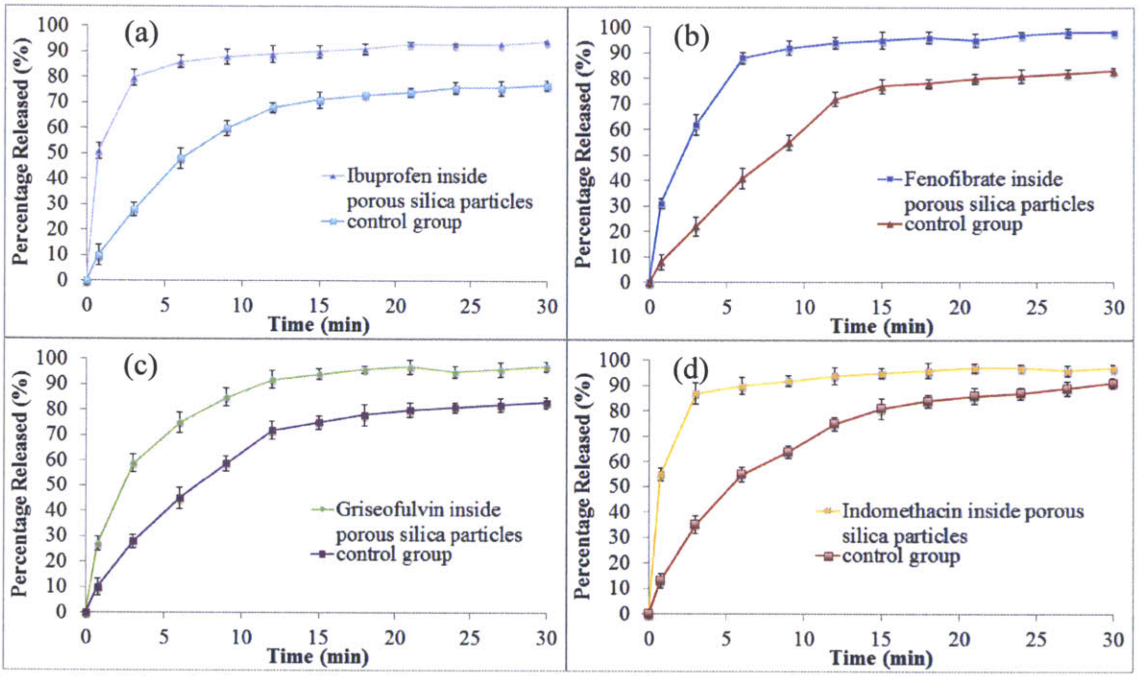

Figure 5-7 Dissolution profiles of compounds loaded in porous silica particles of 40 nm pores: (a) IBP samples of medium wash; (b) FEN samples of strong wash; (c) GSF samples of strong wash; (d) IMC samples of strong wash.

Dissolution profiles of these nanocrystals were tested and the results are shown in Figure 5-7. For ibuprofen, it took only 1 minute to achieve ~ 50% release while the control group needed 6 minutes to reach almost the same percentage. The control group is a physical mixture of porous silica particles and ibuprofen crystals from commercial sources. Similar trends were also seen in FEN, GSF and IMC. These results demonstrate nanocrystals under the rigid confinement can be used as a novel formulation method and will strongly improve the dissolution rates of poorly soluble active pharmaceutical ingredients. In the pharmaceutical industry, making amorphous or nano-crystalline materials is a common practice to enhance the bioavailability of poorly soluble drugs. However, it is difficult to stabilize amorphous or nano-crystalline materials in the formulation, especially for a long time. Our method uses the porous matrix to block the diffusion of moisture, limit the reorganization movement of API molecules and therefore better stabilize the desired state of APIs. In addition, the process is very simple and the samples can be directly formulated into capsules without further formulation.

## 5.4 Conclusions

In summary, by using nano-crystallization under rigid confinement we successfully obtained nano-crystalline ibuprofen, fenofibrate and griseofulvin. The results of dissolution tests successfully illustrate the significant enhancement of dissolution profiles of those compounds when they were presented in the form of nanocrystals inside the rigid confinement. We also used ssNMR in the qualitative and quantitative analysis of compounds nano-crystallized in the confinement.

## 5.5 Reference

1. E. M. Merisko-Liversidge and G. G. Liversidge, *Toxicologic pathology*, 2008, **36**, 43.
2. A. H. Faraji and P. Wipf, *Bioorganic & medicinal chemistry*, 2009, **17**, 2950.
3. M. Wang, G. C. Rutledge, A. S. Myerson and B. L. Trout, *Journal of pharmaceutical sciences*, 2012, **101**, 1178.
4. K. Kim, I. S. Lee, A. Centrone, T. A. Hatton and A. S. Myerson, *Journal of the American Chemical Society*, 2009, **131**, 18212.
5. M. Turk and R. Lietzow, *Journal of Supercritical Fluids*, 2008, **45**, 346.
6. E. Reverchon, G. D. Porta and M. G. Falivene, *Journal of Supercritical Fluids*, 2000, **17**, 239.
7. S. W. Siddiqui, Y. Zhao, A. Kukukova and S. M. Kresta, *Ind. Eng. Chem. Res.*, 2009, **48**, 7945.
8. H. Chioua, H. K. Chana, D. Henga, R. K. Prudhommeb and J. A. Raperc, *Journal of Aerosol Science*, 2008, **39**, 500.
9. M. Sultana, *Thesis: Microfluidic Systems for Continuous Crystallization of small organic molecules*, Masschusetts Institute of Technology, Cambridge, 2010.
10. V. Genota, S. Desportesb, C. Croushorea, J. Lefevrea, R. B. Pansua, J. A. Delairea and P. R. Rohrb, *Chemical Engineering Journal*, 2010, **161**, 234.
11. M. Ildefonso, N. Candoni and S. Veesler, *Crystal Growth & Design*, 2013, **13**, 2107.
12. B. D. Hamilton, M. A. Hillmyer and M. D. Ward, *Crystal Growth & Design*, 2008, **8**, 3368.
13. J.-M. Ha, M. A. Hillmyer and M. D. Ward, *The Journal of Physical Chemistry B*, 2005, **109**, 1392.
14. J.-M. Ha, B. D. Hamilton, M. A. Hillmyer and M. D. Ward, *Crystal Growth & Design*, 2012, **12**, 4494.
15. K. K. Qian and R. H. Bogner, *Journal of pharmaceutical sciences*, 2012, **101**, 444.
16. P. Maheshwari, D. Dutta, S. K. Sharma, K. Sudarshan, P. K. Pujari, M. Majumder, B. Pahari, B. Bandyopadhyay, K. Ghoshray and A. Ghoshray, *The Journal of Physical Chemistry C*, 2010, **114**, 4966.
17. J. M. Ha, J. H. Wolf, M. A. Hillmyer and M. D. Ward, *J. Am. Chem. Soc.*, 2004, **126**, 3382.
18. J.-M. Ha, B. D. Hamilton, M. A. Hillmyer and M. D. Ward, *Crystal Growth & Design*, 2009, **9**, 4766.
19. E. Skorupska, A. Jeziorna, S. Kazmierski and M. J. Potrzebowski, *Solid State Nucl Mag*, 2014, **57-58**, 2.
20. F. G. Vogt, *Future Med Chem*, 2010, **2**, 915.
21. J. M. Griffin, D. R. Martin and S. P. Brown, *Angew Chem Int Edit*, 2007, **46**, 8036.
22. T. J. Offerdahl, J. S. Salsbury, Z. D. Dong, D. J. W. Grant, S. A. Schroeder, I. Prakash, E. M. Gorman, D. H. Barich and E. J. Munson, *J Pharm Sci-Us*, 2005, **94**, 2591.
23. J. W. Lubach, D. W. Xu, B. E. Segmuller and E. J. Munson, *J Pharm Sci-Us*, 2007, **96**, 777.

24. D. H. Barich, J. M. Davis, L. J. Schieber, M. T. Zell and E. J. Munson, *J Pharm Sci-Us*, 2006, **95**, 1586.
25. K. Masuda, S. Tabata, H. Kono, Y. Sakata, T. Hayase, E. Yonemochi and K. Terada, *Int J Pharm*, 2006, **318**, 146.
26. R. K. Harris, *Analyst*, 2006, **131**, 351.
27. M. Geppi, G. Mollica, S. Borsacchi and C. A. Veracini, *Appl Spectrosc Rev*, 2008, **43**, 202.
28. T. N. Pham, S. A. Watson, A. J. Edwards, M. Chavda, J. S. Clawson, M. Strohmeier and F. G. Vogt, *Mol Pharmaceut*, 2010, **7**, 1667.
29. J. W. Lubach, B. E. Padden, S. L. Winslow, J. S. Salsbury, D. B. Masters, E. M. Topp and E. J. Munson, *Anal Bioanal Chem*, 2004, **378**, 1504.
30. T. Azais, C. Tourne-Peteilh, F. Aussenac, N. Baccile, C. Coelho, J. M. Devoisselle and F. Babonneau, *Chem Mater*, 2006, **18**, 6382.
31. A. J. Rossini, A. Zagdoun, M. Lelli, J. Canivet, S. Aguado, O. Ouari, P. Tordo, M. Rosay, W. E. Maas, C. Coperet, D. Farrusseng, L. Emsley and A. Lesage, *Angew Chem Int Edit*, 2012, **51**, 123.
32. A. Lesage, M. Lelli, D. Gajan, M. A. Caporini, V. Vitzthum, P. Miéville, J. Alauzun, A. Roussey, C. Thieuleux, A. Mehdi, G. Bodenhausen, C. Coperet and L. Emsley, *Journal of the American Chemical Society*, 2010, **132**, 15459.
33. T. Kobayashi, O. Lafon, A. S. Lilly Thankamony, I. I. Slowing, K. Kandel, D. Carnevale, V. Vitzthum, H. Vezin, J.-P. Amoureux, G. Bodenhausen and M. Pruski, *Physical Chemistry Chemical Physics*, 2013, **15**, 5553.
34. W. R. Gunther, V. K. Michaelis, M. A. Caporini, R. G. Griffin and Y. Román-Leshkov, *Journal of the American Chemical Society*, 2014, **136**, 6219.
35. T. C. Ong, M. L. Mak-Jurkauskas, J. J. Walish, V. K. Michaelis, B. Corzilius, A. A. Smith, A. M. Clausen, J. C. Cheetham, T. M. Swager and R. G. Griffin, *J Phys Chem B*, 2013, **117**, 3040.
36. A. J. Rossini, C. M. Widdifield, A. Zagdoun, M. Lelli, M. Schwarzwalder, C. Coperet, A. Lesage and L. Emsley, *J Am Chem Soc*, 2014, **136**, 2324.
37. A. Pines, J. S. Waugh and M. G. Gibby, *J Chem Phys*, 1972, **56**, 1776.
38. R. L. Vold, J. S. Waugh, M. P. Klein and D. E. Phelps, *J Chem Phys*, 1968, **48**, 3831.
39. R. Freeman and H. D. W. Hill, *J Chem Phys*, 1971, **54**, 3367.
40. A. E. Bennett, C. M. Rienstra, M. Auger, K. V. Lakshmi and R. G. Griffin, *J Chem Phys*, 1995, **103**, 6951.
41. X. Yang, B. Sarma and A. S. Myerson, *Crystal Growth & Design*, 2012, **12**, 5521.
42. P. Derollez, E. Dudognon, F. Affouard, F. Danede, N. T. Correia and M. Descamps, *Acta Crystallographica Section B*, 2010, **66**, 76.
43. A. Mahieu, J.-f. Willart, E. Dudognon, M. D. Eddleston, W. Jones, F. Danède and M. Descamps, *Journal of pharmaceutical sciences*, 2013, **102**, 462.
44. G. K. Balendiran, N. Rath, A. Kotheimer, C. Miller, M. Zeller and N. P. Rath, *Journal of pharmaceutical sciences*, 2012, **101**, 1555.
45. S. A. Surwase, J. P. Boetker, D. Saville, B. J. Boyd, K. C. Gordon, L. Peltonen and C. J. Strachan, *Molecular Pharmaceutics*, 2013, **10**, 4472.
46. J. P. Bradley, PhD, University of Warwick, 2011.

47. S. G. Levine, R. E. Hicks, H. E. Gottlieb and E. Wenkert, *J Org Chem*, 1975, **40**, 2540.
48. T. J. Simpson and J. S. E. Holker, *Phytochemistry*, 1977, **16**, 229.

## 5.6 Appendix

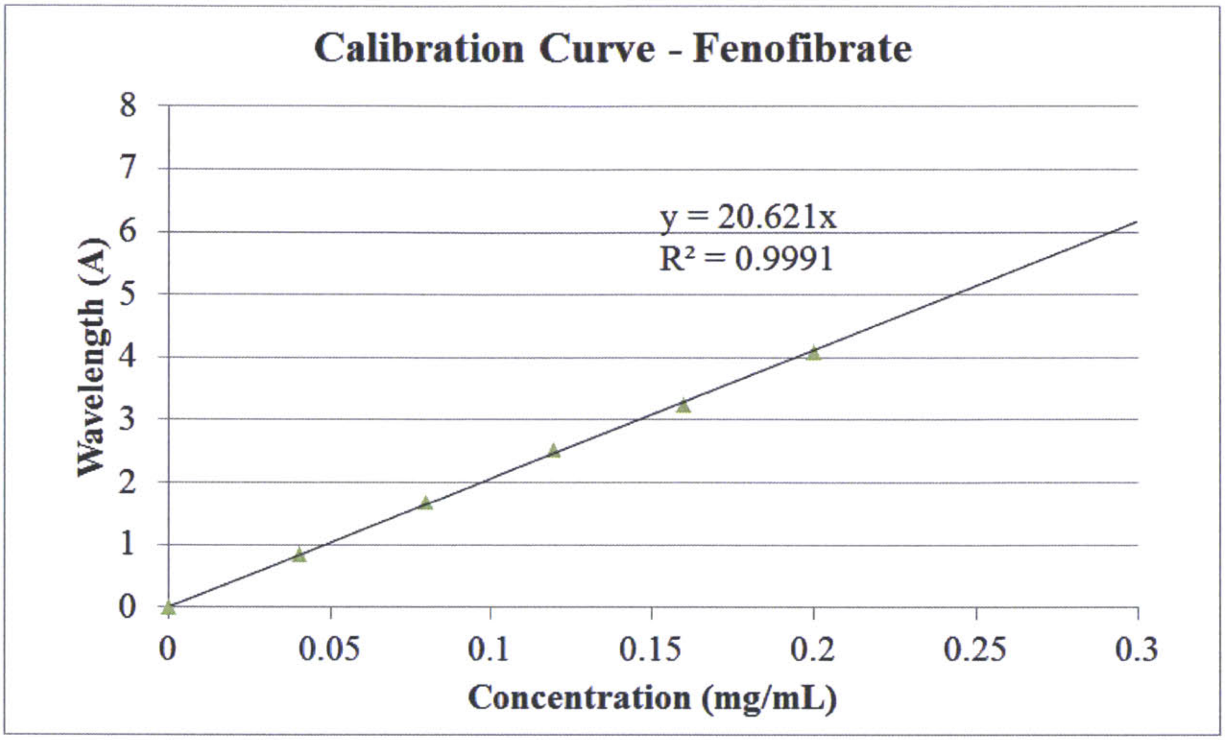

Figure 5-8 Fenofibrate calibration curve using UV-Vis

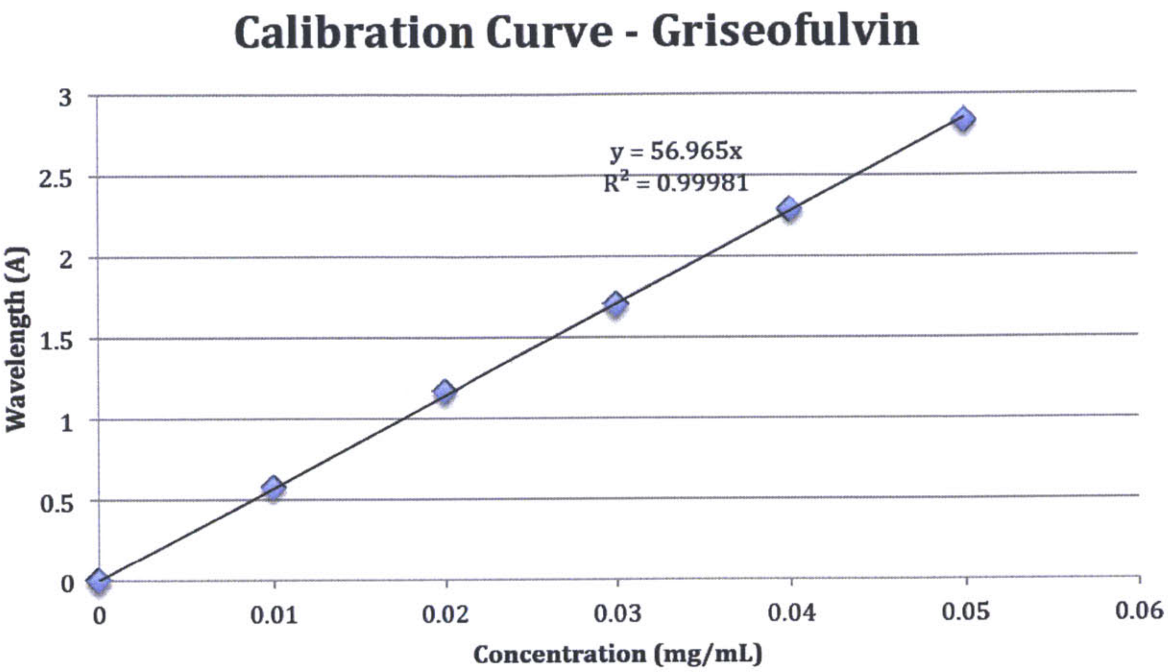

Figure 5-9 Griseofulvin calibration curve using UV-Vis

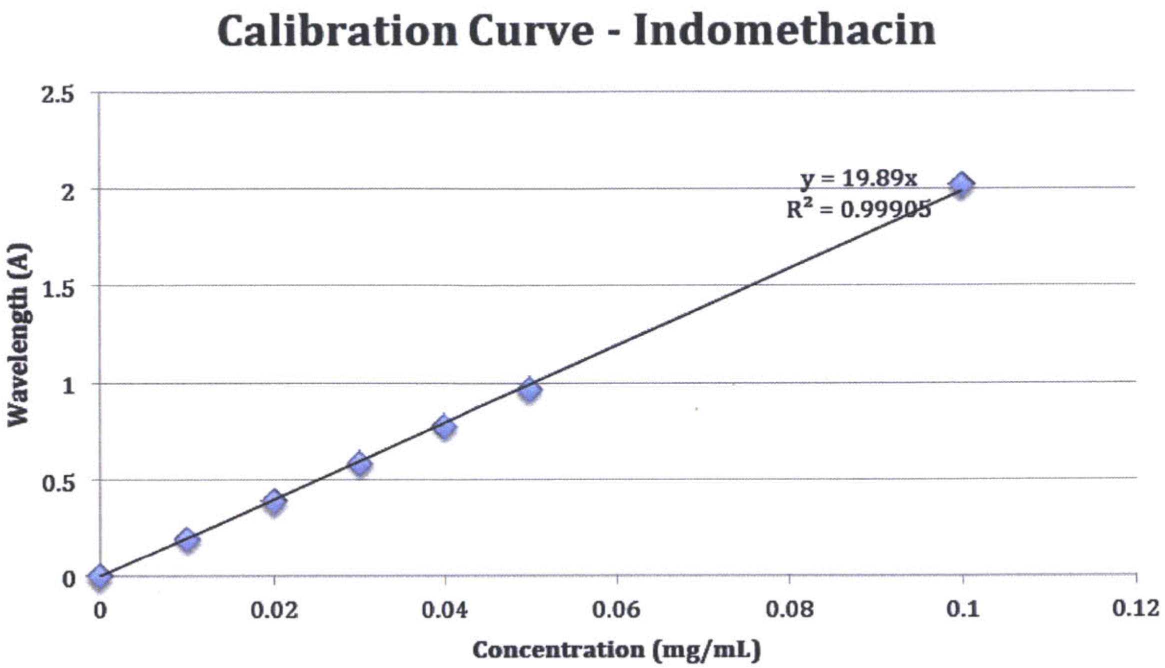

Figure 5-10 Indomethacin calibration curve using UV-Vis

Table 5-5. $^{13}$C chemical shifts of silica-griseofulvin polymorphs

| **Surface Polymorph (δ, ppm)** | **Pore Polymorph (δ, ppm)** | **Assignment** |
|---|---|---|
| 197.08 | 198.34 | 4 |
| 192.86 | 194.75 | 8 |
| 172.81 | 172.81 | 6 |
| 171.40 | 170.72 | 12 |
| 167.04 | 168.73 | 14 |
| 160.34 | 161.65 | 10 |
| 106.46 | 108.79 | 9 |
| 105.15 | 106.99 | 5 |
| 94.03 | 95.29 | 13 |
|  | 92.86 | 7,11 |
| 61.99 | 58.79 | 10-OMe |
| 60.97 | 58.30 | 6-OMe |
| 57.67 |  | 12-OMe |
| 41.95 | 43.01 | 3 |
| 40.00 | 40.00 | 2 |
| 15.59 | 17.77 | 1 |

# 6 Nanocrystal Formation and Polymorphism of Glycine

The surface of a crystal may play an important role in its physical and chemical properties. The percentage of molecules that are exposed on surfaces increases significantly as the crystal size decreases. However, the role of surface molecules and crystal size on the physiochemical properties of crystals is poorly understood. Here, using glycine as a model compound, nano-sized crystals were obtained by two different methods – nano spray drying and bi-functional self-assembled monolayers (SAMs). The surface structures of these nanocrystals were examined and the solubility was measured as a function of size for both the α-form and β-form. It was found that the disordered surface structures may promote molecule mobility and cause "crystal-bridging" to form larger crystals. In addition, our results show that the solubility ratio of β-form/α-form changes as size varies indicating the importance of the surface molecules.

## 6.1 Introduction

Research on crystal surfaces at the nano and molecular scale is of great interest.[1-6] From a molecular perspective, molecules on the surface are very unique. First, they are different from molecules in the bulk. Second, even surface molecules on the same crystal could be different. Crystals have facets and therefore different surfaces of the same crystal, if not symmetric, arrange molecules in different ways.[7] Previously, sork has focused on bulk properties, such as solubility and melting point, and tend to ignore crystal surface or consider molecules on the surface the same as molecules in the bulk.[8] This is generally correct for most cases where surface molecules contribute little. However, surface molecules play a vital role in some cases. One example is crystal growth mechanism. The way that molecules arrange themselves and grow on surfaces is poorly understood.[9] Recently, Ward and his co-workers utilized a real-time in situ atomic force microscope (AFM) and found that L-cystine dimethylester and L-cystine methylester inhibits the growth of the six symmetry-equivalent {100 steps due to specific bindings at the crystal surface.[10] Zhao et al. showed that graphene primarily grows on copper single crystal facets (100) and (111) using atomic-resolution scanning tunnelling microscopy (STM).[11] Another good example is nanocrystals. As particle size goes down, the fraction of surface molecules in a crystal increases significantly. Compared to bulk molecules, molecules on surfaces possess fewer interactions in the structure and tend to leave the surface. In order to consider the importance of surface molecules in such circumstances, the Ostwald-Freundlich equation and the Gibbs–Thomson equation were derived and can be used to roughly describe some physiochemical properties' change as particles size reduces.[12]

Organic compounds, rather than inorganic systems, normally exhibit more crystal defects.[13] Most organic molecules form molecular crystal structures by intermolecular and intramolecular forces. Compared to ionic and covalent bonds, the intermolecular forces in molecular crystals are generally weak, including electrostatic interaction between dipoles, dispersion forces and hydrogen bonds.[8] Besides, most organic molecules are non-simply shaped and anisotropic. Therefore, organic solids show more complex structures and are commonly hard to crystallize. Crystal defects are easily incorporated into the structure, especially near the surface.[8, 13]

In this work, we selected glycine as the model compound. Glycine is the simplest organic molecule, and exhibits six different polymorphs.[14] Three of them can be obtained at under room temperature and pressure (α, β and γ). The stability order of them is γ > α > βFor crystals above 1 micron, were surface molecules do not have a significant influence on bulk properties, the ratio of the solubility of polymorphs is a constant at a given temperature. It is the goal of this work to determine if this is also the case for crystals below one micron, were surface molecules have an increasing importance the properties such as solubility.

## 6.2 Experimental Section

### 6.2.1 Materials

Glycine (ReagentPlus®, ⩾99%) and water (CHROMASOLV® Plus) were obtained from Sigma Aldrich. 200 proof ethanol was obtained from VWR.

### 6.2.2 X-Ray Powder Diffraction (XRPD) analysis

The instrument (X'Pert PRO, PANalytical Inc.) is equipped with a PW3050/60 standard resolution goniometer and a PW3373/10 Cu LFF DK241245 X-ray tube. The high tension generator high voltage and anode current were set as 45 kv and 40 mA when using. A spinner sample stage PW3064 (Reflection mode) was used for all the samples. Settings on incident bean path include: soller slit 0.04 rad., mask fixed 10 mm, programmable divergence slit and fixed 1° anti-scatter slit. Settings on diffracted beam path include: soller slit 0.04 rad and programmable anti-scatter slit. The scan was programmed as a continuous scan: 2θ angle 2-40°, step size 0.0083556°, time per step 19.685 s; three repeated scans were collected to average.

### 6.2.3 Raman analysis

We used Horiba Jobin-Yvon Labram HR800 spectrometer equipped with a 514 nm line using 1800 grooves/mm and a 100x microscope objective. One benefit of gold islands is that the Raman signal is enhanced due to the surface-enhanced effect by gold. The characteristic peaks 2972/3008 $cm^{-1}$ for $\alpha$-form, 2953/3010 $cm^{-1}$ for $\beta$-form and 2964/3000 $cm^{-1}$ for $\gamma$-form were used for polymorph characterization.

### 6.2.4 Experimental Setup

The setup was quite complex and we only describe three generalized steps here for simplicity (Figure 6-1). Patterned gold substrates with island size 1 μm were first prepared in MIT microsystems technology laboratories. Silicon substrate was patterned by photolithography first, coated with 5 nm titanium layer and 50 nm gold layer. The rest photoresist were stripped off by immersing the substrates in acetone for 2 hours. After being cleaned and dried with a nitrogen gun, the substrates with gold islands were ready to prepare bi-functional self-assembled monolayers (SAMs). Fabricated substrates with patterned gold islands as mentioned above were cleaned with piranha solution (A typical mixture of 3:1 concentrated sulfuric acid to 30% hydrogen peroxide solution) for 20 minutes for the cleaning of all organic impurities from the surface. Substrates were then washed with copious amount of pure water and isopropanol then dried with nitrogen gun. Cleaned patterned substrates were slowly put into a 10 mM thiol/ethanol (3-mercaptopropionic acid, 3MPA) solution in pure nitrogen atmosphere for 18 hours for the formation of hydrophilic SAMs on gold islands, i.e. –COOH group of 3MPA exposing outwards. Substrates were rinsed three times with pure ethanol and dried with nitrogen gas and immersed into a 2 mM OTS (n-Octadecyltrichlorosilane)/toluene solution for 40 minutes for the formation of hydrophobic SAMs on the remaining silicon surface. After being rinsed 3 times with pure toluene and dried with nitrogen gas, the bi-functional SAMs substrates were ready with hydrophilic thiol on gold islands and hydrophobic OTS on the remaining silicon area for the crystallization of MA. Surfaces were scanned under Atomic Force Microscope (AFM). The roughness of these gold island surfaces were at most ±2 nm. These bi-functional SAMs substrates were then used under different slow evaporation and anti-solvent crystallization conditions to obtain the desired polymorphic outcome. More details can be found in chapter 3 and appendix.

### 6.2.5 Solubility test

Glycine/ethanol solutions of different supersaturated concentrations were carefully prepared just before we tested the solubility of nanocrystals. Glycine was recrystallized to eliminate possible impurities in commercial bottles and ethanol was filtered with 0.2 μm Whatman® Anotop syringe filters before use as well. The solubility of bulk glycine crystals in ethanol at 25 °C was tested using gravimetric method to be 0.263 ± 0.015 mg glycine/g solution for α-form and 0.309 ± 0.008 mg glycine/g solution for β-form. For example, to prepare a solution of supersaturation S = 1.1, we put ~ 0.34 g glycine into ~ 1000 g ethanol and stirred the slurry on a hot plate. We gradually increased the temperature until crystals were full dissolved. Then we raised the temperature by another 5 °C and held it for another 30minutes to ensure the dissolving of invisible particles. The stability of the prepared supersaturated solutions was not good but they normally remained clear within a couple of hours. We tested one sample by putting it into the solution and check whether the crystals dissolve or not. If not, a higher concentration solution will be used. Finally, solubility of the sample is defined as the average of concentrations of the solution dissolving it and the one before that.

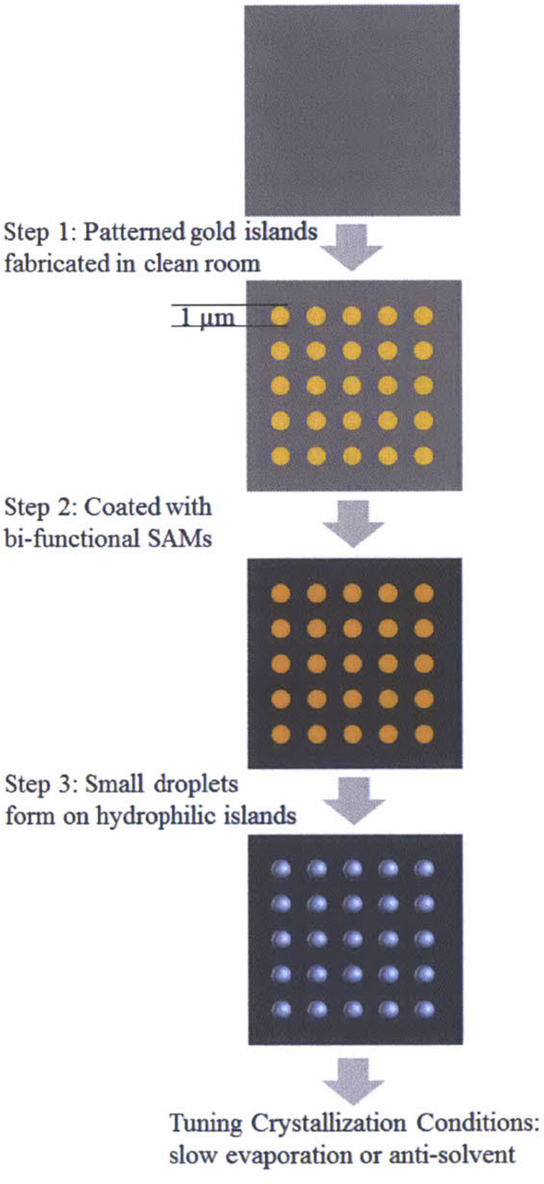

Figure 6-1 Illustration of steps to achieve droplet crystallization on bi-functional SAMs substrates.

## 6.3 Results and discussion

### 6.3.1 Nanocrystals obtained on bi-functional SAMs substrates

Previously we have showed using substrates of 1 μm gold islands coated with bi-functional Self-Assembled Monolayers (SAMs) to produced nano-sized mefenamic acid crystals with controlled polymorphs as small as ~ 300 nm.[6] Here we utilized the same technique to produce nanocrystals of different glycine polymorphs. Instead of varying surface chemistry, we controlled polymorphic outcome by changing solution pH and crystallization conditions (slow diffusion of anti-solvent or slow evaporation[6]). Figure 6-2a shows glycine nanocrystals on 1 μm gold islands from a glycine/water solution of 0.207 g glycine/g solution. The largest dimension of these nanocrystals is from 683 nm to 1.19 μm. Unlike nanocrystals formed using nano spray dryer, most of the nanocrystals here clearly showed needle-like shapes. Figure 6-2b shows glycine nanocrystals on 1 μm gold islands from a glycine/water solution of 0.011 g glycine/g solution. Due to the limit of focus depth of optical microscope, the left region of the image is blurry but one dot per island is clear. Besides, the crystal size is already under wavelength of visible lights, and is probably almost the same as resolution limit of that objective lens in the microscope, so the shape is hardly seen here. Figure 6-2c shows an AFM resolution image of one of the nanocrystals, and a crystal-like shape rather than a sphere can be easily distinguished. These results suggest that nano-crystallization under these experimental conditions is much slow and the crystal structure of these nanocrystals is much better organized than that of nanocrystals formed by spraying. The largest dimension of these nanocrystals is from 210 nm to 418 nm.

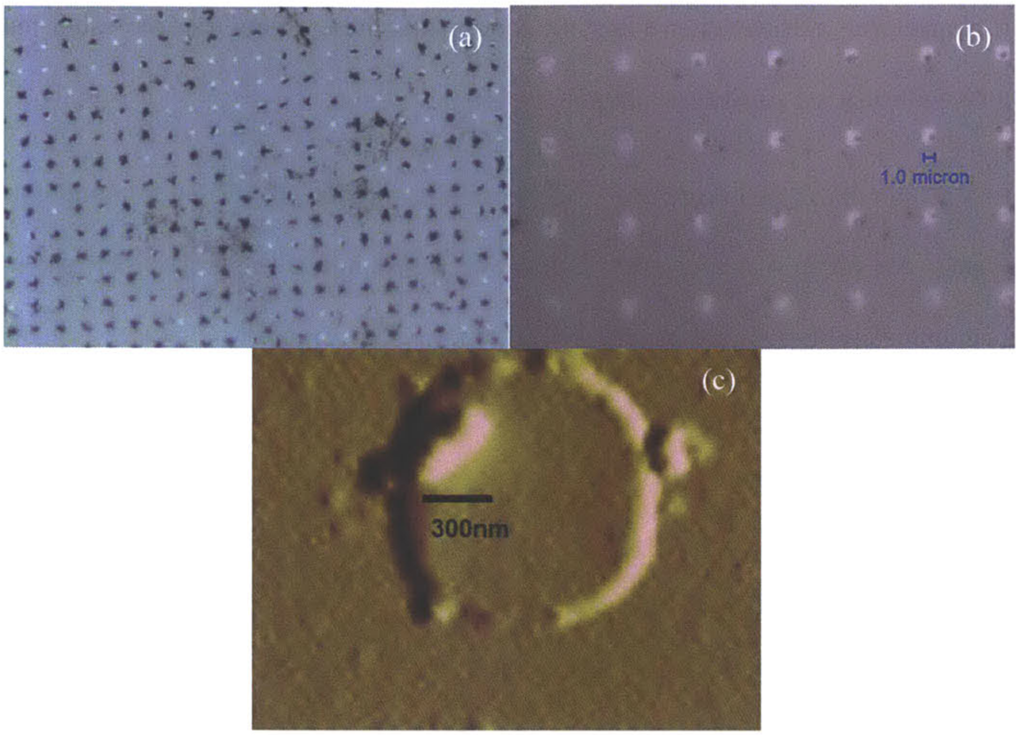

Figure 6-2 Images of nanocrystals formed on bi-functional SAMs substrates. (a) Nanocrystals from a glycine/water solution of 0.207 g glycine/g solution. Black dirt was photoresist residue left. (b) Nanocrystals from a glycine/water solution of 0.011 g glycine/g solution. (c) One of the nanocrystals in (b) under AFM.

Previous work in our laboratory obtained mostly β-glycine nanocrystals.[15, 16] Here, we successfully obtained mostly α-glycine when we waited for a longer time (more than a month), and varied the surface chemistry (hydrophilic SAMs with -COOH) and island sizes. Solubility vs size curves of both polymorphs were tested as shown in Figure 6-3. Compared to the bulk solubility, 286 ± 25 nm α-glycine nanocrystals showed 19.8% increase and 229 ± 32 nm β-glycine nanocrystals exhibited 16.4% enhancement in solubility. Using the Ostwald-Freundlich equation surface tensions for α-glycine and β-glycine were calculated to be 2729 and 1826 erg/cm$^2$, respectively. However, we are not certain that these values can represent nanocrystals with 100% well-ordered surface structures.

Those two fitted curves will cross at r = 97 nm, indicating that β-glycine is more stable than α-glycine due to the effect of surface molecules. Similar results on the same order of magnitude of size-dependent stability of polymorphs were reported on organic molecular crystals such as anthranilic acid.[17, 18] The metastable form II persisted in 7.5 nm pores and was believed to possess a smaller cluster size.

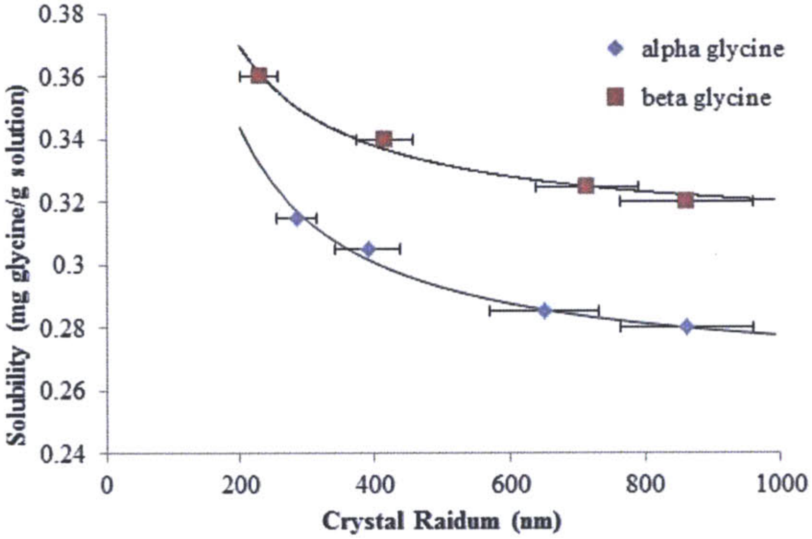

Figure 6-3 Solubility curves of different polymorphs of glycine. Two black lines are fitted curves using the Ostwald-Freundlich equation ($R^2 = 0.981$ for α-glycine and 0.983 for β-glycine).

### 6.3.2 Nanocrystals obtained by nano spray drying

We also used Buchi nano spray dryer (model B-90) to obtain glycine nanocrystals. The smallest spray mesh (hole diameter is 4.0 μm) was used in all experiments. A glycine/water solution was sprayed from a spraying head through the mesh, and solvent evaporates for crystallization during falling of droplets. The role of experimental conditions, such as solution concentration, pH and temperature, on the size and polymorphic outcome were explored as shown in Table 6-1. In many cases, we see concomitant nucleation of at least two polymorphs. This is consistent with literature.[15, 19, 20] As temperature decreases and pH changes to acidic/basic, more stable forms (α and γ) start to show. As solution concentration decreases, size reduction of product particles was not obvious. It can be explained by the relationship between a particle's diameter (d) and its volume (V): d is proportional to $V^{1/3}$ ($d \sim V^{1/3}$). However, the particle's volume (V) is proportional to the solution concentration (C) ($V \sim C$), assuming the volume of one droplet coming from the mesh the same every time spraying. Therefore, the relationship is $d \sim C^{1/3}$. Even when the solution concentration decreased to 1/5 of its original value, the particle size only reduces to 58% of its original number.

Table 6-1 Polymorphic outcome of glycine nanocrystals formed using spraying analyzed by XRPD

| **Glycine/water solution (0.106 g glycine/g solution)** | | | |
|---|---|---|---|
| | pH = 2 | pH = 6 | pH = 10 |
| **T = 75 °C** | 18% α, 82% β | 13% α, 87% β | α, β, γ (18:47:35) |
| **T = 95 °C** | 100% β | 100% β | α, β, γ (7:82:11) |
| **Glycine/water solution (0.021 g glycine/g solution)** | | | |
| | pH = 2 | pH = 6 | pH = 10 |
| **T = 75 °C** | α, β, γ (13:68:19) | 21% α, 79% β | α, β, γ (10:52:38) |
| **T = 95 °C** | 12% α, 88% β | 15% α, 85% β | α, β, γ (14:80:6) |

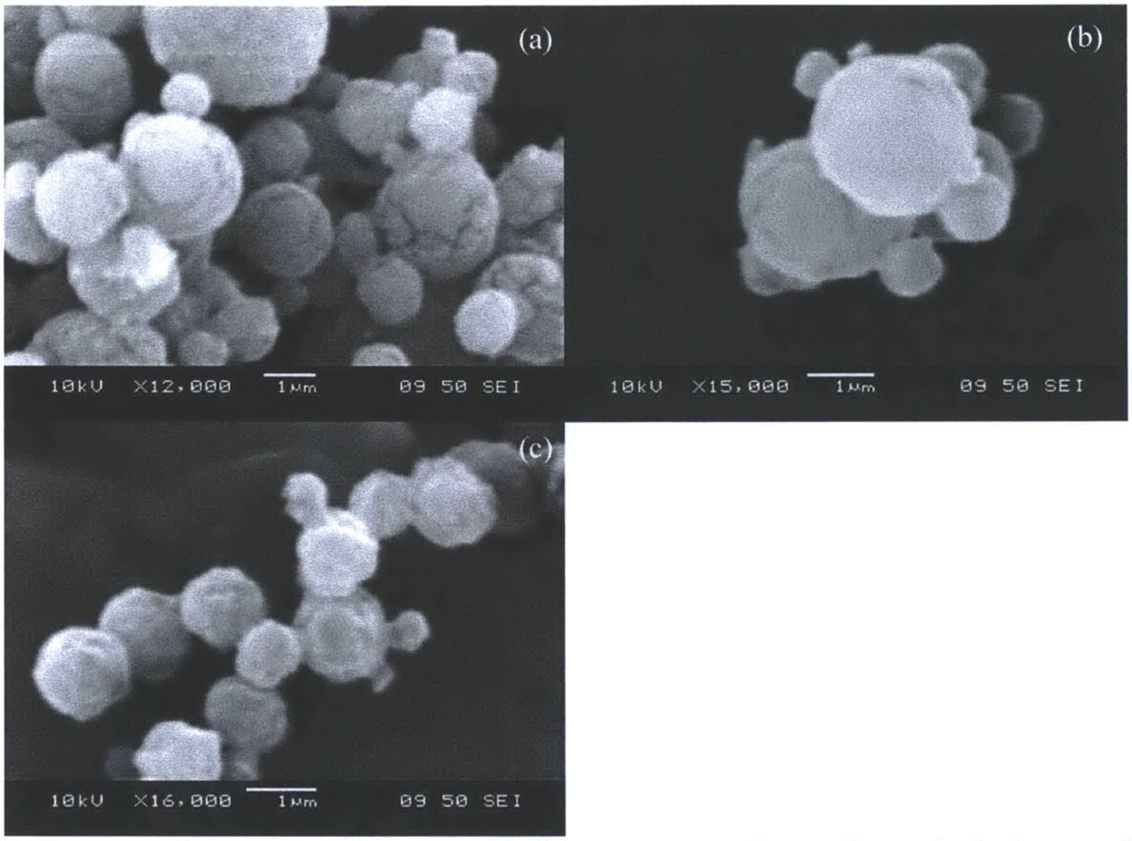

Figure 6-4 SEM images of nanocrystals from nano spray dryer using a glycine/water solution (0.021 g/g solution) at 95 °C. A 20-nm gold layer was coated. (a) and (b) were images taken immediately after the spraying. (c) was taken 2 hours after the spraying.

Figure 6-4 shows the result of spraying a glycine/water solution (0.021 g/g solution) at 95 °C. The size of particles exhibits a wide distribution from ~ 200 nm to ~ 3 μm, indicating that droplets coming from the mesh are quite different in size as well. The shapes of these particles are spherical without any sign of crystal facets. A particle is possibly not a single crystal but many crystalline domains. As one droplet falls down, free fall movement only takes 0.45 seconds to pass a distance of 1 meter. When solvent evaporates in such a short f time, it is possible that multiple nucleation events happen, or many defects are generated during crystal growth even when there is only one nucleus. Interestingly, we did not observe any amorphous materials in the XRPD analysis which was conducted right after the spraying. Figure 6-4c is the image of the same sample which was taken 2 hours after the other two images. One noticeable change is that these crystals start to form connections with adjacent crystals.. The sample was stored under ambient conditions which were tested to be 23°C and 35%RH. From the molecular perspective, glycine molecules, especially those on the surface of particles, showed very high mobility. It is strongly related to the poorly ordered crystal structure at the surface. This "crystal-bridging" phenomenon indicates that these nanocrystals formed using nano spray dryer are not stable when they are piled together and possess a high tendency to form bigger crystals through the "crystal-bridging". These nanocrystals, nonetheless, cannot be tested for solubility vs size. Although number based percentage of crystals of size $< 1$ μm are more than half, volume based percentage of those are at most 20%. When we put the sample into a solution of a certain concentration, it is hard to visually distinguish whether the crystals dissolve or not.

## 6.4 Conclusion

In conclusion, crystal surface is a vital part of organic molecular nanocrystals. Through nano spray drying, we obtained spherical nanocrystals with disordered surface structures. These defects on crystal surfaces may significantly enhance mobility of molecules and therefore big crystals form by "crystal-bridging". Second, using bi-functional SAMs substrates, we obtained glycine nanocrystals with narrow size distributions and controlled polymorphs. We found that the solubility ratio of β-glycine/α-glycine changes as crystal size reduces. The most similar reports were that many researchers demonstrated melting point depression of nanocrystals and size-dependent stability of polymorphs under confinement.[17, 18, 21-24] To the best of our knowledge, no one has reported similar findings for organic molecular nanocrystals which are open to free space. Our results help further understand the importance of surface molecules in organic molecule crystals, especially nanocrystals. In addition, we believe, with more knowledge towards surface of polymorphs, methods to produce organic molecular nanocrystals with desired polymorph and properties will become feasible in industry.

## 6.5 Reference

1. I. Halasz and H. Vančik, *CrystEngComm*, 2011, **13**, 4307.
2. Y. Diao, A. S. Myerson, T. A. Hatton and B. L. Trout, *Langmuir : the ACS journal of surfaces and colloids*, 2011, **27**, 5324.
3. Y. Diao, T. Harada, A. S. Myerson, T. A. Hatton and B. L. Trout, *Nat Mater*, 2011, **10**, 867-871.
4. A. D. Daigle and J. J. BelBruno, *Surface Science*, 2011, **605**, 1313.
5. K. Chadwick, J. Chen, A. S. Myerson and B. L. Trout, *Crystal Growth & Design*, 2012, **12**, 1159.
6. X. Yang, B. Sarma and A. S. Myerson, *Crystal Growth & Design*, 2012, **12**, 5521.
7. C. P. Price, A. L. Grzesiak and A. J. Matzger, *Journal of the American Chemical Society*, 2005, **127**, 5512.
8. A. S. Myerson, *Handbook of Industrial Crystallization*, Butterworth-Heinemann, 2002.
9. R. Mohan and A. S. Myerson, *Chem Eng Sci*, 2002, **57**, 4277.
10. J. D. Rimer, Z. An, Z. Zhu, M. H. Lee, D. S. Goldfarb, J. A. Wesson and M. D. Ward, *Science*, 2010, **330**, 337.
11. L. Zhao, K. T. Rim, H. Zhou, R. He, T. F. Heinz, A. Pinczuk, G. W. Flynn and A. N. Pasupathy, *Solid State Communications*, 2011, **151**, 509.
12. W. Wu and G. H. Nancollas, *Journal of solution chemistry*, 1998, **27**, 521.
13. D. S. Chemla, *Nonlinear optical properties of organic molecules and crystals*, Elsevier, 2012.
14. S. V. Goryainov, E. V. Boldyreva and E. N. Kolesnik, *Chemical Physics Letters*, 2006, **419**, 496.
15. K. Kim, A. Centrone, T. A. Hatton and A. S. Myerson, *Crystengcomm*, 2011, **13**, 1127.
16. K. Kim, I. S. Lee, A. Centrone, T. A. Hatton and A. S. Myerson, *Journal of the American Chemical Society*, 2009, **131**, 18212.
17. J. M. Ha, J. H. Wolf, M. A. Hillmyer and M. D. Ward, *J. Am. Chem. Soc.*, 2004, **126**, 3382.
18. J.-M. Ha, B. D. Hamilton, M. A. Hillmyer and M. D. Ward, *Crystal Growth & Design*, 2009, **9**, 4766.
19. A. Singh, I. S. Lee and A. S. Myerson, *Crystal Growth & Design*, 2009, **9**, 1182.
20. I. S. Lee, A. Y. Lee and A. S. Myerson, *Pharmaceutical research*, 2008, **25**, 960.
21. Q. Jiang, C. Hu and M. D. Ward, *Journal of the American Chemical Society*, 2013, **135**, 2144.
22. B. D. Hamilton, M. A. Hillmyer and M. D. Ward, *Crystal Growth & Design*, 2008, **8**, 3368.
23. J.-M. Ha, M. A. Hillmyer and M. D. Ward, *The Journal of Physical Chemistry B*, 2005, **109**, 1392.
24. D. Knezic, J. Zaccaro and A. S. Myerson, *Crystal Growth & Design*, 2004, **4**, 199.

## 6.6 Appendix

Patterns made by photolithograph and electron beam lithography:

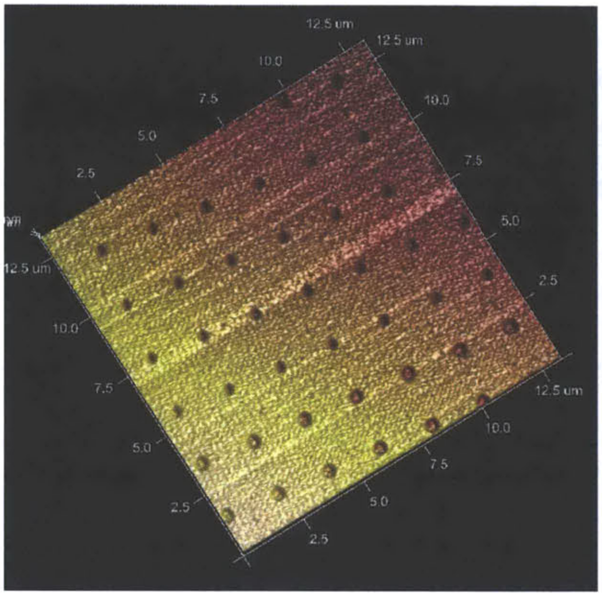

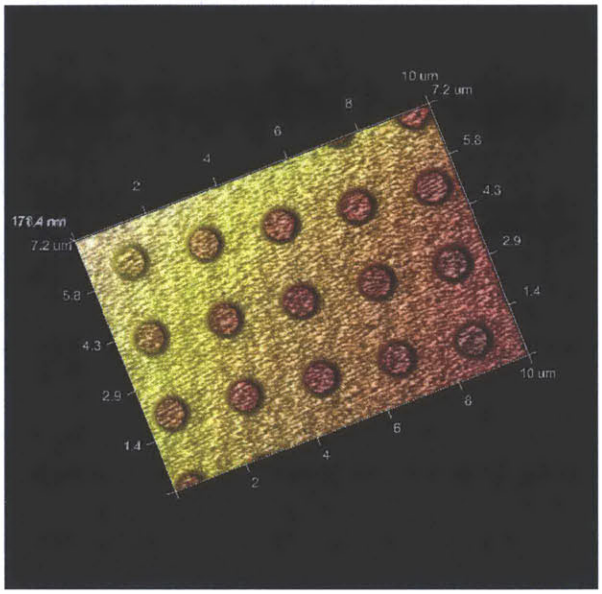

# 7 SEPARATION AND ENRICHMENT OD ENANTIOPURE FROM RACEMIC COMPOUNDS USING MAGNETIC LEVITATION

Crystallization of a solution with high enantiomeric excess can generate a mixture of crystals of the desired enantiomer and the racemic compound. Using a mixture of S-/RS-ibuprofen crystals as a model, we demonstrated that magnetic levitation (MagLev) is a useful technique for analysis, separation and enantioenrichment of chiral/racemic products.

## 7.1 Introduction

The enantiomeric purity of pharmaceutical compounds is important because enantiomers/racemates of a drug can have different effects (i.e. therapeutic or harmful).[1] In the late 1950s, the racemic mixture of Thalidomide, for example, was widely prescribed to relieve the symptoms of morning sickness in pregnant women. Nevertheless, the drug was withdrawn in 1962 after a birth defects crisis, where it was later discovered that the (R) enantiomer is effective against morning sickness while the (S) enantiomer causes birth defects.[2] Apart from therapeutic effects and safety, efficacy of a pure enantiomer is another area of interest.[3] For example, S-ibuprofen has anti-inflammatory activity that is 150 times higher than that of R-ibuprofen.[4] As a result, this subject is not only of interest to pharmaceutical companies but also to the Food and Drug Administration (FDA) who tends to verifying and marketing most chiral drugs as single enantiomers. In fact, in 2006, approximately 80% of small-molecule drugs approved by the FDA were chiral and 75% of them were single enantiomers.[5] There is need to develop new approaches to analyze enantiomeric purity and obtain pure enantiomers. Asymmetric synthesis, chiral resolution and isolation of enantiomerically pure compounds (e.g., from biological sources) are common methods to produce enantiopure compounds.[6] In many cases, even with efficient purifications, the products are a mixture of the desired enantiomer and a small or considerable amount of the undesired enantiomer. For example, the active pharmaceutical ingredient used in the treatment of Parkinson's disease (L-3,4-dihydroxyphenylalanine), is manufactured with an asymmetric synthesis step yielding 95%ee.[6] After synthesis, L-enantiomer is purified by either high-performance liquid chromatography (HPLC) or formation of diastereomers followed by crystallization. These two methods, though commonly used to obtain single enantiomers, have three disadvantages: (i) Separation by HPLC require expensive instrumentation and stationary phase.[1] (ii) A particular chiral stationary phase may only work for a limited number of compounds.[6,7] (iii) Formation of diastereomers introduces another compound into the system, and requires additional crystallization and filtration steps.[7]

One of the alternative approaches to solution-based separation of enantiomers is to purify the desired enantiomer from a mixture of crystals of enantiomerically pure and racemic compound. Given a solution with high enantiomeric excess, one crystallization step usually generates crystals of the desired enantiomer contaminated with crystals of the racemic compound.[8,9] Since the racemic compound and pure enantiomers have different densities, MagLev can be used as a cost-effective, and non-destructive method to separate the enantiomerically pure crystals (desired products) from the racemic compound crystals ("impurity").

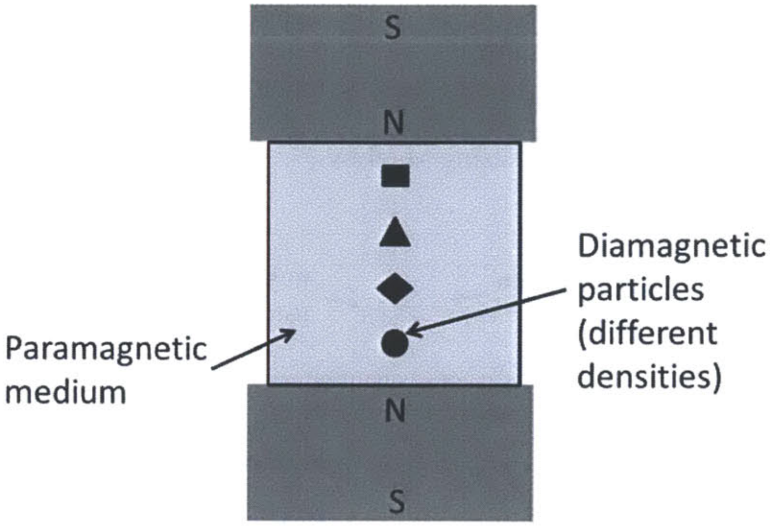

Figure 7-1 Diamagnetic particles with different densities suspended in a paramagnetic medium can be levitated to different heights when container is placed between the magnets of MagLev device.

The theory of MagLev is described in details elsewhere.[10,11,12] Briefly, under the influence of an external magnetic field, dia-magnetic materials of different densities (suspended in a para-magnetic medium) can be levitated to different heights by the balance of magnetic and gravitational forces (Figure 7-1). Since most materials (especially most organic compounds) are diamagnetic, MagLev can find broad applications in density-based analysis and separations in the pharmaceutical industry. We have demonstrated the use of MagLev to separate mixtures of crystal polymorphs.[13] Here, we describe the use of MagLev for analysis of enantiomeric purity and enrichment (Figure 7-2). We selected a mixture of enantiomerically pure and racemic crystals of ibuprofen to demonstrate the concept; S-ibuprofen is metabolically "cleaner" than racemic ibuprofen.[14] We also performed the separation of S-phebox from RS-phebox (See the Appendix). Phebox is generally used as an efficient auxiliary for asymmetric catalysis and its enantiomeric purity is vital since it provides appropriate stereochemical and electronic circumstances. To our knowledge, this is the first report on analysis of enantiomer purity, and enantio-enrichment based on density using MagLev.

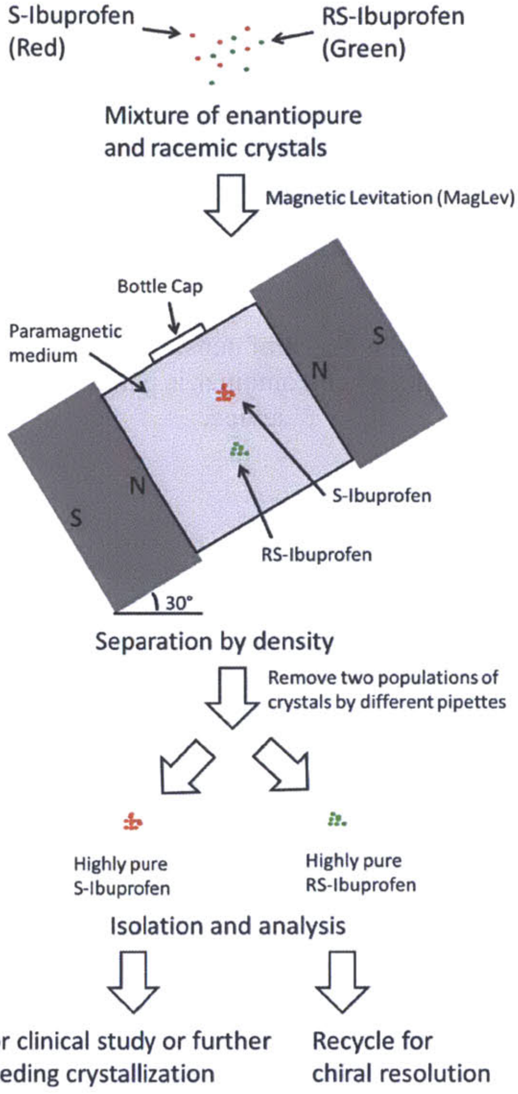

Figure 7-2 Schematic illustration of the separation of enantiopure crystals from racemic crystals of ibuprofen by density using MagLev. . Using ibuprofen as a model ystem, MagLev enables separation and isolation of S-Ibuprofen and RS-Ibuprofen by their difference in density. This method can be used as a general method to analyze enantiomeric purity of a mixture or purify

enantiomer product for further use. The densities of S-ibuprofen and RS-ibuprofen are reported to be 1.093 g/cm$^3$ and 1.110g/cm$^3$, respectively.[15]

## 7.2 Experimental Section

### 7.2.1 MagLev device configuration

The configuration of the MagLev device that we used is shown in Figure 7-2. When an object is placed in the container within the MagLev device, the "levitation height" is defined as the distance from the center of the object to the bottom magnet (aligned along the perpendicular distance between two magnets). With this setup, a low-density object will levitate at a higher height compared to a denser object. We separated the enantiomer and racemic crystals of ibuprofen by levitating in aqueous 0.55M $MnCl_2$ and tilting the MagLev device at 30° for optimum resolution (see the Appendix for details).

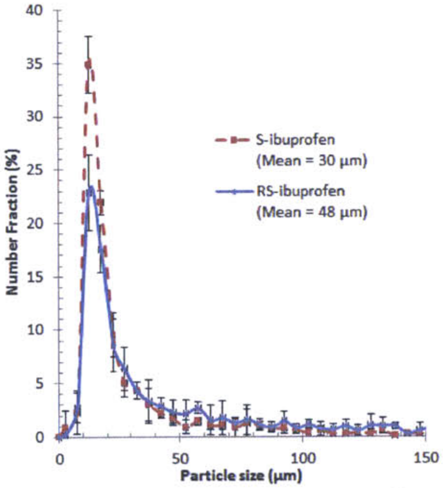

Figure 7-3 Particle size distribution of S-ibuprofen and RS-ibuprofen crystals measured using optical microscopy. The error bars represent standard deviation from seven independent measurements (n=7).

### 7.2.2 Particle size of ibuprofen

Particle size distribution is important when performing MagLev because the separation is slower as the particle size decreases (due to both Brownian motion and fluid shear).[7] Therefore, we performed particle size measurements on ibuprofen crystals using an optical microscope. Figure 7-3 shows that particles of S-ibuprofen (with a mean size of 30 μm) have smaller sizes than those of RS-ibuprofen (with a mean size of 48 μm). The size of these particles is very close to the particle size of the API commonly used in pharmaceutical crystallization processes.

## 7.3 Results and discussion

### 7.3.1 MagLev as an analytical tool

To evaluate the accuracy of MagLev as an analytical tool for measurement of enantiomeric purity, we conducted the separation from prepared ibuprofen mixtures of known compositions. Taking run No. 6 (refer to Table 7-1) as an example, a prepared mixture of 197.62 mg S- and 2.61 mg RS- ibuprofen (98.7%ee) was first dispersed in the glass bottle filled with paramagnetic medium (0.55M aqueous manganese chloride). Then the glass bottle was placed in the MagLev device. The Maglev device was tilted at a 30° in order to increase the separation.[7] After allowing the mixture to separate overnight (~12 hours), two populations of crystals were clearly visible in the sample bottle, as shown in Figure 7-4. The top and the bottom populations levitated to a height of ~ 19 mm and ~ 16 mm, respectively. Their separation distance is ~ 12 mm (distance between two centers of the populations). The crystals in the top population were carefully removed using a 20 mL syringe attached to a needle while crystals in the bottom population were collected directly by vacuum filtration. After drying, the mass of the top and bottom populations were measured. The crystals in the top population weighed 197.51 mg, while the bottom population had 2.33 mg of the crystals. Compared to the total initial mass of 200.23 mg, there was a loss of 0.39 mg during the process (which is probably due to crystals sticking to the glassware or filter paper). During density-separation in MagLev, lower-density objects levitate at higher heights compared to denser objects, thus the top population of crystals should be S-ibuprofen (1.093 g/cm$^3$) and the bottom population of crystals should be RS-ibuprofen (1.110 g/cm$^3$). We performed differential scanning calorimetry (DSC) analysis on the crystals to confirm their compositions. Since S-ibuprofen and RS-ibuprofen have different melting points, the melting peak area was used to quantify composition (see the Appendix for details).

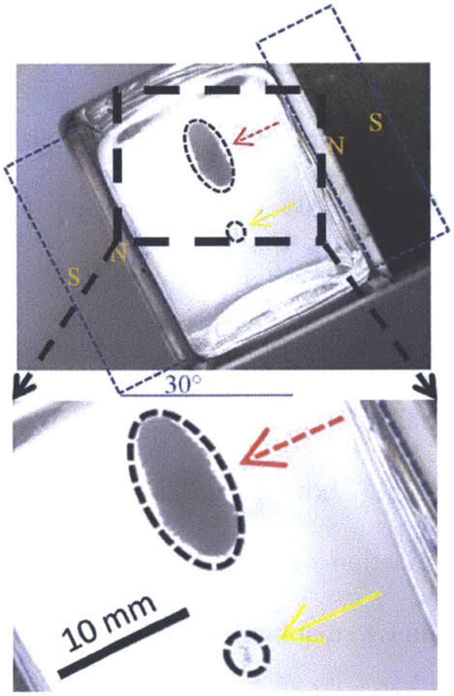

Figure 7-4 Separation of a solid mixture of 98.7% S-ibuprofen and 1.3% RS-ibuprofen in the MagLev device (tilted at 30°): Two populations of solid crystals were obtained, S-ibuprofen in

the upper portion (red dotted arrow) and RS-ibuprofen in the bottom portion (yellow arrow). (An enlarged version of the whole photograph is included in Appendix).

Table 7-1 Enantiomeric purity of S-ibuprofen before and after density-separation from a mixture containing the racemate using MagLev.

| ***Run No.*** | ***Mixture (before separation) (% ee)*** | ***S-ibuprofen (% ee)*** | ***RS-ibuprofen (% ee)*** |
|---|---|---|---|
| 1 | 48.5 | 95.2 | 5.18 |
| 2 | 50.3 | 95.4 | 4.17 |
| 3 | 51.0 | 94.9 | 4.26 |
| 4 | 79.9 | 98.0 | 3.60 |
| 5 | 91.6 | 98.9 | 2.95 |
| 6 | 98.7 | 99.8 | 2.57 |

Both populations of crystals were not 100% pure. In Run 6, the top population (197.51 mg) of crystals showed S-ibuprofen with 99.8%ee purity, indicating that 0.2 %wt of the crystals were RS-ibuprofen (Table 7-1). Crystals found at the bottom population (2.33 mg) exhibited 2.57%ee purity, indicating 2.57%wt of the crystals were S-ibuprofen. Table 7-1summarizes the results of six different separations from different initial mixtures. The contaminations in both populations were present in all six separations (and will be dis-cussed in a later section). From Table 7-1, we see that the reproducibility and selectivity of the separations are good. Run 1-3, starting at similar compositions (~ 50%ee), showed similar separation results: ~ 95%ee in the top population with a standard deviation of ± 0.2%. In addition, Run 6 with an initial purity of 98.7%ee could be separated into two distinguishable populations.

Table 7-2 Comparison of enantiomeric purity analyzed using MagLev to the actual values calculated from the composition of the prepared mixture.

| *Run No.* | *Esimated value by MagLev (% ee)* | *Actual value (% ee)* | *Error(% ee)* |
|---|---|---|---|
| 1 | 48.1 | 48.5 | -0.4 |
| 2 | 50.6 | 50.3 | +0.3 |
| 3 | 51.5 | 51.0 | +0.5 |
| 4 | 80.5 | 79.9 | +0.6 |
| 5 | 92.3 | 91.6 | +0.7 |
| 6 | 98.8 | 98.7 | +0.1 |

We determined enantiomeric purity using integrated melting peak areas from DSC analysis. For convenience, we define racemic crystals in a bulk of enantiopure crystals or enantiopure crystals in a bulk of racemic crystals as "impurity" crystals. The analysis showed enantioenrichment although traces of the "impurity" crystals exist in each population. This is probably due to the fact that the "impurity" crystals in both populations are present in small amounts (< ~5%wt), and thus do not show significant effect on the analysis. Table 7-2 summarizes the results of enantiomeric purity analysis using MagLev. Taking run 6 as an example, the top and bottom populations weighed 197.51 mg and 2.33 mg. Assuming that 197.51 mg are all S-ibuprofen crystals and 2.33 mg are all RS-ibuprofen, the enantiomeric purity of the initial mixture is calculated to be 98.8%ee (estimated value by MagLev). The mixture was prepared with 197.62 mg S-ibuprofen and 2.61 mg RS-ibuprofen (so the actual value is 98.7%ee). Therefore, the estimated value by MagLev showed a +0.1% difference. All the other 5 runs also showed errors < 1.0%. These results suggest that MagLev can be used as a simple and efficient method for analysis of enantiomeric purity and enantioenrichment from a mixture containing the enantiomer and racemate.

### 7.3.2 MagLev as an separation tool

Table 7-3 Enantiomeric purity of S-ibuprofen (top population) after four sequential density-separations using MagLev.

| *Number of Separations* | *1* | *2* | *3* | *4* |
|---|---|---|---|---|
| Purity of top population | 95.1%ee | 97.2%ee | 98.6%ee | 99.2%ee |

Beginning with an initial mixture having enantiomeric purity of ~50%ee, we obtained ~ 5%wt of the racemic compound "impurity" crystals in the top population after separation in Maglev (run 1 in Table 7-1). This result inspired our interest to perform iterative purification steps to increase %ee. We removed the top population of crystals and dispersed them in a fresh paramagnetic solution with the aid of sonication and ran through another density-separation in MagLev (with the same operating procedure, 2nd separation). The purity of the top population increased from 95.1%ee to 97.2%ee after the 2nd separation. Then we carried out the same separation procedure again on the top population (3rd separation). By repeating the separation procedure for a total of four times, we obtained 99.2%ee purity in the top population. We include a figure in the Appendix illustrating the procedure for iterative separations of the top population and Table 7-3 summarizes the enantiomeric purity of the top population after each separation step. As the number of separations increased, the enantiomeric purity of the top population increased. After four sequential separations, an initial mixture of ~ 50%ee was purified to a 99.2%ee product. The yield (defined as the percentage of final product mass over the initial S-ibuprofen mass) was 99.5%. These results indicate that the "impurity" crystals can be gradually removed from a population of crystals by multiple-stage separations using MagLev. The improvement in separation with the use of ultrasonication between successive separations indicates that some type of agglomeration or physical trapping of "impurity" crystals occurs. In addition, it appears that small particles play an important role in the "impurity" particles since (1) good separation was observed during separation of two millimeter sized crystals; (2) crystals smaller than 2 μm are strongly affected by Brownian motion and thus difficult to separate into a cluster by MagLev.

## 7.4 Conclusions

We have demonstrated that MagLev can be used as a simple and efficient method for analyzing enantiomeric purity and chiral separation in pharmaceutical industry. We summarize some highlights here as follows: (1) typically, separating a racemic compound and its corresponding enantiomers requires significant work to develop a HPLC method or understand complex phase diagrams regarding different solvents and temperatures. In using MagLev method, none of the above is a concern. A small density difference (0.01~0.02 g/cm$^3$) that almost exists in every chiral system is good enough for separation. (2) This method can be used for continuous separation as well. Winkleman *et al.* used a microfluidic device combined with magnets to continuously separate and collect polystyrene particles of different densities in a flowing stream of aqueous $GdCl_3$ solution.[16,17] Although the diameters of these polystyrene particles (75 ~ 150 μm) are larger than the crystals used here, our experiments here showed that ~ 80% of particles (volumetric percentage by visual inspection) reached their equilibrium positions within 5 minutes while it takes ~12h for the other ~20% of particles to separate. We therefore believe that it is reasonable to achieve a high degree of separation in a continuous system as long as some considerations are taken into the process design regarding particle size and separation time. (3) It works well with small quantities which can be hard for differential crystallization method. In pharmaceutical drug discovery phase, thousands of new compounds are produced with only a few milligrams for screening. With MagLev, highly pure enantiomer compounds can be easily obtained for further tests. (4) Because the amount of separated racemic and enantiopure crystals are visible, MagLev provides an instrument-free method of detecting small quantities of racemic crystals (or any other impurities of different density) in a bulk of enantiopure crystals. (5) This method provides both highly pure racemic and enantiopure crystals for future use. (6) It gives a high degree of separation in a single step (from ~50%ee to ~95%ee).

In summary, the use of MagLev provides a method that is low-cost, portable, non-destructive, and does not require electricity or extensive skill to operate. The analysis of enantiomeric purity was applied to mixtures of up to 98.7%ee, and the difference between the estimated values from MagLev and the actual values are all < 1.0%. By applying four sequential separations using MagLev, we obtained a highly pure S-ibuprofen product in 99.2%ee starting from a ~ 50%ee mixture with the racemate. In addition, this method developed for chiral analysis and separation is not limited to the pharmaceutical industry, but may also be used as a general tool for analysis and purification in any chiral system that crystallizes into forms that differentiate between chiral and racemic products. The impurities are not limited to racemic compound crystals but can apply to any compounds with different densities than that of the pure enantiomer. We believe developing a continuous separation system using MagLev has potential applications in purifying enantiomers from products of asymmetric synthesis reactions in the production of chiral drugs. It could be an alternative method to solution-based separations (e.g., HPLC or formation of diastereomers), especially in resource-limited settings where these methods are inaccessible or expensive to develop.

## 7.5 Reference

1. N. M. Maier, P. Franco, W. Lindner, *J. Chromatogr.A.*, 2001, **906**, 3.
2. A. M. Thayer, *C&EN.*, 2007, **85**, 11.
3. R. J. D'Amato, M. S. Loughnan, E. Flynn, J. Folkman, *Proc. Natl. Acad. Sci.*, 1994, **91**, 4082.
4. I. K. Reddy, R. Mehvar (2004). Chirality in drug design and development. CRC Press.
5. S. S. Adams, P. Bresloff, & C. G. Mason, *J. Pharm. Pharmacol.*, 1976, **28**, 256.
6. H. Federsel, *J. Nat. Rev. Drug Discovery,* 2005, **4**, 685.
7. G. Gübitz, M. G. Schmid, *Biopharm. Drug Dispos.*, 2001, **22**, 291.
8. V. Dupray (2012), Recrystallization of Enantiomers from Conglomerates, Recrystallization, Prof. Krzysztof Sztwiertnia (Ed.), ISBN: 978-953-51-0122-2, InTech, DOI: 10.5772/33746.
9. H. Lorenz, F. Capla, D. Polenske, M. P. Elsner, A. Seidel-Morgenstern, *J. Univ. of Chem. Technol. and Metall.*, 2007, **42**, 5.
10. K. A. Mirica, S. S. Shevkoplyas, S. T. Phillips, M. Gupta, G. M. Whitesides, *J. Am. Chem.Soc.*, 2009, **131**, 10049.
11. A. Winkleman, R. Perez-Castillejos, K. L. Gudiksen, S. T. Phillips, M. Prentiss, G. M. Whitesides, *Analytical chemistry*, 2007, **79**, 6542.
12. M. R. Lockett, K. A. Mirica, C. R. Mace, R. D. Blackledge, G. M. Whitesides, *J.Forensic Sci.*, 2013, **58**, 40.
13. M. B. J. Atkinson et al. *Angew. Chem.Int. Ed.*. 2013, **52**, 10208.
14. A. M. Evans, *Clin. Rheumatology*, 2001, **20**, S9.
15. I. B. Rietveld, M. Barrio, B. Do and J. L. Tamarit, R. Céolin, *J.Phys. Chem. B*, 2012, **116**, 5568.
16. A. Winkleman, R. Perez-Castillejos, K. L. Gudiksen, S. T. Phillips, M. Prentiss and G. M. Whitesides, *Anal. Chem.*, 2007, **79**, 6542.
17. K. A. Mirica, S. T. Phillips, S. S. Shevkoplyas, and G. M. Whitesides, J. Am. Chem. Soc. 2008, **130**, 17678.

## 7.6 Appendix

The Setup of MagLev Device:

The magnetic field was established in the MagLev device by aligning like poles of two NdFeB magnets (grade N50, 5 cm x 5 cm x 2.5 cm, Model #NB063-N50; Applied Magnets, Plano, TX) co-axially. Both magnets are positioned at 3.5 cm apart, equivalent to the width of the container in which the samples are suspended in the paramagnetic solution (Figure 1). With this setup, a low-density object will have a higher levitation height compared to a high-density object. Previous work showed that tilting the MagLev device at a larger angle generates a larger separation distance between beads of different densities. Using this rationale, we conducted tilted experiments at different angles and found MagLev tilted at 30° yielded a better resolution of crystals and an easy experimental set-up.

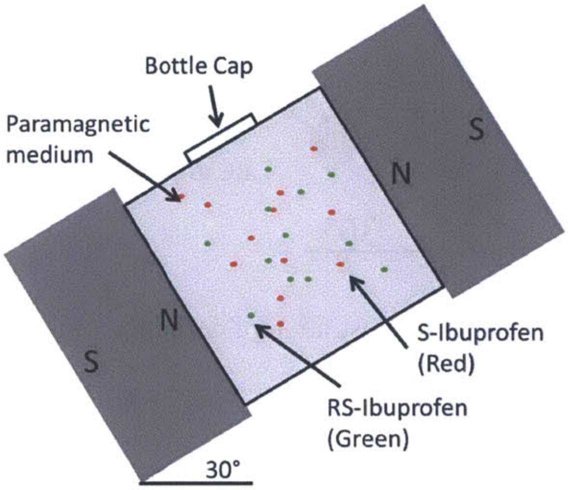

Figure 7-5 Schematic illustration of MagLev device. A cubic glass bottle (filled with the crystals and paramagnetic solution) is placed between two magnets with like poles facing each other. The bottle cap can be opened and the two populations of crystals can be withdrawn by pipettes.

Levitation Heights:

When an object is placed in the MagLev device, the "levitation height" is defined as the distance from the center of the object to the center of the bottom magnet (aligned along the perpendicular distance between two magnets).

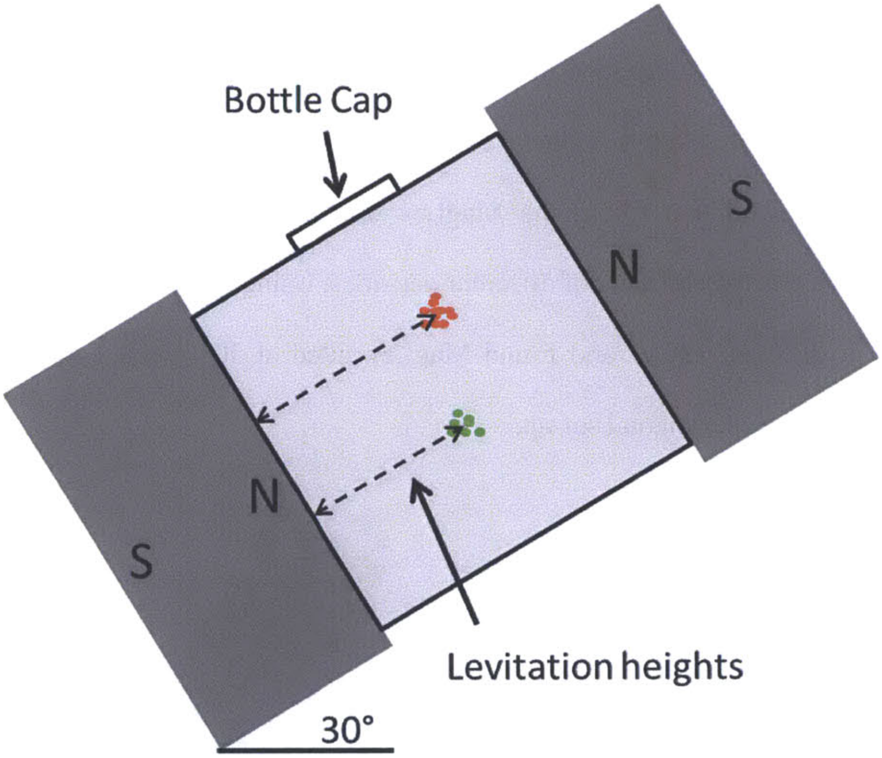

Figure 7-6 Schematic illustration of definition of levitation heights.

Materials:

S-Ibuprofen (>98%, Catalog number I4883) and RS-Ibuprofen (>99%, Catalog number 375160) were purchased from Sigma-Aldrich and used as received. Densities of S-ibuprofen and RS-ibuprofen were reported to be 1.093 g/cm$^3$ and 1.110 g/cm$^3$, respectively, in the literature. These samples were characterized by X-ray powder diffraction (XRPD) and differential scanning calorimeter (DSC), and the results showed that both forms of ibuprofen are pure crystalline materials while no impurity peaks were detected. S-Phebox (Catalog number RNI00022) and RS-Phebox (Catalog number RNI00024) were obtained from Sigma-Aldrich and used as received. Phebox is normally used as an efficient auxiliary for asymmetric catalysis. Manganese(II) chloride tetrahydrate (>99%, Catalog number M3634), sucrose (>99.5% Catalog number S9378) and Tween 20 (Catalog number P1379) were also obtained from Sigma Aldrich.

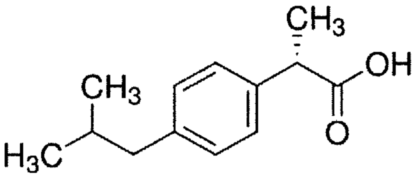

S-ibuprofen

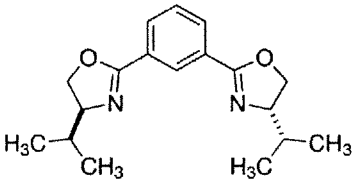

S-Phebox

Experimental Setup:

We placed a mixture of S- and RS- ibuprofen in a 35 mm*35 mm*62 mm glass bottle containing the paramagnetic solutions (0.55M $MnCl_2$, 0.36M Sucrose and 0.5% v/v Tween 20). The mixture was initially dispersed with gentle shaking followed by a 3-min of sonication. From the experiment, we noted that good dispersion is crucial for MagLev separation; however, magnetic stir bar, normally used for strong mixing, may break the crystals into smaller pieces. We applied a 3-minute water bath sonication treatment. Some bubbles emerged due to the presence of the surfactant, and therefore we degassed the solution to remove all bubbles. After the dispersion, the sample bottle was placed at the center between the magnets of the MagLev device and left overnight (~ 12 hours) for crystals to separate (it takes less than 5 minutes for ~ 80% (volume percentage by visual inspection) crystals to achieve equilibrium position, but it takes overnight for the remaining small crystals to equilibrate).

The selection of the paramagnetic solution for separations of enantiopure from racemic crystals is important, if the products are to be used as drugs. First, all components in the solution should be approved by the FDA as excipients non-toxic to humans. Second, the resulting product should meet the United States Pharmacopeia standard after the separations. Considering these restrictions, we used an aqueous solution of 0.55 M $MnCl_2$ as paramagnetic medium (containing Tween 20 surfactant, 0.5% v/v and 0.36 M sucrose to increase its density). We chose $MnCl_2$ salt because it is relatively cheap (< 0.2 cent/g in industry), and produces a transparent aqueous salt solution, allowing direct visual observation of levitating crystals at their levitation heights. Although it is possible that trace amount of the paramagnetic salt may stick to the crystal surfaces (after separation in MagLev), one or several washing steps with water after the separation should be sufficient for the residual salt to a safe level (based on our experience with handling impurity during crystallization). We used water with Tween 20 (0.5% (v/v) as the solvent system because ibuprofen is fairly insoluble in water; however, to prevent sample loss during MagLev separation, we pre-saturated the paramagnetic solution with the same solid compositions as the ibuprofen testing mixture.

### Quantifying Enantiomeric Composition by DSC:

DSC analysis was carried out on a TA Q2000 Differential Scanning Calorimeter. Samples were placed in Tzero® pans and sealed airtight by pressing the lids on the pans. A heating rate of 5°C/min was used.

A typical DSC curve is shown below. The calculation of the sample compositions follows:

$$\frac{S_A}{S_B} = \eta \frac{x_A}{x_B}$$

Where $S_A / S_B$ is the melting peak area for species A/B (enthalpy change during melting, H(S-ibuprofen)/H(RS-ibuprofen) in our case), $x_A / x_B$ is the weight percentage of species A/B, and $\eta$ is a constant. The DSC calibration curve of S/RS-ibuprofen presented a linear relationship y = 0.77x ($R^2 = 0.99$). This relationship works perfectly to calculate the composition for the bottom population of mainly RS-ibuprofen. For the top population of mainly S-ibuprofen, we subtracted the results of the lower population (mainly RS-ibuprofen) from the initial masses of S-ibuprofen and RS-ibuprofen (Mass Balance) and calculated the percentage.

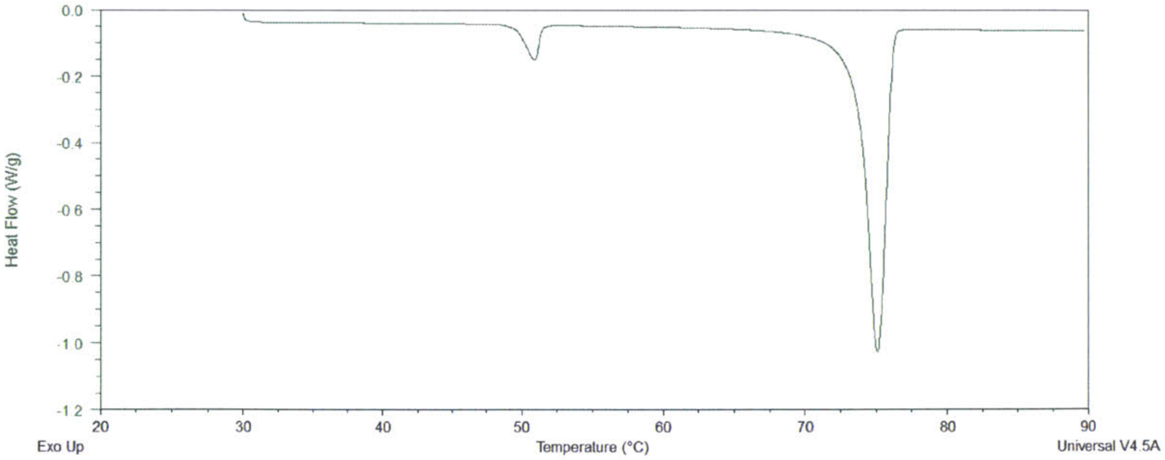

Figure 7-7 A typical DSC curve of a mixture of S- (1st peak) and RS-ibuprofen (2nd peak).

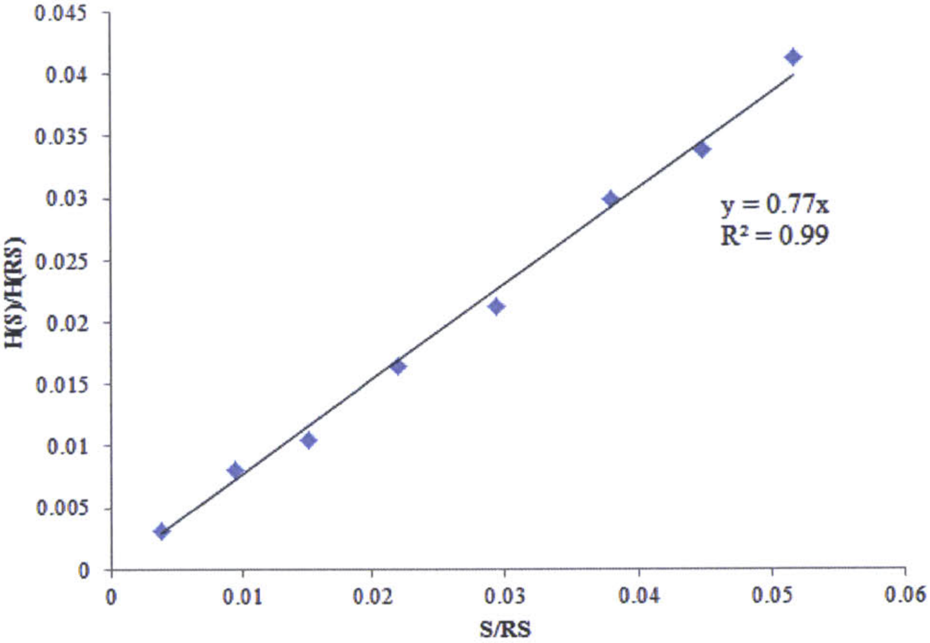

Figure 7-8 Calibration curve of melting peak area for species A/B (enthalpy change during melting, H(S-ibuprofen)/H(RS-ibuprofen) in our case) vs. the weight percentage of species A/B.

Separation of Phebox crystals (A mixture of S-phebox and RS-phebox crystals):

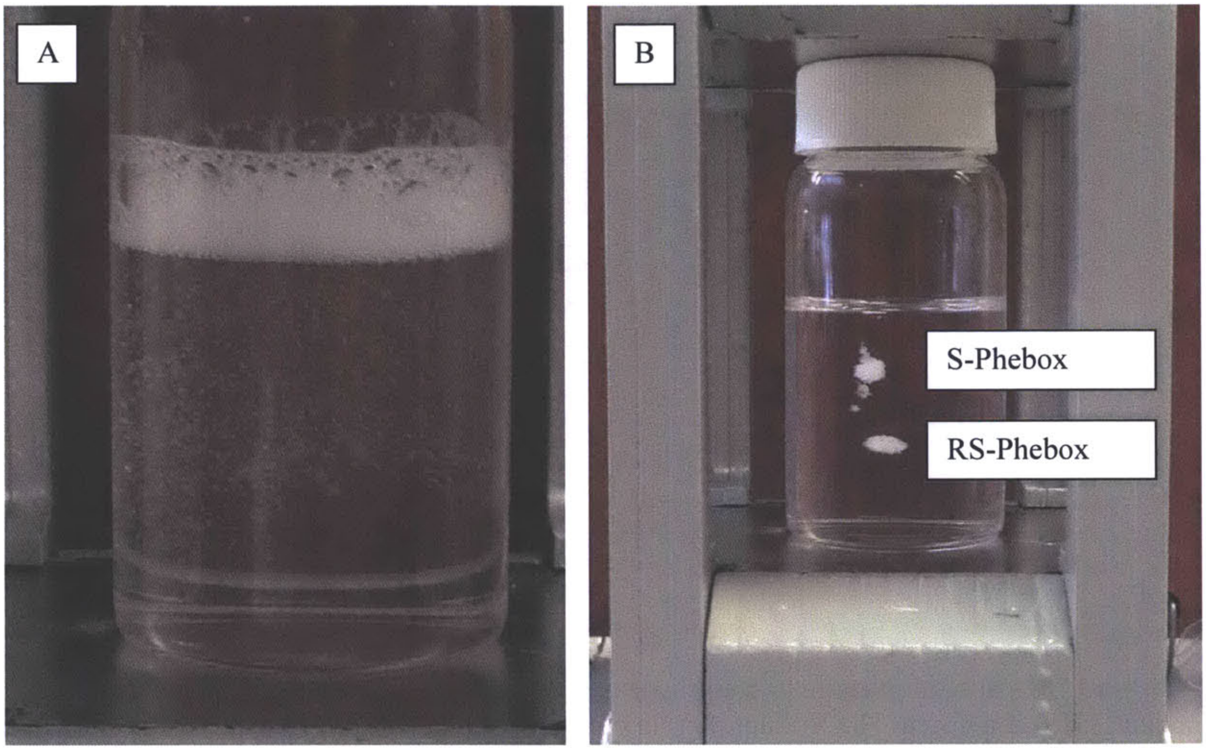

Figure 7-9 Picture showing S- and RS- phebox crystals dispersed in aqueous 1M $MnCl_2$ immediately when the bottle was placed between the magnets (A), and after allowing the crystals to separate overnight in the MagLev device (B). The MagLev device was set up in vertical position (no tilt).

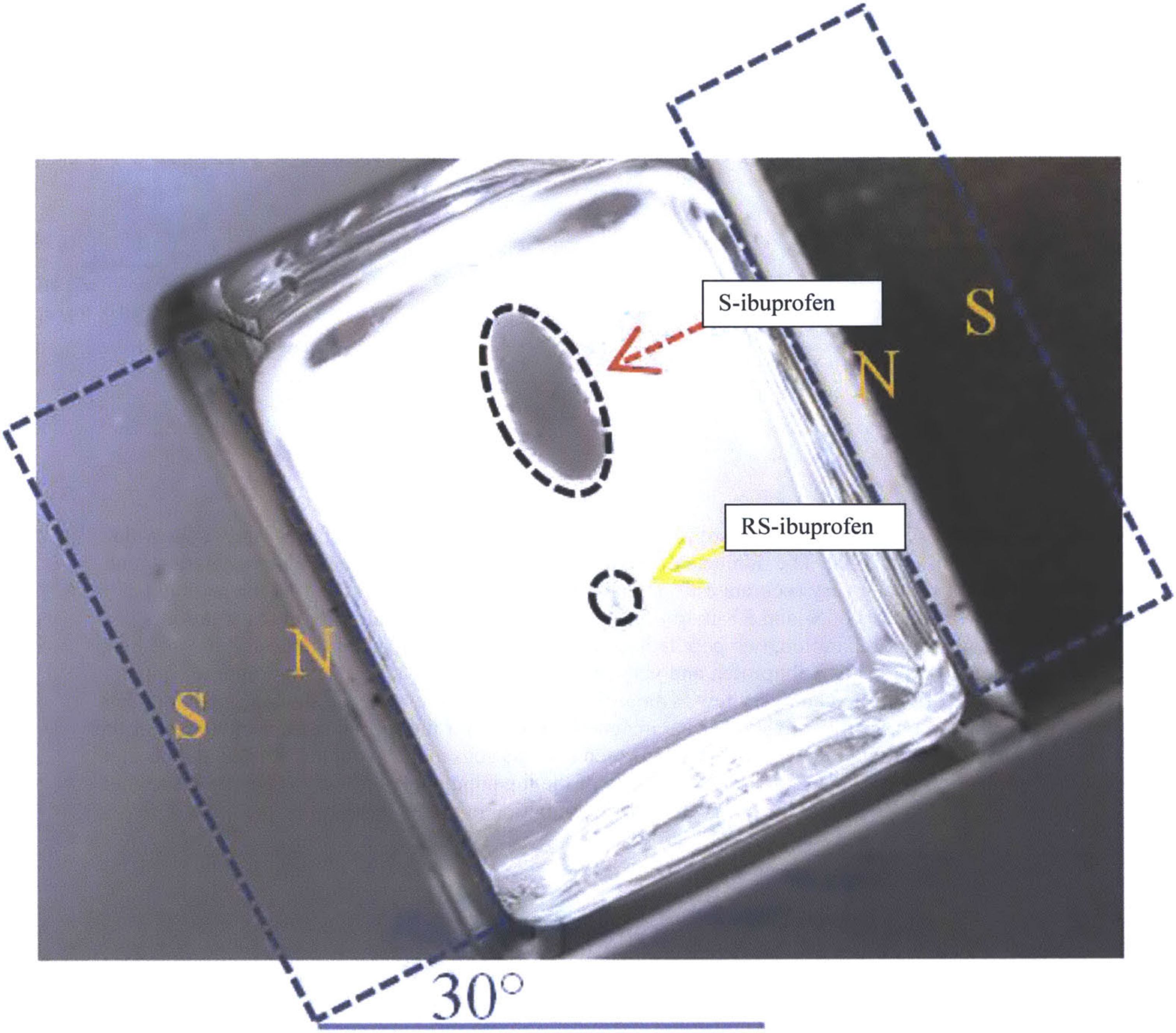

Figure 7-10 An enlarged version of Figure 7-4 in main text.

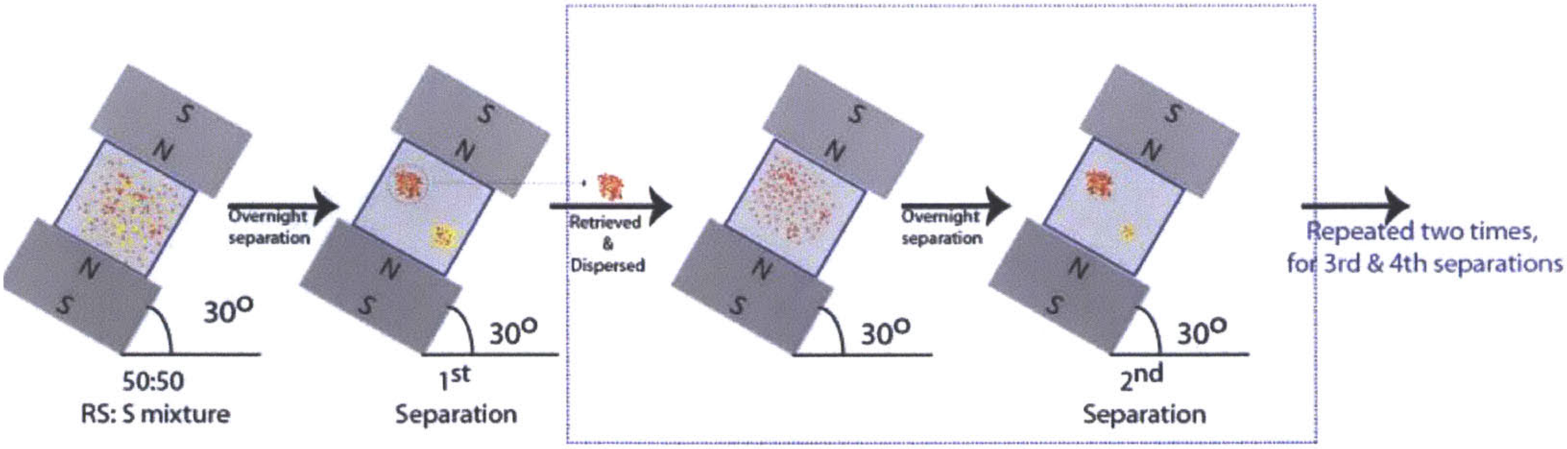

Figure 7-11 Iterative separation of the top population. Red dot: S-ibuprofen crystal; Yellow dot: RS-ibuprofen crystal. The numbers of red and yellow dots only represent relative amounts, and do not reflect a very accurate estimation of the experimental process. (1) At the beginning, known amounts of S- and RS-ibuprofen crystals are dispersed uniformly in the solution. (2) After overnight separation, two populations of crystals are clearly shown in the solution. The top one includes mostly S-ibuprofen and very few RS-ibuprofen crystals. The bottom one contains mostly RS-ibuprofen and very few S-ibuprofen crystals. (3) We retrieved the top population and dispersed it uniformly into another paramagnetic solution for the second separation. (4) After the second separation, the very few RS-ibuprofen crystals got separated out and formed the bottom population of crystals. Therefore, the purity of the top population in the 2nd separation is higher than the purity of the top population in the 1st separation.

# 8 CONCLUSIONS AND FUTURE WORK

## 8.1 Conclusions

This thesis focuses on the systematic study of methods to produce organic molecular nanocrystals and their physicochemical properties in order to improve the fundamental understanding towards nucleation theory and structures of nanocrystals. We have used three different approaches in the study: (1) bi-functional SAMs substrates; (2) crystallization under nano-sized confinement, including soft confinement and rigid confinement; (3) nano spray drying.

In the first approach, we mainly focus on the role of SAMs on inducing heterogeneous nucleation and desire to control the polymorphic outcome based on the chemical interactions. Seven different self-assembled monolayers were employed to study the nucleation behavior of the non-steroidal anti-inflammatory drug mefenamic acid. The results show that SAMs forming a strong interaction with -COOH group of MA molecules preferably produced form II. However, we found that the effect of SAMs on polymorphs was not dominant for MA, and worked only in a certain range of supersaturation. We also explored the effects of temperature, solvent, droplet size and concentration on the polymorph control of MA. Regardless of which factor among these four was changing, it was always related to the supersaturation change in the droplets. We finally demonstrated the ability to make crystals as small as ~ 300 nm and exclusively produce either form of MA by applying our knowledge developed above.

In the second approach, our impregnation method using polymer matrices was proven successful to produce nano-sized organic molecular crystals, for glycine, ibuprofen, acetaminophen and deferasirox, with controlled polymorphs as small as ~100 nm. We also showed that by carefully choosing the right experimental conditions and the polymer matrix, nanocrystals with desired sizes and forms could be obtained. For a rigid confinement, we choose porous silica particles of 40 nm pores for study. Four different compounds were studied, ibuprofen, fenofibrate, griseofulvin and indomethacin. Solid-state Nuclear Magnetic Resonance (ssNMR) was employed to analyze the structure of those compounds inside pores which are difficult to characterize using other analytical methods. We successfully demonstrated the production of 100% or partially nano-crystalline ibuprofen, fenofibrate and griseofulvin in these porous silica particles. The dissolution profiles of these nanocrystals are significantly faster than those of bulk crystals. These results help advance the fundamental understanding of nucleation under confinement and may lead to potential applications in developing new formulations in the pharmaceutical industry.

In the third approach, we used a commercial equipment to conduct spray drying experiments. We examined the nanocrystals produced and found out that these nanocrystals are spherical shapes, indicating disordered structures formed during crystallization. This result is probably due to fast evaporation rates. We also observed the "crystal-bridging" phenomenon only two hours after the spraying, suggesting that these nanocrystals are quite unstable.

The solubility vs size curves of α- and β-glycine were measured. Based on the trends, two curves may cross at crystal radius ~ 97 nm. Several good questions to think about at this point is: whether a dominant facet exists as the major surface in the nanocrystals, whether this face is the same as the dominate facet of bulk crystals, whether the dominant facet changes as different crystallizations are used and how many defects exists on the surface and inside the nanocrystals.

Last, we developed a separation technique using magnetic levitation to separate enantiopure crystals from racemic crystals based on their density difference. Starting from a ~50%ee mixture of S- and RS-ibuprofen crystals, we finally obtained a product of 99.2%ee by four sequential separations. This separation technique could also be used as an analytical tool to detect the %ee of the sample. As organic molecules are easily to possess many solid forms such as polymorphs, solvates, and co-crystals, we believe this technique may have huge potentials in industry.

## 8.2 Future work

In this thesis, we successfully demonstrated using three different approaches to produce organic molecular nanocrystals and illustrated advantages/disadvantages of each method.

To further explore the surface molecules and defects on properties of nanocrystals, I suggest combining the bi-functional SAMs substrates method with an advanced atomic level detection technique, for example, STM. Bi-functional SAMs substrates are still the most promising way to produce nano-sized crystals in a controllable way with relatively low supersaturation, indicating less defects and disorders may form during crystallization. Besides, it allows direct observation to the nanocrystals unlike crystallization under confinement.

To better develop industrial applications of organic molecular nanocrystals, I suggest the second approach either under soft confinement (polymer matrices) or rigid confinement (inorganic porous materials, such as silica or alumina). Both studies showed promising enhanced dissolution profiles. However, several problems should be noticed. (1) XRPD is a good tool to detect surface crystals and crystals within in a few micrometers under the surface, but for crystals deep inside the matrix solid state NMR or other tools should be considered. (2) Eliminating surface crystals may also cause the wash away of some crystals inside the pores, so how to optimize the washing steps to maximize the loading and ensure all particles experiencing the same levels of washing are practical problems when considering industrial applications.